Impact of Variations in Patient and Beam Parameters on Proton Therapy using Pencil Beam Scanning technique

J. Paramasamy
2022

Erasmus MC
Universitair Medisch Centrum Rotterdam

TUDelft

LUMC

HollandPTC
Protonen Therapie Centrum

Johannes Vermeer (1632 - 1675)
Inspirator van Holland PTC
Passie in precisie

Wij laten ons inspireren door Johannes Vermeer die met een
unieke combinatie van zachtheid en precisie in zijn
schilderijen de volmaaktheid benadert.

Het is exact deze zachtheid en precisie die ook wij in ons
werk nastreven, net als het verlichte inzicht waarmee
Vermeer onvergetelijke kunstgeschiedenis schreef.

Impact of Variations in Patient and Beam Parameters on Proton Therapy using Pencil Beam Scanning technique:

HOW ROBUST ARE THE PROTON PLANS FOR INTERPLAY?

Jasika Paramasamy
Student number : 4442288
20 June 2022

Thesis in partial fulfillment of the requirements for the joint degree of Master of Science in
Technical Medicine
Leiden University; Delft University of Technology; Erasmus University Rotterdam

Master thesis project (TM30004; 35 ECTS)
Dept. of Biomechanical Engineering, TU Delft
September 2021 – June 2022

Supervisor(s):	MSc. Kees Spruijt
	MSc. Yibing Wang
	Dr. Michiel Kroesen
	Prof. Dr. Mischa Hoogeman

Thesis committee members:	Dr. Ir. John J. van den Dobbelsteen, TU Delft (chair)
	Prof. Dr. Mischa Hoogeman, Erasmus MC
	Dr. Michiel Kroesen, Erasmus MC
	MSc. Kees Spruijt, HollandPTC

An electronic version of this thesis is available at http://repository.tudelft.nl/.

Acknowledgements

Summary

Pencil beam scanning is a technique used in the proton therapy. This technique makes use of a thin beam which can irradiate each spot at millimetre precision. It is a very promising technique, especially for more radiation sensitive areas, e.g. lung carcinogenesis, as it can spare more healthy surrounding tissue compared to conventional radiation therapy due to proton's physical property of the Bragg peak: this is the explosively release of the particles' energy at a certain point in the beam path; a minimal energy loss is obtained before this peak and no energy is deposited after this Bragg peak. In the PBS, interplay is a concern. The interplay effect is defined as the interference of the moving beam and breathing induced tumour motion. Hence an inhomogeneous dose distribution occurs which differs from the planned dose. In the interplay effect different parameters are involved, which can be divided into beam and patient parameters.

The HollandPTC developed a Quality Assurance tool for assessing the interplay effect in lung treatment plans in which a first order sinusoidal function is utilized. However, a sine function is not reflecting the daily variation in target motion and also beam delivery fluctuates over time. By implementing variations into our QA tool, a more realistic interplay assessment could be obtained. A previously done literature search provided us insufficient information regarding beam and patient parameters describing variations over time, hence we did our own research. In this thesis, an investigation was done to analyse the variation in beam and patient specific parameters.

For the machine parameters, the variation in Energy Layer Switching Time (ELST) and Beam On Time (BOT) was determined for the VARIAN ProBeam 4.0. Three clinical lung plans which contained in total nine beams, were irradiated on an array of ionization chambers multiple times over multiple days. The output files were analysed regarding the ELST and BOT. For each beam 15 measurements were done, a total of 135 measurements were executed over a period of two weeks. We found variations in ELST between energy layers, but also within an energy layer variations were observed. The within day and day-to-day variations were comparable. Regarding the BOT, this variable strongly depends on the planned dose. Looking at each individual beam: variations between energies were found; no variations within an energy layer was found. By dividing the measured dose of all output files within an energy layer by the corresponding BOT, the dose rate for each energy was obtained. The dose rate was low at low energies and gradually increased towards the higher energies.

Patient parameters were also investigated regarding the tumour motion pattern: the variation in amplitude, period and degree of asymmetry was investigated. In three lung patients, the breathing signal was recorded for 1.5 minutes utilizing the Anzai belt. Five measurements were done: two measurements for two patients and one measurement for one patient. The obtained signals were analysed in terms of amplitude, period and degree of asymmetry for each breathing cycle. Each cycle was fitted into the Lujan's model, hence a value for each of the three variables were observed. For each patient the intra- and inter-session variation was obtained; however, those variations were smaller than the interpatient variation, mainly for the amplitude and period. For our group the amplitude variated between 6 and 12mm and the period variated between 2.5 and 4.5 seconds. The degree of asymmetry was most likely to be 1.

In this analysis, we found that the ELST mainly depends on the step size of the degrader and slit movement. Unfortunately, no hard conclusion regarding the variation within an energy layer could be stated, probably the data transfer systems of the beam line are involved in this variation. Developing a prediction tool for assessing the ELST seems appealing, however more data in different energy ranges should be obtained. For the BOT: this time was more or less dependent on the planned dose. Variations measured for this parameter were caused by inaccuracies of our measurement tool itself. The dose rate depends on the energy: at higher energies a higher dose rate is observed than at lower energies.

Regarding the patient parameters, significant differences are found between patients' respiratory signal e.g., the tumour motion strongly depends on tumour characteristics. Hence, we advise to analyse the tumour motion pattern patient specifically.

In this thesis report the first insights towards the fluctuations in the relevant parameters were determined. The retrieved information can be used to optimize the interplay QA tool, to get a more realistic interplay assessment in the plans.

Contents

List of Abbreviations

4DCT	Four-Dimensional Computed Tomography
AP	Anterior-Posterior
BAS	Beam Adjustment Service
BDT	Beam Delivery Time
BIMTIM	Beam Intensity Monitoring Threshold Interlock Module
BOT	Beam On Time
CC	Cranial-Caudal
CT	Computed Tomography
CTV	Clinical Target Volume
csv	comma-separated values
DICOM	Digital Imaging and Communications in Medicine
ELST	Energy Layer Switching Time
ESS	Energy Selection System
GTV	Gross Target Volume
HPTC	Holland Proton Therapy Centre
ITV	Internal Target Volume
LR	Left-Right
NSCLC	Non-Small Cell Lung Cancer
opg	offline plan generation
PBS	Pencil Beam Scanning
PCS	Process Control System
PDF	Probability Density Function
PLC	Programmable Logic Circuits
PPS	Personnel Protection System
PTV	Planned Target Volume
QA	Quality Assurance
RT plans	Radiotherapy plans
SCLC	Small Cell Lung Cancer
SDT	Spot Delivery Time
SNS	Scanning Nozzle System
SSWT	Spot Switching Time

Introduction

Proton therapy is one of the most advanced modalities for treating cancer. Its primary advantage over conventional external radiotherapy, is its ability to deliver a high radiation dose to a specified depth that stops beyond exploiting the Bragg peak effect [34]. The penetration range of the Bragg peak is directly related to the initial energy of the proton: the higher the energy the deeper the penetration of the particle.

Pencil beam scanning (PBS) is an innovative and intuitive technique used in proton therapy [34]. In this technique an ultra-fine proton bundle (spot size between 2.5-10mm [77]), scans and irradiates the tumour spot by spot for each layer until the full volume has been radiated. Since the dose delivery for protons stops directly after the Bragg peak, PBS is used to provide better dose sculpting on the target and further reduce the dose to normal tissues [35].

PBS has shown promising treatment outcomes in the recent past, especially for lung carcinogenesis whereas critical structures are located nearby, the radiation is restricted only to the tumour [34] [35]. PBS can be used at different moments during the treatment trajectory of lung cancer patients: it can be used as primary treatment; before surgery to shrink the tumour; after surgery to eliminate any cancer cells that remain in the treated area or to ease symptoms. Although PBS theoretically seems to be the ideal technique for treating those cancer types, this technique will have its issues when treating moving targets. In the PBS technique dose is deposited spot-by-spot while the target is moving due to breathing. Due to the interference between the scanning beam and the respiratory induced tumour motion, some parts of the lung tumour get irradiated when they cross the beam scanning path, several parts get irradiated multiple times (hot spots); and other parts may receive no dose at all (cold spots). Hence, an inhomogeneous dose distribution occurs which differs from the actual treatment plan. This phenomenon is referred to as the interplay effect.

In the HollandPTC, one has been working on an interplay simulation Quality Assurance tool for assessing the robustness of the treatment plans for interplay. This software simulates motion into a time resolved 2D dose measurement by shifting each frame according to a predefined target motion. The software allows us to assess the interplay robustness of our treatment plans. In this software, no variation in beam deposition (beam parameters) and target volume motion (patient parameters) is taken into account. It would be appealing to include variations of those involved parameters in the tool, so a more realistic interplay assessment can be perceived.

From literature it is known that beam parameters strongly dependent on unique characteristics of the proton machine in the concerned institution [50][54][55]. As our institution is equipped with the VARIAN ProBeam 4.0, we are interested in the VARIAN machines. Unfortunately, no studies regarding those machines are done yet in literature. The Lujan's model [67] is a widely used model for tumour motion to determine patient parameters. Utilizing this model, lots of population evaluation are done, however we are interested in patient specific variations in breathing pattern.

The goal of our thesis is to analyse the variation of our machine and patient specific parameters. For the first parameter, measurements will be done with the in-house VARIAN machine. The latter parameter will be analysed by recording different breathing signals of our lung patients.

For the sake of comprehensibility, relevant background information regarding the concerned subject is provided in the following section. Subsequently, two executed experiments regarding the determination and analysis of the mentioned parameters are described. In the last section, a general discussion is provided in which recommendations and possibilities for clinical applications are considered.

Background

2.1 | Lung cancer

Lung cancer is the leading cause of cancer death worldwide (18.0% of the total cancer deaths ~1.76 million) in 2020 [1]. Globally 2.2 million patients were diagnosed with lung cancer in 2020 [2]. Lung cancer can affect anyone, however the risk of developing this type of cancer is increased by (passive) smoking, exposure to agents like asbestos and hard metals, exposure to radiation and exposure to indoor and outdoor air pollution [3].

There are broadly two main types of primary lung cancer:
- Non-small cell lung cancer (NSCLC): about 80-85% of all lung cancers are NSCLC. The form of cancer knows several subtypes [4]:
  - Adenocarcinoma: Adenocarcinoma usually evolves from the mucosal glands and represents about 40% of all lung cancers. Lung adenocarcinoma usually occurs in the lung periphery. This type of cancer has a strong association with previous smoking, but it is also the most common subtype to be diagnosed in people who have never smoked [5].
  - Squamous cell carcinoma: Squamous cell lung tumours often occur in the central part of the lung or in the main airway. It develops in the flat top cells (squamous cells) that cover the surface of the main airway. About 30% of all lung cancers are classified as squamous cell lung cancer. This type is more strongly associated with smoking than any other type of NSCLC [6].
  - Large cell carcinoma: About 2% of all lung cancers are classified as large cell [4].
- Small cell lung cancer (SCLC): Small cell lung cancer is an aggressive neuroendocrine cancer. SCLC accounts for about 15% of all lung cancers and is found most often in people with a smoking history [7]. It is marked by an extremely high proliferative rate and poor prognosis.

Other types of cancer may include lung carcinoid tumours, adenoid cystic carcinomas, lymphomas, sarcomas, and hamartomas.

2.1.1 | Diagnosis

When a patient visits the doctor with symptoms susceptible for lung cancer, a chest X-ray is usually the first test used for the diagnosis [8]. However, chest X-rays cannot give a definitive diagnosis because small lesions are undetectable with x-ray imaging, and it often cannot distinguish between cancer and other lung lesions. In any patient suspected of having a lung lesion, a diagnostic intravenous contrast-enhanced CT of the chest should be made, performed from the supraclavicular region to the adrenal glands [8][9].

When from this CT, lung cancer is established, a bronchoscopy is offered. A bronchoscopy is a test used to look inside the trachea and bronchi using a bronchoscope [10]. During this procedure, it is possible to take a small sample of cells (biopsy). The sample is sent to a pathologist, where a pathological examination is done: the cell type of the cancer and affected nodes are obtained [10][11]. After lung cancer has been diagnosed and the type of cancer is determined, the extent of the disease is defined.

For the staging an investigation is done for possible metastases by FDG-PET [8]. For this procedure, the patient is infused with a radioactive analogue of glucose (^{18}F-fluorodeoxyglucose), here the deoxyglucose is ^{18}F-labeled [12]. Increased energy demand and metabolic activity is characteristic of most cancers due to their overexpression of the GLUT glucose transporters and increased hexokinase activity.

2.1.2 │ Staging

Adequate staging is paramount in the investigation of patients with lung cancer to select the most appropriate therapy. There are many staging systems. The TNM staging system is the most common way to stage lung cancer, here T describes the extent of the primary tumour, N the lymph node involvement, and M describes the metastatic disease [13]. In *Appendix 2A* an overview of the cancer staging manual and stage grouping of lung cancer is depicted. Generally, surgery is considered in stage IA till IIB; no radical resection can be guaranteed from stage IIIA t/m IIIC since lymph nodes are involved, the standard treatment for these stages is radiotherapy in combination with chemotherapy; stage IV is principally incurable and is treated with systemic therapy [14][15].

2.1.4 │ Cancer treatment options

Surgery

A straightforward method to treat lung cancer is surgery: during this procedure, the tumour is removed. This treatment option is only effective if the entire tumour is extracted out of the body, hence only non-metastatic tumours are treated in this way [16]. There are different surgery approaches (**Figure 1**) [17]:

- Pneumonectomy: Resection of an entire lung.
- Lobectomy: Resection of an entire lobe.
- Segmentectomy or wedge resection: Resection of only a part of a lobe. This approach is preferred above lobectomy to preserve more lung function.
- Sleeve resection: Removal of a lobe of the lungs and part of the bronchi.

A disadvantage of treating lung cancer with surgery is the chance of spreading the cancer cells during the removal, or leaving microscopic disease around the edges of the region of interest [16][18]. Hence, surgery is generally supported by chemotherapy or radiotherapy to destroy microscopic disease.
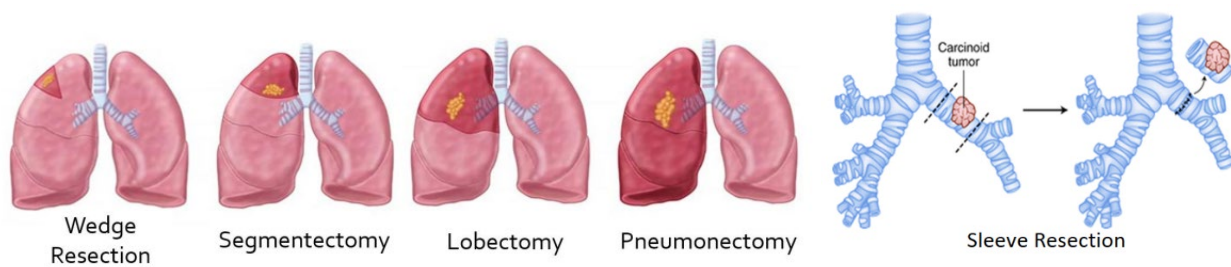
Figure 1: Surgical treatment options for lung cancers (dark red: resected specimen). The standard surgical treatment of early-stage lung cancer is lobectomy, the removal of one of the lobe. Pneumonectomy, the removal of an entire lung, may be necessary if lobectomy cannot completely remove the tumour and the other lung is relatively healthy. In patients with lower pulmonary function, alternatives such as wedge resection and segmentectomy are viable options with higher risk of recurrence. Pulmonary sleeve resection is a type of complex lung resection and reconstruction surgery typically performed for patients with locally advanced lung cancer that involves central airways or vascular structures.

Systemic therapy

Refers to any type of cancer treatment that targets the entire body to damage or destroy cancer cells.

- Chemotherapy: The goal of chemotherapy is to inhibit cell proliferation and tumour multiplication [19]. Since the drug is administered to the entire body, it also affects healthy cells, particularly fast-dividing cell types suffer from chemotherapy. Chemotherapy can be administered in neoadjuvant, adjuvant, combined, and metastatic settings.
    - Neoadjuvant therapy is a treatment given before the primary treatment.
    - Adjuvant therapy is the treatment given in addition to the initial therapy, which can suppress or eliminate the growth of microscopic cancer cells.
    - And chemotherapy can also be combined with other treatment options such as radiation for curative intent.
- Immunotherapy: The goal of immunotherapy is based on improved tumour antigen presentation and recognition; stimulation or amplification of an immune response; or disinhibition of immune cells to allow for an improved antitumor immune response [20].

Radiation therapy

Photons and protons are both ionizing radiation, photons primarily indirectly damage DNA, whereas protons do it in a direct manner (**Figure 2**) [21]. Indirect DNA damage is when radiation contacts water around target cells to cause reactions that produce free radicals. Additional contact with nearby oxygen produces an even more toxic superoxide: reactive oxygen species (ROS). These radicals in turn disrupt biological DNA molecules, hence causing damage to cells [22]. Direct DNA damage occurs when a particle directly interacts with DNA [22]. The goal of radiotherapy is to produce a double strand break. This is when both strands of polynucleotides are broken at the same spot. This should understandably be harder for cancer cells to repair. Enough accumulation of these double strand breaks will lead to cell death. It is easiest to cause a double strand break when a cell is in its M phase of the cell cycle, this is when the chromosome is dividing [21][22][23]. Cancer cells divide more often than normal cells, as their cell cycles repeat more frequently. This makes cancer cells more vulnerable to radiation than normal cells.

- Photon therapy: The most commonly used type of external beam radiotherapy is photon irradiation. A photon beam is produced in a linear accelerator: in this machine, high speed electrons, collide with a metal target and photons are released (Brehmstralung). This photon beam can then be directed towards a patient and their tumour.

- Proton therapy: A proton beam is produced in a cyclotron or synchrotron. A detailed description will follow.
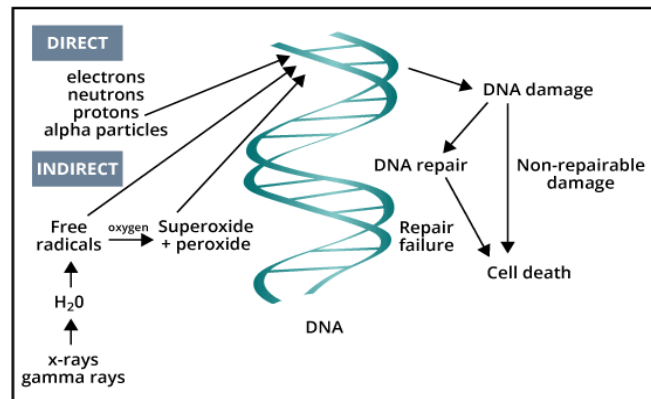
Figure 2: Action mechanism of ionizing radiation. The interaction of secondary electrons with DNA results in direct effects, whereas the interaction of secondary electrons with water molecules leads to generation of Reactive Oxygen Species, which causes indirect effects.

2.2 | Cyclotron

Cyclotron is a device used to accelerate charged particles [26]. It is based on the fact that the electric field accelerates a charged particle, and the magnetic field keeps it revolving in circular orbits of constant frequency due to centripetal force (**Figure 3**). Cyclotrons consist of two hollow D-shaped electrodes [26][27]. The two Dees are placed horizontally with a small gap separating them. Across the Dees a high voltage is applied which sets up an electric field. If a charged particle (proton) is placed between those Dees, the particle is going to experience a force, it will accelerate towards the negative D in the direction of the electric field. During the acceleration the particle will gain kinetic energy because it is gaining in velocity v. The second component of the cyclotron is the application of a magnetic field B. The whole apparatus of the two Dees is placed between the two poles of a strong electromagnet. The magnetic field acts perpendicular to the plane of the Dees [27]. When the proton is in the cavity of the negative D, no differences of potential will be experienced. The force that the proton will experience at that point is due to the magnetic field, but this applies a centripetal force. The centripetal force conducts the particle through a circular orbit.

(a)   (b)
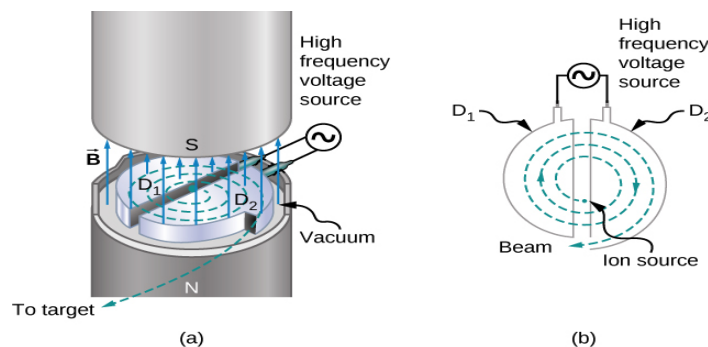
Figure 3: Cyclotron contains of two "D" shaped electrodes, back to back. A strong magnetic field passes normal to the circle. This magnetic field forces the particles to travel in a circular path. A high frequency, alternating current is applied between the two electrodes. The frequency is the same as the number of full rotations made by the particles each second. Charged particles are injected at the centre and are accelerated by the electric field created between the two electrodes. When they come around the circle, the field switches direction, so that the particles are always accelerating.

The particle is going into a circular path, but when it gets to a certain position within the D close to the small gap, the polarity changes: the proton is attracted towards the other D, which is now negatively charged [28]. The particle speeds up, and since the velocity is increased, the particle turns in a larger arc due to the centripetal force when it is in the negative D. As a result the radius of each turn increases, this process will continue till the particle reaches the edge of a D: the proton spirals out of the cyclotron into a beam line with a specific energy [26][27][28].

The working mechanism of all proton machines after the cyclotron are more or less similar: once the proton beam has left the cyclotron, it will encounter the Energy selection system (ESS) [29]. Since all protons have the same energy (~250MeV) after leaving the cyclotron, an ESS is employed to degrade such energy in order to match the particle energy to a shallower depth. The energy selection system consists of an energy degrader, a set of collimators, and a double bend achromatic (DBA) section with an energy selection slit. The energy degrader consists of wedges composed of graphite. It is a motorized mechanical device putting more (or less) of the carbon wedges in the path of the beam to reduce energy. The beam collides with the wedges; hence the energy is selected [29]. The energy scatter due to collimation on the wedges is limited by collimators. After this beam improvement, the beam is focused by quadrupole magnets. These magnets are placed along several places in the beam line to keep the beam focused. Even if the energy is selected using the degrader, we will still have some particles with other energies due to the scatter. To extract undesired energies, the beam will encounter dipole bending magnets which bends the beam according to the energy of the particles. The radius of the curve during bending is given by the centripetal force: higher energy protons are bent in the inside curve and lower energy protons are bent in the outer bend. Due to the bending magnets, the beam will be spread according to its energy. Subsequently, a moving energy slit is used to filter the beam such that only 1% of the beam spread in a certain energy range is permitted through [29][30].

Once the proton beam is directed into the gantry room, the protons will encounter the nozzle [31]. There is an ionization chamber and four steering magnets within the nozzle: two in X-direction (Left-Right) and two in the Y-direction (Cranial-Caudal). The ionization chamber measures the spot weight of the beam and provides feedback to the treatment system to ensure accurate delivery. The steering magnets are required for the scanning. By rotating the gantry, which is a large circular component assembled with the nozzle, the best beam angle for treatment can be selected.
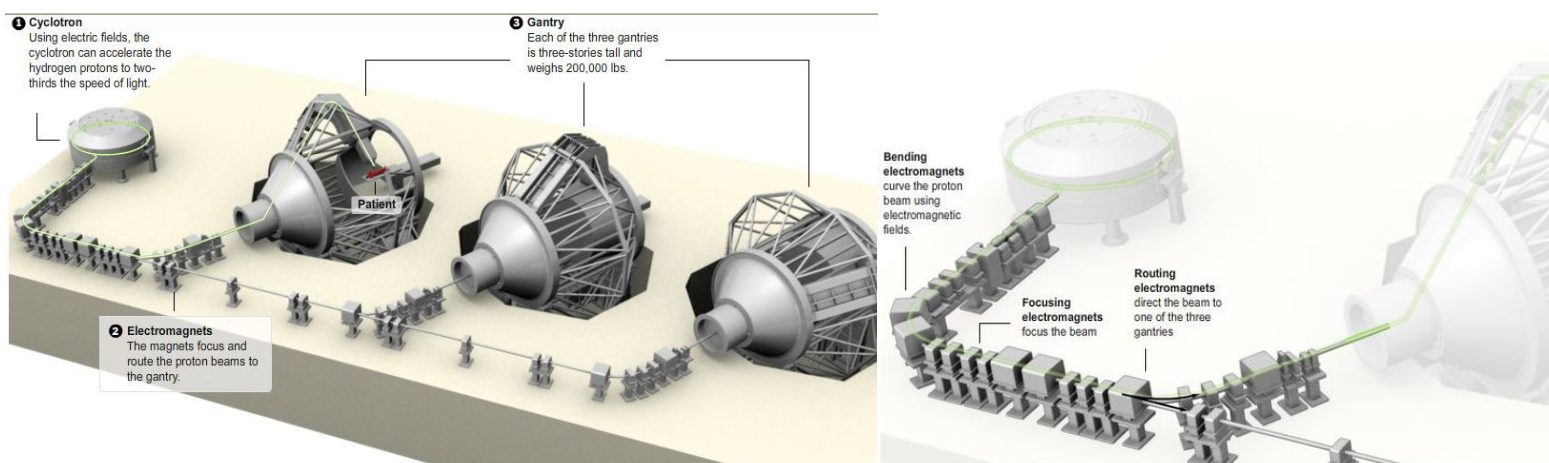
Figure 4: Overview of the cyclotron, beam line and gantry. Using a series of electromagnets to steer the beam, the protons from the cyclotron are sent to each of the treatment rooms using a vacuum line. One cyclotron provides protons for all the treatment rooms. The beam is only in one room at a time.

2.3 │ Bragg peak

A proton is very fast when it enters the patient's body, it deposits only a small dose on its way. The absorbed dose increases very gradually with greater depth and lower speed, suddenly rising to a peak, known as the Bragg peak [32], when the proton is ultimately stopped (**Figure 5**). This is Protons with higher energies have a higher penetration depth compared to low energy protons.

There are several different methods for delivering a proton dose to a patient, the HollandPTC uses both passive scattering and pencil beam scanning technique.

2.3.1 │ Passive scattering

In passive scattering, the proton beam is spread out to be a uniform beam laterally. For this technique a monoenergetic beam passes through a high Z-material, such a divergent beam occurs with a homogeneous dose region (**Figure 5**) [33]. To get a Spread Out Bragg Peak (SOBP), a range modulator wheel is used. The modulation wheel rotates continuously and contains steps of variable thicknesses. Due to this variable thickness, each proton within the beam will have another penetration depth. Each individual Bragg peak stops in another consecutive depth leading to a proton beam which is spread out evenly. Field collimation is required to define field shape.
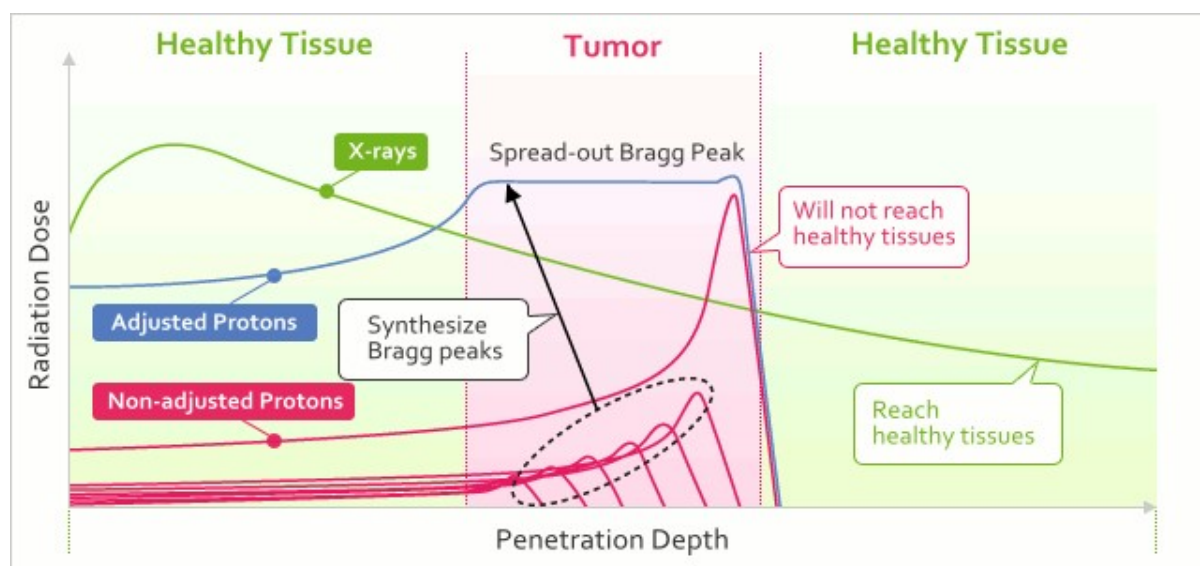
Figure 5: Depth dose distribution for X-ray, protons and Spread-out Bragg Peak. Before photons and protons reach the tumour, both radiation types have to make their way through the patient's skin and surrounding tissues. The photon, with no mass and no charge, is highly penetrating and delivers a dose throughout any volume of tissue irradiated. A proton is a heavy and charged particle that gradually loses its speed as it interacts with human tissue. It deposits only a small dose on its way and delivers its maximum dose at a precise depth (Bragg peak), which is determined by the amount of energy it was given by the cyclotron. Combining beams with different energies it is possible to describe an extended uniform dose region in depth, which is called the Spread-out Bragg Peak.

2.3.2 │ Pencil beam scanning

In the pencil beam scanning technique, an ultra-fine proton beam (spot size 2.5-10mm) is used to irradiate the tumour layer by layer and spot by spot [34]. The target volume is irradiated layer by layer to

adjust for the depth: each layer changes with changing proton energy, the deeper the layer the higher the energy of the proton beam should be. During the treatment in the HollandPTC, we will usually start with the high energy layers and end with the superficial low energy layers [35]. For each layer a particular number of spots is planned, the beam irradiates a spot till its planned dose is reached, then the beam is stopped and the nozzle is steered towards the next spot. After all the spots within an energy layer are irradiated, the next layer will be irradiated spot by spot. This process continues till the entire tumour is covered.

2.4 ｜ Treatment Plan Preparation

2.4.1 ｜ Simulation based on 4DCT Imaging

To make the planning of lung patients for fractionated proton therapy, a planning 4DCT is made [36]. Prior to the 4DCT, a topogram is made: a topogram is an overview image on which the operator determines the scanning range, thereafter the 4DCT is acquired within this range. A 4DCT is a 3DCT in which the time and hence respiration is taken into account [37]. To incorporate the respiration in the measurement the Anzai belt (Anzai AZ-733 V respiratory gating system) is used [38]. This system consists of a load cell pressure sensor integrated in an elastic belt, which is fastened around the patient's thorax. The load cell detects external respiratory real time motion by changes of the pressure and converts this pressure into an electrical signal [38][39]. When the patient breathes in, the pressure on the load cell is gradually increasing resulting in an increasing signal; when the patient breathes out, the pressure on the cell is gradually decreasing resulting in a decreasing signal. The obtained respiratory signal is recorded in synchronization with the CT data acquisition [37]. Hence, a 3DCT volume containing a moving structure is imaged over a period of time, creating a dynamic volume data set.

There are two 4DCT scan modes: cine and helical [40]. For cine 4DCT, data over one respiratory cycle is acquired and then the CT couch is moved to the adjacent position to obtain the next CT data within the next respiratory cycle [41]. In the HPTC, helical 4DCTs are made, and is described in detail here below.

Before the helical scan is started, the estimated respiration rate is determined by looking at the respiration signal of the Anzai belt [42]. The estimated respiration rate plays an important role in setting the combination of pitch and rotation time. The pitch is defined as the ratio between the distance of the imaging table translates in one gantry rotation and the width of the x-ray collimation in one detector (**Figure 6**) [43]. If pitch and rotation time parameters are set correctly, every voxel passes over the detector for at least one breathing cycle. Scanning too fast can result in missed phase information. The longer the breathing cycle, the smaller the pitch factor and the longer the acquisition time becomes.
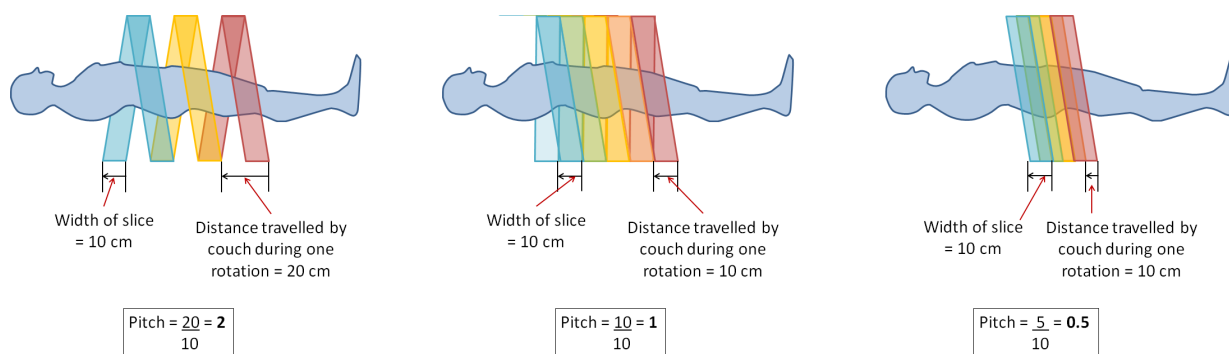
Figure 6: Pitch in helical scan. During a helical scan the couch moves continuously forward during imaging. Pitch is the ratio of table motion per revolution to beam width. Pitches greater than 1 indicate a gap in the helix of the scan. Effects of increasing pitch: decreased scan time; decreased patient dose; decreased image resolution and increased image noise.

The data sufficiency condition or DSC is a term in which each acquisition has to collect data at each location within the ROI for the duration of a breathing cycle plus the duration of data acquisition for an image reconstruction, equal to one gantry rotation cycle [44]. When the DSC is satisfied, scans provide complete coverage without any gap between slices in the imaged volume.

In **Figure 7** below [45], the scanning trajectories of both helical and cine 4DCT are depicted. The two outermost detector rows are shown with thick black lines. Each gray trajectory line corresponds to the detector centres of all detectors which are located between the outer detectors. The x-axis shows the scanning range and the y-axis the time. To scan a full breathing cycle of 4 seconds within a particular range ($z1$ till $z2$), it will take 8.3s for the helical and just 4s for a cine 4DCT to cover 2cm. It takes longer for the helical CT to cover the same region since it needs additional time for the table to translate in the scan to cover all the phases of the respiratory cycle. Taking a closer look at the helical 4DCT, we see that the helical scan starts before $z1$, but also ends after $z2$. The area before $z1$ and the area after $z2$ do not have all the phases of respiration. When looking between $z1$ and $z2$, we see that each phase of each region is covered for at least one period: the images of a certain region taken at x seconds and x+τ seconds, correspond to the images at the same phase but then acquired over two breathing cycles of τ seconds duration. This means that helical images of a particular region and phase may be reconstructed from one or two breathing cycles: e.g. the images in 'seg 2' overlap in the Z region with the images in 'seg 1' since both are obtaining data at the same phase and partly of the same region. The average of both images is taken to produce a single image at a particular location in a certain phase. By continuing this principle over a broader scanning range, all regions will be covered for each phase of the breathing signal (multiple times).
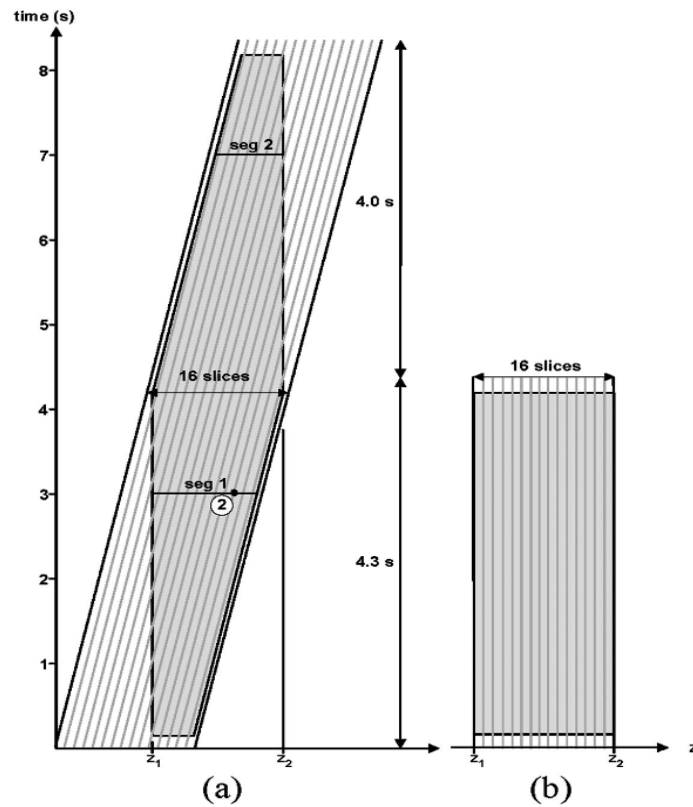
Figure 7: Scanning trajectories of helical (a) and cine (b) 4DCT for the breathing cycle of 4 s are shown. In (a) and (b) the outermost two detector rows are shown with thick lines. Each trajectory line corresponds to the trajectory of the centre of a detector. Z1 till z2 is the scanning range for a particular respiratory cycle. To scan only one breathing cycle of data for 4DCT, the helical acquisition will need to scan for 8.3s, and the cine acquisition needs only 4.3s.

After the 4DCT is acquired, raw image data are sorted according to its temporal relation to the adjacent exhaling and inhaling peak points of the respiratory curve. This is also known as phase-based reconstruction [46]. The breathing cycle is divided into equal time points from 0 to 90% of the period (**Figure 8**). Each bin represents another phase and contains a set of all data points within the region of interest in a particular phase.
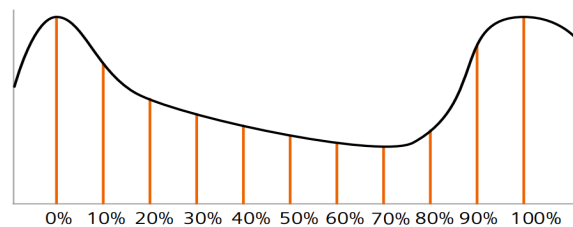
Figure 8: A breathing cycle binned into ten respiratory phases.

2.4.2 | Contouring and treatment Planning

In RayStation the Gross Target Volume (GTV) of the tumour is delineated in the midventilation phase. The midventilation phase represents the tumour in its time-averaged position over the respiratory cycle. In this phase the tumour is located at the average position of full in- and exhale [47]. After contouring of the tumour in this phase, the drawn outline is propagated towards the other phases. The Clinical Target Volume (CTV) in each phase is determined utilizing a formula in which a 0.5cm margin is taken around the drawn GTV [48]. The sum of the CTVs from all phases is referred to as the Internal Target Volume (ITV) [49] and is placed on the average CT. The average CT is the average intensity projection of all phases. Here, the mean attenuation values of each voxel in all phases are taken to create an average CT. After the ITV is placed on the average CT, the dose planning is done on this set of images, where the full ITV region is considered as target volume. On the average CT, the created ITV is expanded with a margin of 2mm, which is then called the ITV+2mm [48][49]. Thereafter, a robustness margin of 5mm is added on the ITV+2mm to account for deviations in tumour position.
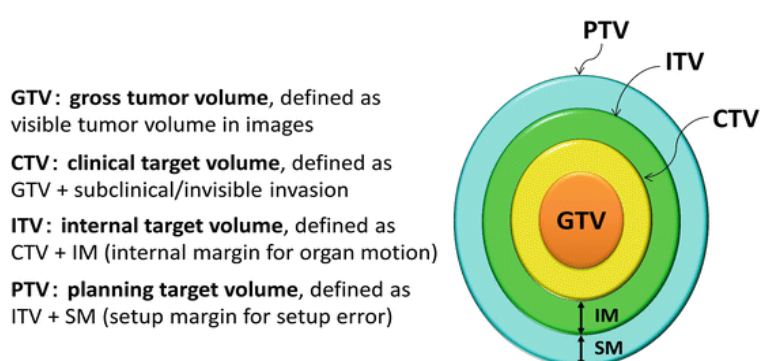
Figure 9: GTV: gross tumour volume, defined as visible tumour volume in images; CTV: clinical target volume, defined as GTV+ subclinical/invisible invasion; ITV: internal target volume, defined as CTV+IM (internal margin for organ motion); PTV: planning target volume, defined as ITV+SM (setup margin for setup error) ≈ ITV+2mm.

In modern proton therapy treatment planning so-called robust optimization approaches are used to ensure that the generated treatments are sufficiently robust against uncertainties [50]. It is difficult to probabilistically define uncertainties in the real procedure. In robust optimization, a limited number of potential error scenarios are included in deriving the plan, such that it fulfils all treatment goals in all the included scenarios. Scenarios are used to present a range of possible alternatives so that the performance robustness of designs can be assessed based on how different designs perform in each of these alternatives [51]. Robustness evaluation is performed using 0.5 cm set-up uncertainty with isocentre shifts in 14 directions on the average CT [52]; 6 with 5 mm in X, Y, and Z directions, respectively; and 8 with 5 in diagonal directions (**Figure 10**). For PBS, 3% range uncertainty is added for the CT density shifts [53]. Adding positive and negative range errors to each setup error results in 28 scenarios; In reality however, there are infinitely many possible error scenarios in which the patient can be. The voxelwise minimum dose is derived as the composite of minimum dose values per voxel from all scenarios for CTV-coverage. Similarly, voxelwise maximum dose is derived as the composite of maximum dose values for CTV-coverage and for organ-at risk dose distributions [51][52][53].
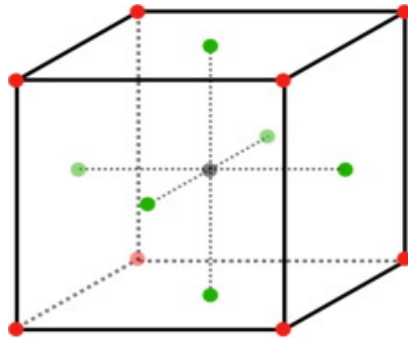
Figure 10: Examples of sampling setup error in a limited number of directions. Common choices include the 6 principal directions (6 green dots), from the centre to the vertices (8 red dots) and combinations of these that result in 14.

2.4.3 | Treatment plan Quality Assurance at HollandPTC

After a treatment plan is created and before the plan is delivered to a patient, patient specific quality assurance is required to verify the treatment delivery by the dose calculation by the treatment planning system [56]. In the HPTC, patient QA is executed by utilizing IBA's MatriXX PT (**Figure 11**): this detector consists of an active area of 24.4 x 24.4cm^2 and includes 1020 ionization chambers with a resolution of 7.6mm [57]. The effective point of measurement of all ionization chambers is located at a depth of 0.6cm from the detector window, which is equal to 0.6cm Water Equivalent Thickness (WET). Using this detector, dose distribution plots are created with predefined sampling time precision. These plots are saved in offline plan generation (opg) format [57].

Figure 11: MatriXX PT. The ionization chamber detector arrays are designed for fast and accurate verification of patient dose.

During patient QA, each planned beam is irradiated at a gantry angle of 0° on the MatriXX. The MatriXX measures the dose in each ionization chamber as set by the frame rate and stores this profile in offline plan generation (opg) format. Each opg file contains an array for the dose of each ionization chamber [58]. A dose distribution map can be obtained by summing up the arrays of each opg file and is referred to as the integral dose [59]. In the software MyQA the measured dose distribution can be compared with the dose distribution expected and planned by the TPS [60].For this comparison a gamma index analysis is done: a gamma analysis compares the delivered dose distribution point by point to that planned by the treatment planning system based on a distance to agreement (DTA) criteria and a dose difference (DD) criteria (**Figure 12**) [61]. The γ is calculated based on finding the minimum Euclidean distance for each reference point in conjunction with the distance between reference to evaluated point and the dose difference between the reference and evaluated point [61][62]. In the HPTC this criteria is set to 2%/2mm. The result of this analysis is a gamma map.
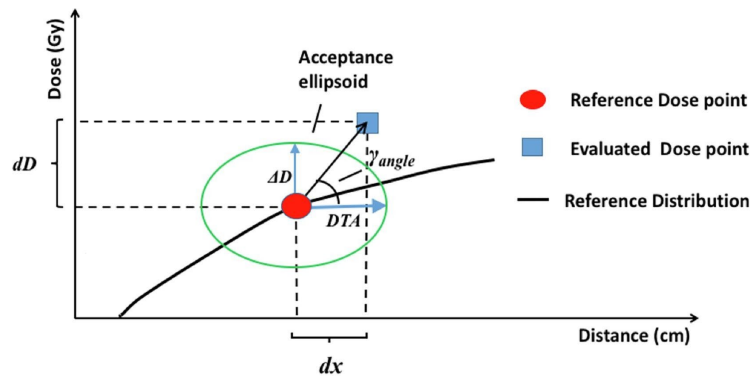
Figure 12: Gamma Index. The gamma evaluation technique is used to compare two dose distributions. It compares dose differences at specific points and determines the distance to the nearest point having the same dose value. The dose difference criterion is important in low dose gradient regions, while the distance-to-agreement criterion yields valuable information in regions having a high dose gradient. Dose difference and distance-to-agreement criteria can be selected and often values of 2%/2mm are used.

2.5 | Interplay effect

During the treatment, the treatment plan is delivered spot by spot to the lungs. Due to respiratory motion, the target volume is moving continuously. In each phase of the respiratory cycle the tumour changes its position while the spots are delivered as planned pretending the tumour is in a fixed position (**Figure 13**). Due to this occurrence locations can be irradiated multiple times in a single layer and others receive no dose at all. This will cause hotspots and coldspots in the irradiated target [54]. Consequently, the inhomogeneous delivered dose distribution, summing the contributions from all the spots, can deviate from the original treatment plan.

In beam pencil beam scanning technique, we also have the beam which is moved for each spot [55]. The movement of the beam can cause an exacerbation of the target motion. The spot by spot delivery executed over time is asynchronous with the breathing motion. The interference between internal tumour motion and scanning pattern is referred as the interplay effect [54][55].
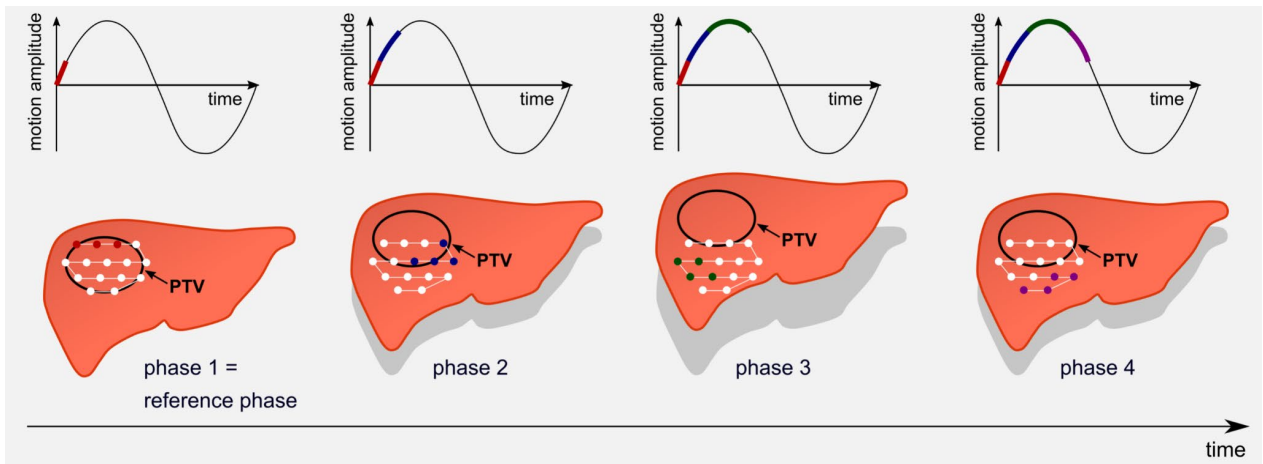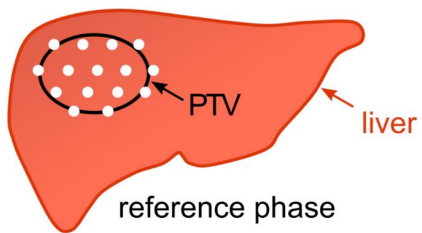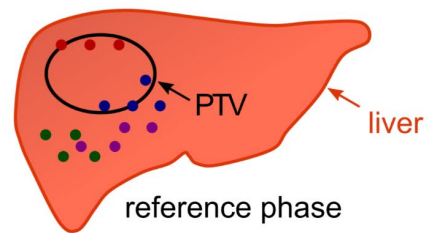
Figure 13: Interplay effect. Planned treatment is shown in white in which a pencil beam is moved spot to spot to irradiate a target. However, while the beam traverses the planned path, the target volume is moving due to breathing motion.

Variation in beam deposition

3.1 | Introduction

One of the parameters that determines the interplay effect, is Beam Delivery Time (BDT). Beam Delivery Time is the time from irradiating the first spot of the first energy layer to irradiating the last spot of the final energy layer. It can be divided into three parts: Energy Layer Switching Time (ELST) (required time to switch from the present energy layer to the consecutive energy layer), Spot Delivery Time (SDT) (required time to deposit a planned spot dose to one spot) and Spot Switching Time (SSWT) (required time to switch from the present spot to the consecutive spot) [63]. The Beam On Time (BOT) is the time needed to scan one energy layer, it is basically all SDTs and SSWTs of one energy layer together.

In the literature, the composition of BDT has been extensively investigated [63][64][65] for proton facilities of IBA. However, similar studies have not been presented for the proton facilities of VARIAN. Because the HollandPTC is equipped with VARIAN machineries, we therefore proposed to investigate the variation in BDT for those apparatus.

3.2 | Method

For this experiment three random clinical lung plans were selected in RayStation. All three plans were based on the PBS technique without repainting. From RayStation, the three radiotherapy plans (RT plans) were exported into Digital Imaging and Communications in Medicine (DICOM) formatted files. Range shifters and other build-ups were removed in all plans utilizing the software program DICOM-Editor. This was done to ensure all possible energy layers were measured, hence preventing energy and/or information loss. Each lung plan consisted of three beams, which means we have nine different beams in total. Each beam was made up of multiple energy layers with multiple spots per energy layer and each layer had its own planned dose. The beams in DICOM format, were subsequently processed into a Python script which extracted relevant beam data: for each beam the energy layers, number of spots per energy layer and planned dose per energy layer were extracted.

Our experiment took place for a period of two weeks from 15/03/2022 to 25/03/2022. Each beam was irradiated three times per day, for five days (each beam was measured 15 times in total = 15 measurement sessions). The measurements were all executed in the same treatment room, namely the Citer.

For this experiment, the MatriXX was placed on top of the treatment couch and aligned by means of the in-room laser positioning system along the main beam's central axis. For the sake of radiation safety, a jerry can filled with water was placed underneath the couch with the MatriXX on top, this can served

as a beam stopper. The setup is shown in **Figure 15**. Prior to each measurement, an uniform reference field of 20 by 20cm of 1Gy was irradiated at an angle of 0° to check the performance of the detector and the beam. The beam trigger settings of the MatriXX for this performance measurement can be found in **Table 1**. The reference field was measured at a depth of 7.6cm. Since the ionization chambers of the MatriXX are positioned at a depth of 0.6cm of the device's surface, a build-up of 7 water equivalent RW3 slabs each with a thickness of 1cm, was required on top of the MatriXX. Lastly, the background radiation was measured by the detector for background correction.

Table 1: Settings MatriXX for reference field and during the measurements. For the measurements the samples before and after beam on/off were set to 50 frames, to ensure the ELST was measured correctly. The sampling rate was set to 0.04s/frame: unfortunately, we are not able to measure with time resolution better than 0.04s/frame, because the computer cannot process all data in time, as a result the data can be lost.

	Reference field	**Measurements**
Sampling time in seconds	0.5	0.04
Samples before beam on	2	50
Samples after beam off	2	50
Number of counts	2	2
Number of pixels	2	2

After the above described performance check, the beam trigger settings were adjusted according to **Table 1** and the beam measurements were started. All beams were irradiated on the MatriXX, which contained no build-up, at an angle of 0°.

During each measurement session, every 0.04 seconds an output file which contains dose distribution information was created. The created files were transmitted to a laptop which contained the software program MyQA. In MyQA, all output files of one session were saved in offline plan generation (opg) formatted files in one folder. In this way, one folder with thousands of opg files in chronological order was collected for each measurement session. This means three folders per beam were created each day; in total 15 folders per beam were created at the end of our research period.

The resulting folders containing the opg files, were subsequently analysed one by one regarding the ELST and BOT utilizing a Python script which was created especially for this analysis. The script basically counts opg files with and without dose per folder. Eventually, for each measurement session two lists, each containing multiple values for ELST or BOT, are retrieved. In *Appendix 3G*, a section of the used script is attached. In **Figure 14** a plot of the working mechanism of the script is visualized.
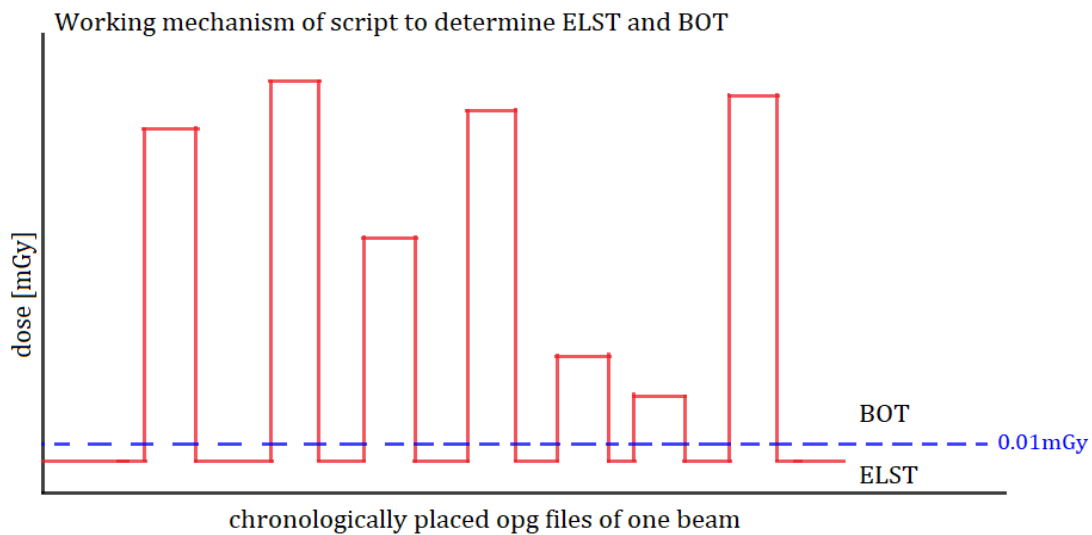
Figure 14: Plot regarding working principal Python script. The folder with chronological retrieved opg files which contains the measurement of one beam, is loaded into the script. The script determines the average dose in each opg in order of time, one by one. The threshold dose was set to 0.01mGy. All sequential opg files with dose less than 0.01mGy will be added up to one energy switching time till an opg file with an average dose of more than 0.01mGy is obtained. If so, then all the opg. files with dose >0.01mGy will be added up to one BOT, till an 'empty' opg. file is obtained. This process is continued till all opg. files in the folder are processed.

After collecting all data, the information of the RT plans and the retrieved measurement data were combined. For each beam, ELST and BOT data of all 15 measurement sessions were joined to the corresponding energy layer. Thereafter, sub-analysis was done for each beam using the combined dataset:

- The step size, which was defined as the required step in MeV to go to the next energy layer, was determined by calculating the difference between consecutive energy layers. The corresponding step sizes were added to the ELST dataset of each beam.
- The corresponding number of spots and planned dose were added to the BOT dataset of a beam.
- The summed dose for all opg files which contribute to the BOT was calculated per measurement session. Hence a list of the measured dose was obtained for each session. The measured dose was compared with the planned dose for each beam.
- Lastly, the dose rate was determined by dividing the measured dose with the corresponding measured BOT for each measurement session of the beam. Per beam, a dataset was created for the dose rate of all measurement sessions together.
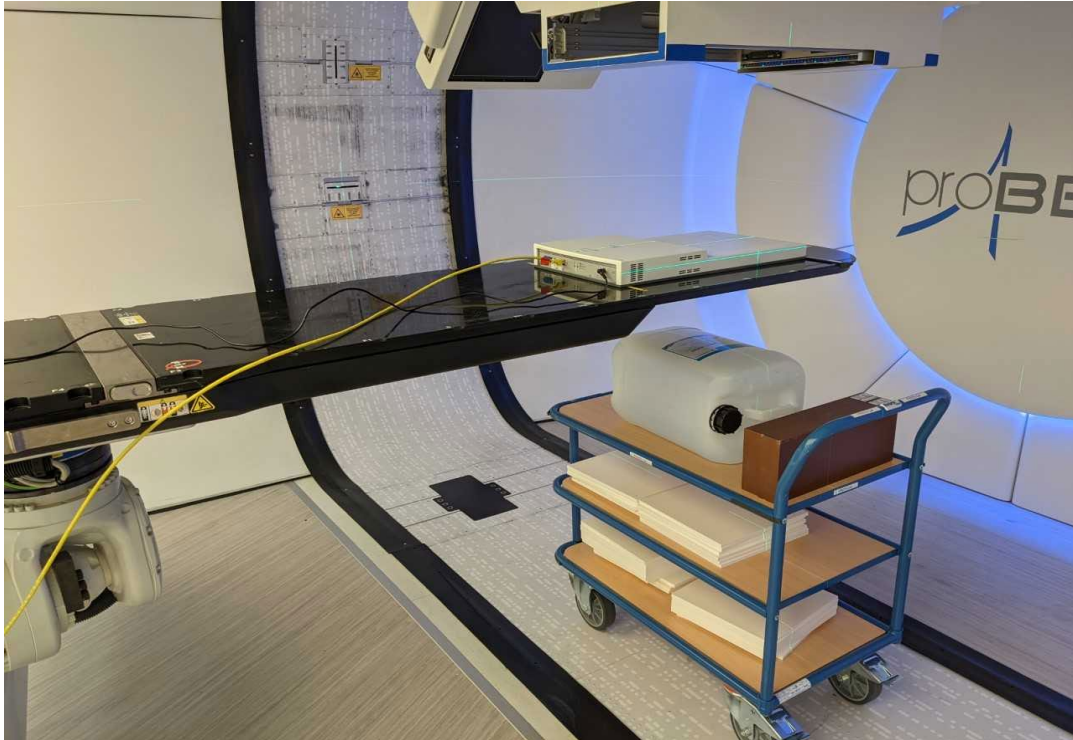
Figure 15: Setup measurement. MatriXX is placed on the treatment couch. Jerry can filled with water (on trolley) is placed underneath the MatriXX.

3.3 | Results

In *Appendix 3A* the extracted data from each lung plan can be found. Due to a problem with the beam stopper on the 15th of March, the measurements only took place for five days instead of six. For each beam 15 measurements were done, a total of 135 measurements were executed over a period of two weeks.

3.3.1 | Energy Layer Switching Time

After processing all the data of the nine beams into the created script, the ELST was obtained. In **Figure 16** below, the ELST is plotted against the energy in a boxplot for all nine beams together. All energy layers on the x-axis, are binned into groups of 2MeV. Each datapoint is added to the consecutive energy: e.g. when the energy changes from 180MeV with a step size of 3MeV to 177MeV, then the datapoint will be added to the 177MeV energy range box. Similar boxplots for each individual beam, can be found in *Appendix 3B*, in those plots the step size per energy layer is also visualized.

As the ELST depends on the step size in MeV of the previous energy layer to the consecutive energy layer, we divided each value of ELST with the corresponding step in the plans which was taken to get to the next energy layer (see **Figure 17** for all nine beams together). In *Appendix 3C*, the individual ELST per step size boxplots for each beam are attached.
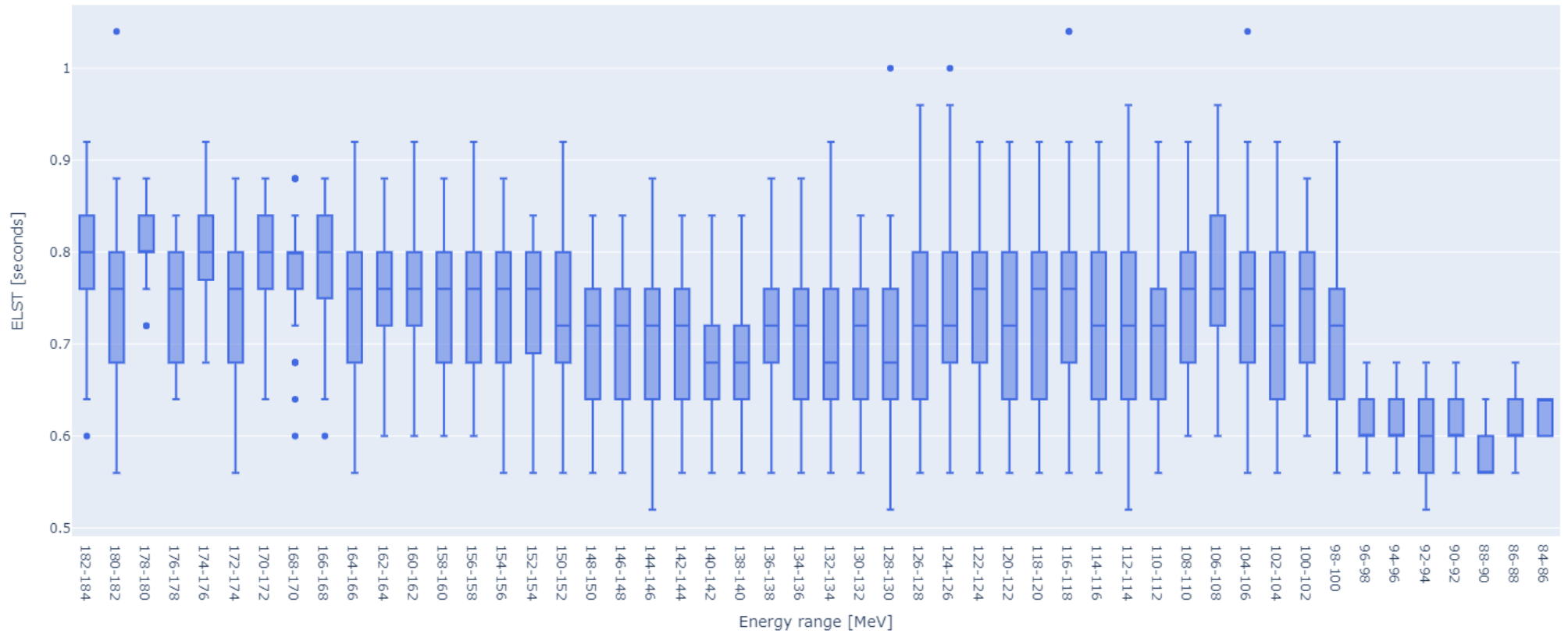
Figure 16: Boxplot of the Energy Layer Switching Time in seconds for all the measured nine beams. Each box represents an energy range of 2MeV with its variations.
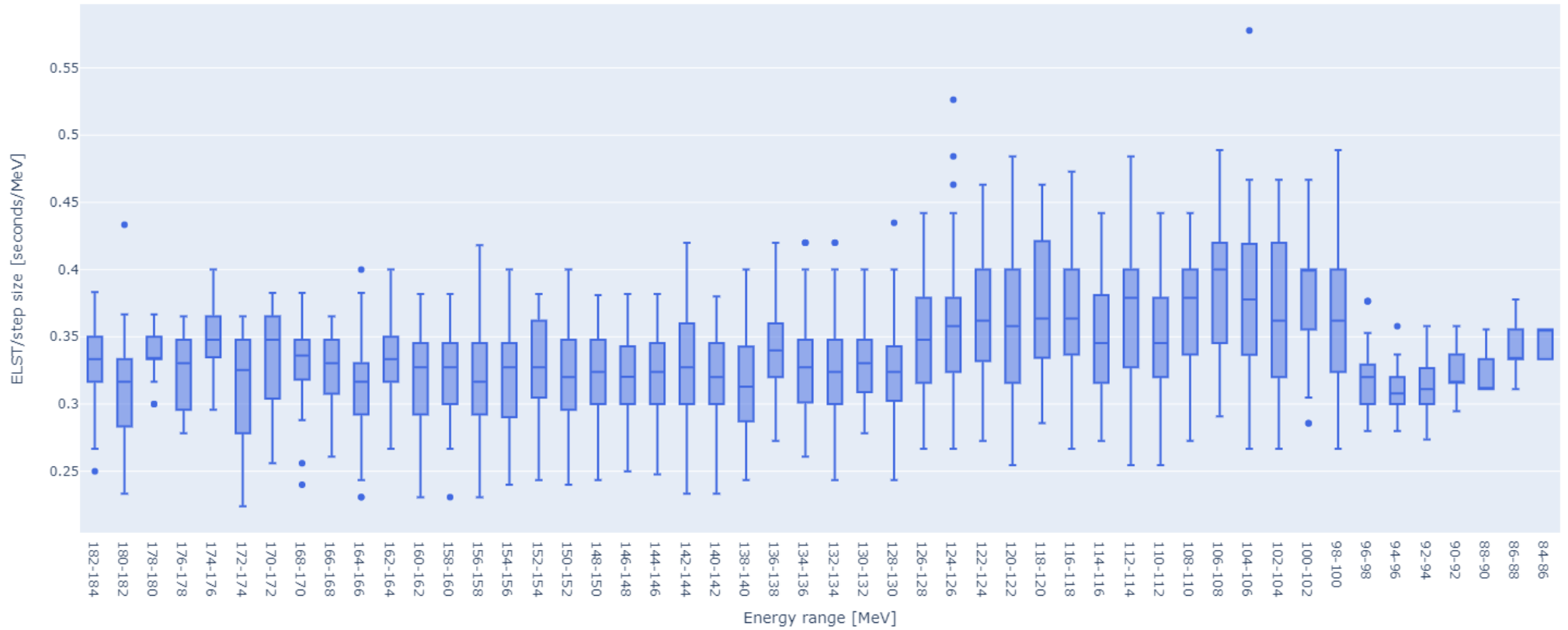
Figure 17: Boxplot of the Energy Layer Switching Time per step size in seconds for all the measured nine beams. Each box represents an energy range of 2MeV divided by the corresponding step size with its variations.

The measurements were executed over multiple days. In **Figure 18** a boxplot is created where the day-to-day variation of the mean ELST is visualized. Each box represents one beam, the coloured data points describe the mean ELST for each day. Each colour corresponds to a specific day.
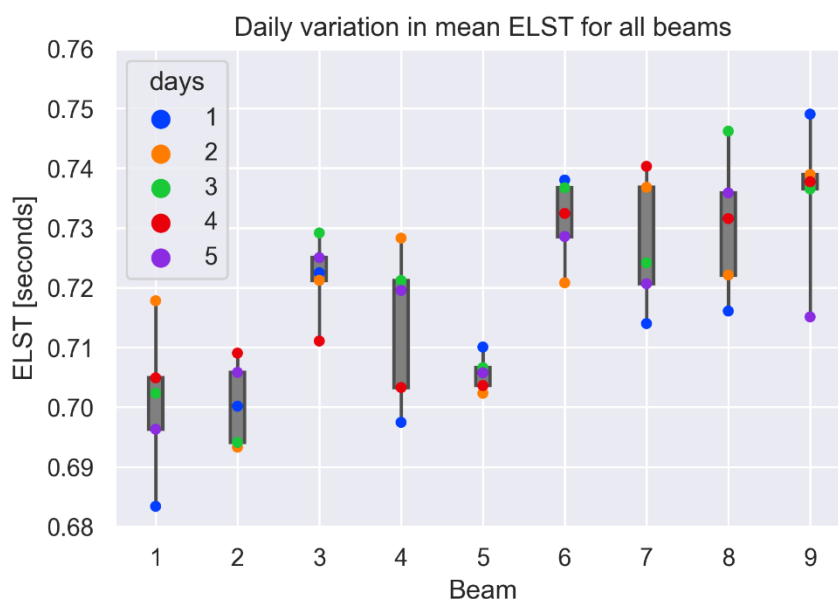
Figure 18: Day-to-day variation in mean Energy Layer Switching Time for each beam. Each colour represents a day: blue 16/03/2022; orange 18/03/2022; green 22/03/2022; red 23/03/2022 and purple 25/03/2022. Relevant dates of the ion source renewal: 04/03/2022 and 19/03/2022.

3.3.2 | Beam On Time

A similar analysis was done for the BOT utilizing the previously mentioned Python script. In *Appendix 3E*, boxplots for the BOT for each beam can be found. In **Figure 19** a boxplot is created where the day-to-day variation of the BOT is visualized for each beam. Since the BOT of all beams vary in different time ranges, each box is zoomed within the corresponding range (**Figure 20**).
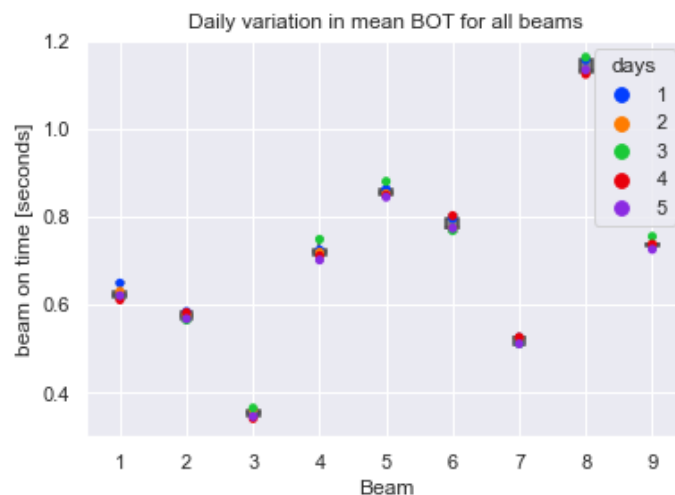
Figure 19: Day-to-day variation in mean Beam On Time for each beam. Each colour represents a day: blue 16/03/2022; orange 18/03/2022; green 22/03/2022; red 23/03/2022 and purple 25/03/2022. Relevant dates of the ion source renewal: 04/03/2022 and 19/03/2022.
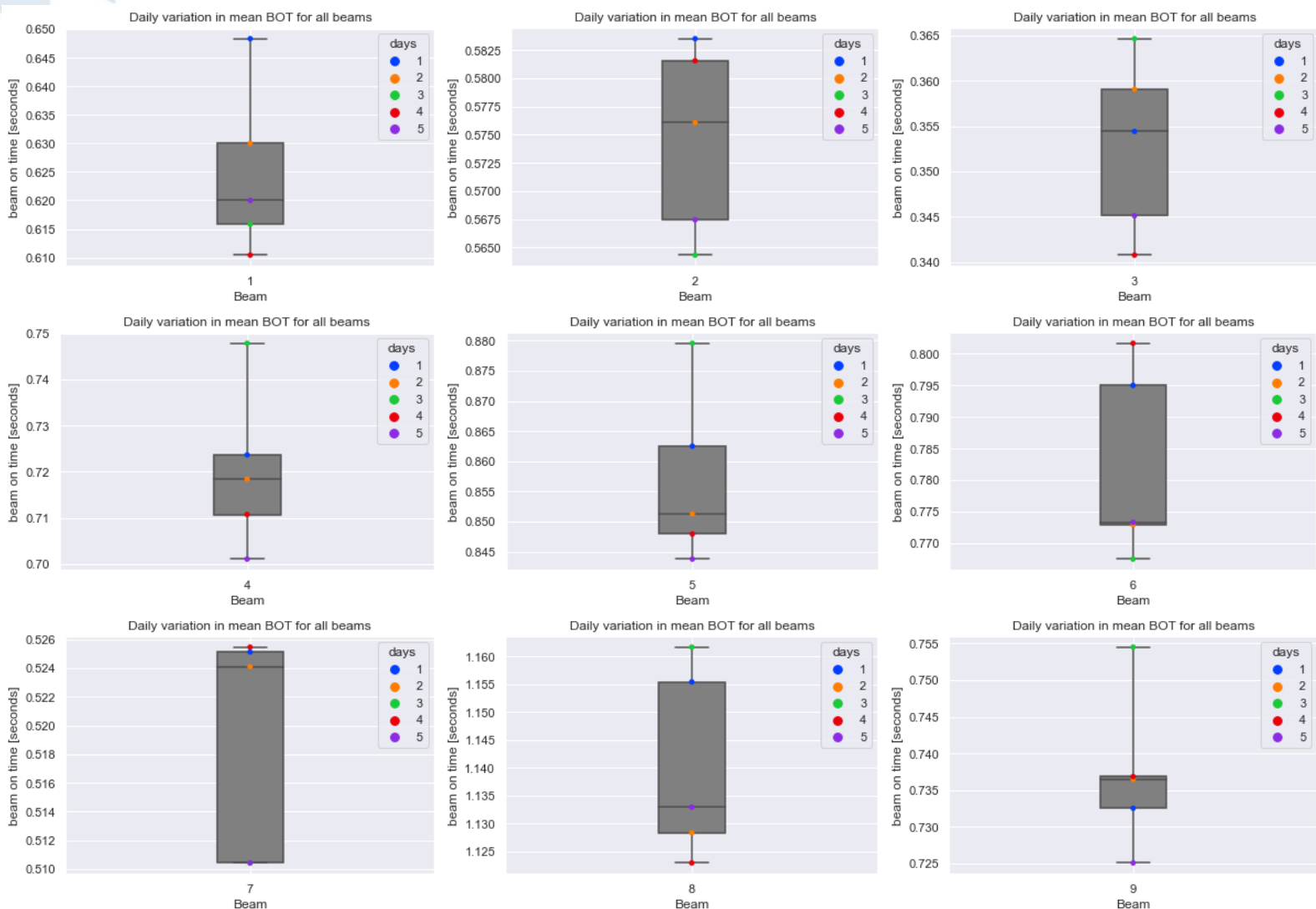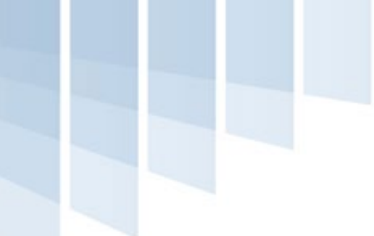
Figure 20: Day-to-day variation in mean Beam On Time for each beam zoomed-in for the concerned time range.

In *Appendix 3D*, the measured dose is plotted against the planned dose for all individual beams. By dividing the sum of the measured dose in mGy by the corresponding BOT, the dose rate is determined. In **Figure 21** a boxplot is plotted for the dose rate against the energy for all the nine beams together. In *Appendix 3F*, boxplots of the dose rate against the energy layer for each individual beam can be found. The planned dose and number of spots per energy layer is also visualized in those plots.
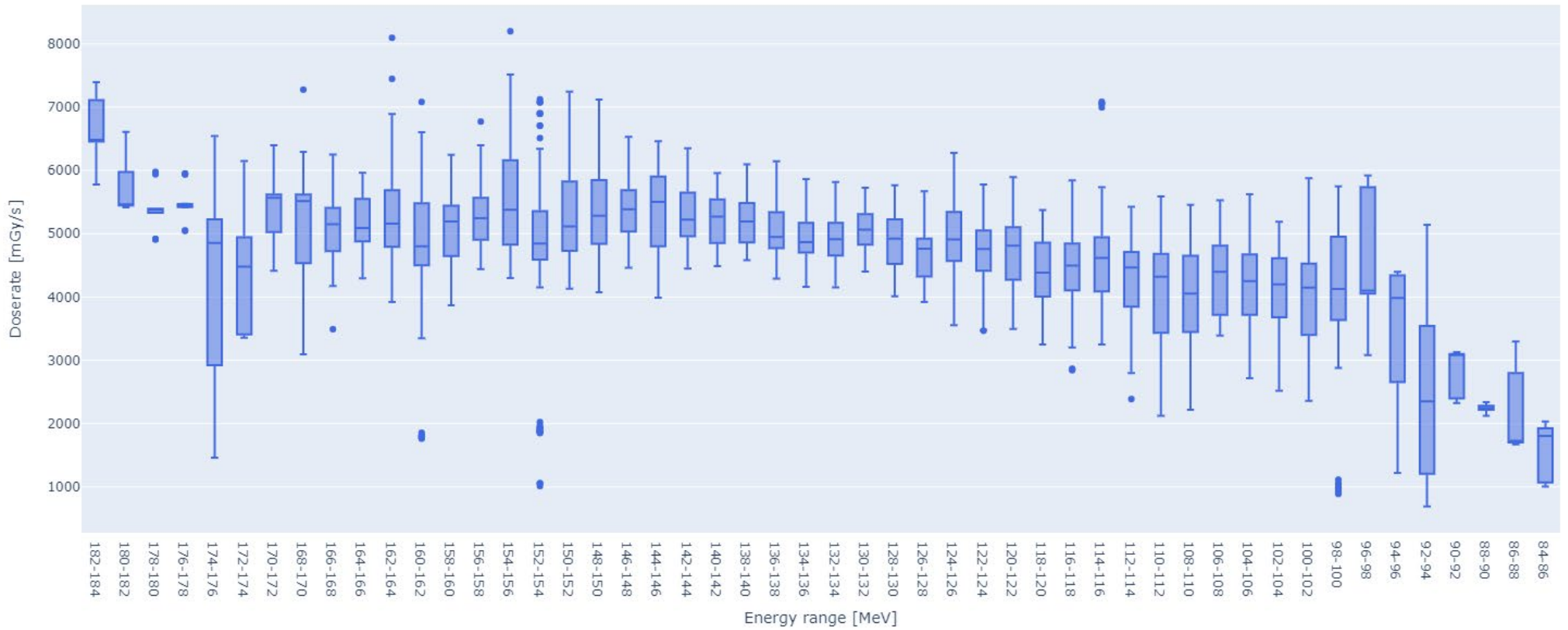
Figure 21: Boxplot of the Dose rate in mGy/seconds for all the measured nine beams. Each box represents an energy range of 2MeV with its variations in dose rate.

3.4 | Discussion

As we are restricted in the data accessibility of VARIAN, we can only measure the dose distribution over time utilizing our MatriXX device which has a restricted sampling time. The individual spot delivery (SDT) and spot switching (SSWT) are too fast processes and therefore not measurable with the MatriXX, hence we divided the BDT in our experiment into ELST and BOT.

3.4.1 | Energy Layer Switching Time

In **Figure 16**, the results of the ELST per energy range are visualized. We see that the ELST is increasing for higher energies. A reason for this occurrence could be the step size in each individual beam plan. When taking the plans in consideration (*Appendix 3B*), we see that the step size is increasing for the higher energies. In **Figure 22**, the proton energy is plotted against the degrader thickness [66]. Here, assuming a linear correlation, we strongly believe that the step size will affect the ELST. To normalize the ELST values for the step size, we divided each value with the corresponding step size of each beam plan, which can be seen in **Figure 17**. Here a quite constant value for the ELST per step size is obtained. As mentioned previously, the degrader is responsible for the energy selection: the wedges of the degrader are driven using a stepper motor and linear stage. The wedge position is proportional to the energy and hence the ELST depends on the step size. According to VARIAN, the carbon wedges move with a constant speed of 1200 mm/minute, and therefore the degrader motion will not depend on the energy but on the energy step which is taken to go to the next energy layer.
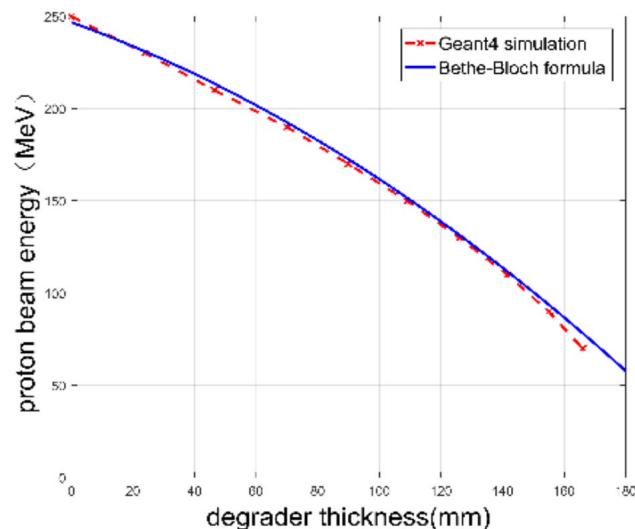
Figure 22: Proton beam energy versus the degrader thickness. The proton beam energy varies with the degrader thickness [66].

However, taking a closer look at **Figure 17**, a slightly elevated ELST per step size is obtained in the range of 98-128MeV compared to the energies outside this range. As described earlier, the energy selection system consists of multiple components including the achromat. The achromat has bending magnets, to spread the proton beam according to its energy, followed by a moving energy slit which only permits a certain energy spread in an energy range to go through the beamline. Since the energy slit is a moving object, we need to investigate its contribution to the ELST. In **Figure 23**, a graph of the calibration settings is provided, here the position of the energy slit is plotted against the energy. In the range of ~70-100MeV and ~140-190MeV the position is quite constant, while in the range of ~100-140MeV and ~190-245MeV a ramp is observed. With other words, whenever the slit is moving, it will contribute to the overall ELST; if the slit is not moving while the energy is changing, then the contribution will be zero. Note that this slit contribution in ELST is probably visible in **Figure 17**, where we found an elevated ELST per step size in the range of 98-

128MeV. No results for energies above 184MeV are obtained (maximum energy in measured plans), hence the ELST in the range of 184-245MeV could not be observed.
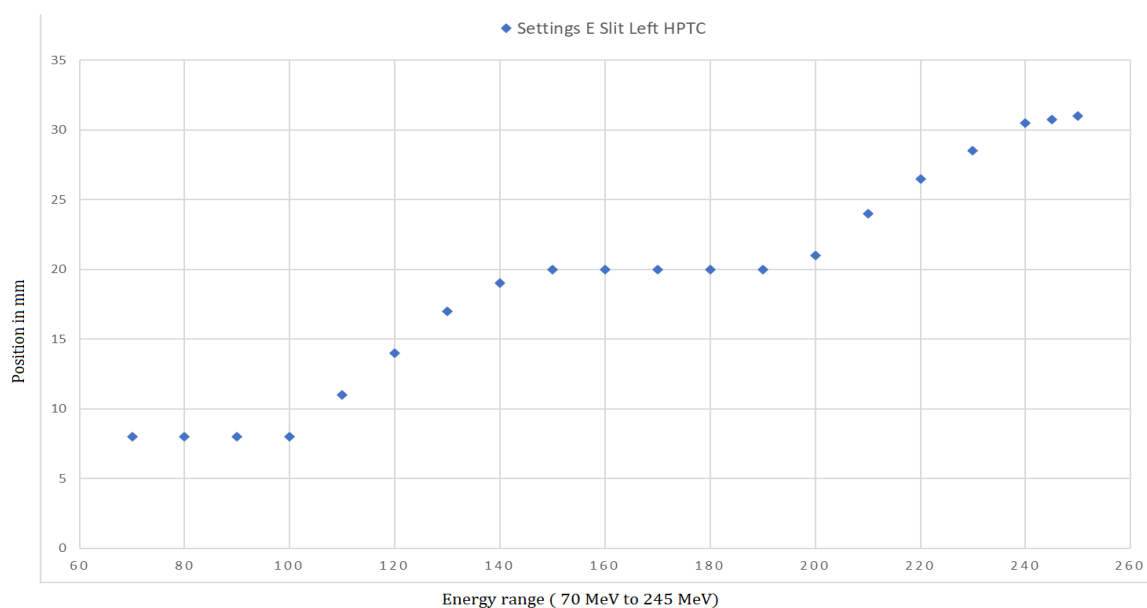
Figure 23: Commissioning of the energy slit in the HollandPTC. The slit position changes for certain energy ranges. A same graph is obtained for the right slit.

By taking only the contribution of the degrader and energy slit into account for the ELST, variations between the energies can be explained and no variation within an energy is expected. Nevertheless, in **Figure 17** variations are observed for each 2MeV energy range. There is variation within a day but also day-to-day which are both in the same extend. The measurements are done with the MatriXX, which can sample the data with a resolution of 0.04 seconds. Since the performance of the MatriXX is not analysed in our experiment, a deviation of ±0.04 seconds for each ELST is accepted for the MatriXX inaccuracy. But even with this deviation, large fluctuations in ELST are obtained. Variations of up to 0.36 seconds (=9 opg. files) are measured within a day for a beam. When looking at **Figure 18**, the day-to-day variations of the nine beams are visualized. We see that the mean ELST for all beams is within the 0.04 seconds acceptance interval. However, looking at the raw data again (*Appendix 3C*), large variations of up to 0.4 seconds (=10 opg. files) within an energy layer for one beam are obtained in some cases. For some energies (96-174MeV), larger variations in ELST are obtained compared to the highest (175-184MeV) and lowest (84-95MeV) energies, this could be due to the number of datapoints in those ranges: less data points were available for the high and low energy ranges hence less variation is observed compared to the energy ranges in the middle.

In a study we found that the ELST is related to the network transmission speed of the concerned proton therapy centre [65]. That a network transmission speed fluctuates continuously is a common fact. To which extent this transmission speed is involved in the variation is unknown. However, it is conceivable that for each measurement, the processes required for an energy switch will vary as hitches and/or prolongations occur in the data feedback loop. Also, the hardware compounds (degrader, energy slit, magnets) in the beamline will have their own working speed, depending on the temperature, pressure and other environment factors. An exact reason for the variations within one day and day-to-day for specific beams is unknown. Due to our lack of knowledge, we contacted the vendor VARIAN. In the next chapter (*3.4.3: Contacting VARIAN*) the technical systems behind an energy switch are discussed.

3.4.2 | Beam On Time

The BOT showed variations within a day and day-to-day (see *Appendix 3E* and **Figure 19**), so did the ELST. However, smaller deviations are observed in the BOT within a day and therefore the variation seems more likely to be caused by the sampling rate of the MatriXX. For the day-to-day variation, theoretically the BOT should be shorter when the measurement was done with a fresh ion source (day 3) rather than with an old one (day 2). However, a more or less the same value for BOT is found for all the days. This could be due to the beam current which is always set to be a constant value for each energy layer. A reason for the variations (within a day and day-to-day) can be due fluctuation of the beam current around the desired number. Also, the temperature and pressure of the environment where the ionization chambers of the MatriXX are present could possible influence the BOT. The ionization process with the ionization chamber will depend on the number of particles available in the chamber and therefore the BOT may vary according to the environmental factors. Lasty, the surface of the MatriXX which causes some information loss, may contribute to the variation.

In *Appendix 3E*, BOT boxplots for the individual beams are shown. We see that the BOT strongly depends on the planned dose rather than the planned spots as the dose curve better agrees with the BOT pattern. The BOT is directly correlated with the output of the cyclotron. In the plots in *Appendix 3D*, we can see that the measured dose in mGy agrees with the planned dose in MU. Minor variations are visible, these variations may occur due to the sampling rate of the MatriXX. Also, the MatriXX's surface, which basically serves as build-up of 0.6cm WET can affect the measured dose.

A dose rate boxplot is created in which the measured dose is divided with the BOT for all the nine beams together (see **Figure 21**). We see that the dose rate is increasing towards the higher energies. This occurrence could probably also be due to the ESS and achromat (**Figure 24**): when a thicker part of the degrader wedges is inserted into the beamline (to reduce the energy), the protons will be more frequently lost and scattered leading to a beam which has a reduced flux and is more dispersed [29]. The number of protons which passes through the degrader will be decreased for the lower energies (thus less protons per area). After the degrader, diverging aperture is placed to focus the beam. Due to the scatter in the degrader, protons with undesired energies can be mixed in the proton beam. To filter the beam, the achromat is utilized. The bending magnets of the achromat system ensures protons are bent according to their energy which causes a spread beam after this magnet. Then the spread beam encounters the energy slit. We can imagine that much less protons will be present after the energy slit since this slit only allows ±0.5% of the energy spread through for all energies; especially for low energies when the beam has encountered the degrader where a huge proton lost is obtained. This is also what we see here in our results for the dose rate.

Also in some energy ranges, the variation in dose rate is large (**Figure 21**). The sampling resolution of the MatriXX seems to affect the dose rate too much as a variation of one frame in the BOT resulted in large variations in dose rate. By looking into the individual beam plans, we find that for the energies with large variations, a lower dose is planned, hence the impact of the MatriXX's sampling resolution on these data points is amplified.
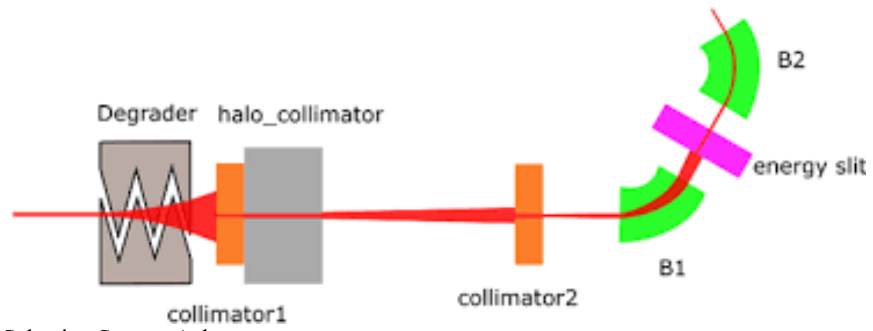
Figure 24: Energy Selection System Achromat.

3.4.3 | Contacting VARIAN: technique behind an energy switch

SENSITIVE INFORMATION OF VARIAN THIS PART OF THE REPORT IS HIDDEN

3.5 | Conclusion

In this study, the variation in ELST and BOT of the VARIAN proton machines is determined. We found that the ELST strongly depends on the energy. The mechanical parts that determine the ELST, e.g. step size for the degrader movement and energy slit movement, are determinant for the variation between the energies.

The exact reason for variations within an energy is unknown, as a lot of components contribute during an energy switch and any hitch in a component will affect the ELST. The within day variation and day-to-day variation are comparable.

Regarding the BOT, there are some variations, but overall a constant BOT is obtained. The BOT strongly depends on the planned dose: the higher the planned dose, the longer the BOT and vice versa. Variations are caused by the used measurement method and fluctuating in the beam current. The dose rate also depends on the energy: at higher energies a higher dose rate is observed than at lower energies because of the huge proton lost for low energies when interacting with the degrader.

Variations in target motion pattern

4.1 | Introduction

Besides the machine parameters, patient's breathing patterns also contributes to the interplay effect as the tumour is moving continuously due to breathing. According to the lung protocol of HollandPTC, the reference 4DCT is utilized to create a treatment plan. In the plan, the amplitude from the 4DCT is used for the maximal motion of extent for the tumour. An extra 5 millimetres robustness margin is used to account for deviations in position of up to 5mm. However, it is conceivable that variations of the breathing amplitude during the dose distribution can lead to mis-irradiation. Particularly, in the Pencil Beam Scanning technique where an ultra-fine beam is steered across the moving target [35]. Besides the amplitude, the period of the tumour movement and the degree of asymmetry/ shape of the tumour movement are also determinative for the dose distribution [67][50]. Variations in all three variables will lead to dose distributions which deviates from the actual plan.

In literature we found Lujan's tumour motion model: it is an one-dimensional model in which a periodic tumour movement is assumed with an oscillation along the craniocaudal axis [67]. Many studies investigated breathing patterns of lung patients using this model [74][75][76]. However, these studies were mainly population based studies. As breathing is an unique and patient specific occurrence, we decided to analyse the respiratory variation in craniocaudal direction patient specifically for our lung patients at the HPTC.

4.2 | Method

Prior to this experiment, permission of the Medical Research Ethics Committees Leiden The Hague Delft (MREC LDD) was required. The MREC checks and assesses medical research using human subjects. The following documents were part of the application: A1 Cover letter to review committee and competent authority; C1 Research protocol and E1/E2 Subject information sheet and informed consent form research subjects. After the approval (MREC -number N22.047), the study was executed. The E-forms are in Dutch and can be found in *Appendix 5A*. The number of patients included in the study and the number of measurements per patient which were done, depended on the number of lung patients eligible for proton therapy in the HollandPTC after approval was granted.

For this experiment, respiratory information of the included lung patients was collected from the reference 4DCT and weekly repeat 4DCTs. During these scans, the 3DCT was used in combination with the Anzai belt which gates the respiratory signal. The Anzai measured the stretch/ circumference change of the patient, which was subsequently used for binning the images into the corresponding phases as described in section *2.4.1: 4DCT Imaging*. The 4DCT scans of each patient were retrospectively analysed. For each scan the following information was retrieved:

1. period in seconds for all individual cycles within each 4DCT.
2. amplitude in millimetres for cranial-caudal direction from each 4DCT.

For the extra measurement, the patient was requested to remain in the radiation position on the CT coach after the standard procedure of the repeat 4DCT acquisition. Using the software programme AZ733VI 1.06, the patient's breathing was recorded with the sub-umbilically fastened Anzai belt for a duration of 1.5 minutes to determine the amplitude, period and degree of asymmetry. The output files were comma-separated values (csv) formatted files.

The Anzai belt only detects pressure changes in AP-direction, therefore it provided relative values in percentages for each change in extent of motion. To convert those values to millimetres in CC-direction, an AP-CC factor was used. To get this factor, amplitude information in CC of the priorly done 4DCT was used: from the extra measurement, all peak values were determined. The CC-amplitude of the 4DCT was subsequently divided by the mean value of all peaks of the extra measurement. Thereafter, the Y-values of the signal (which provides information regarding the extent of motion) was multiplied by this factor.

$$z(t) = -a \times cos^{2n}(\pi t/\tau) + a \qquad\qquad (1)$$

- $z(t)$ = position at time t
- a = the amplitude of the motion
- n = degree of asymmetry
- τ = period of one breathing cycle

In the Lujan's model a periodic tumour movement is assumed *(1)* [67]. However, we are interested in the variation within a breathing pattern. Hence, for each signal we looked per cycle to the relevant variables: in Python the least-squares fitting method was utilized between each breathing cycle within a 1.5 minute signal and Lujan's model. From this fit, the best-fit parameters in the Lujan's model for period (in seconds), amplitude (in millimetres) and degree of asymmetry was obtained. In *Appendix 4C* a section of the script is attached. In **Figure 26** a block diagram of the undertaken steps in the script can be found.
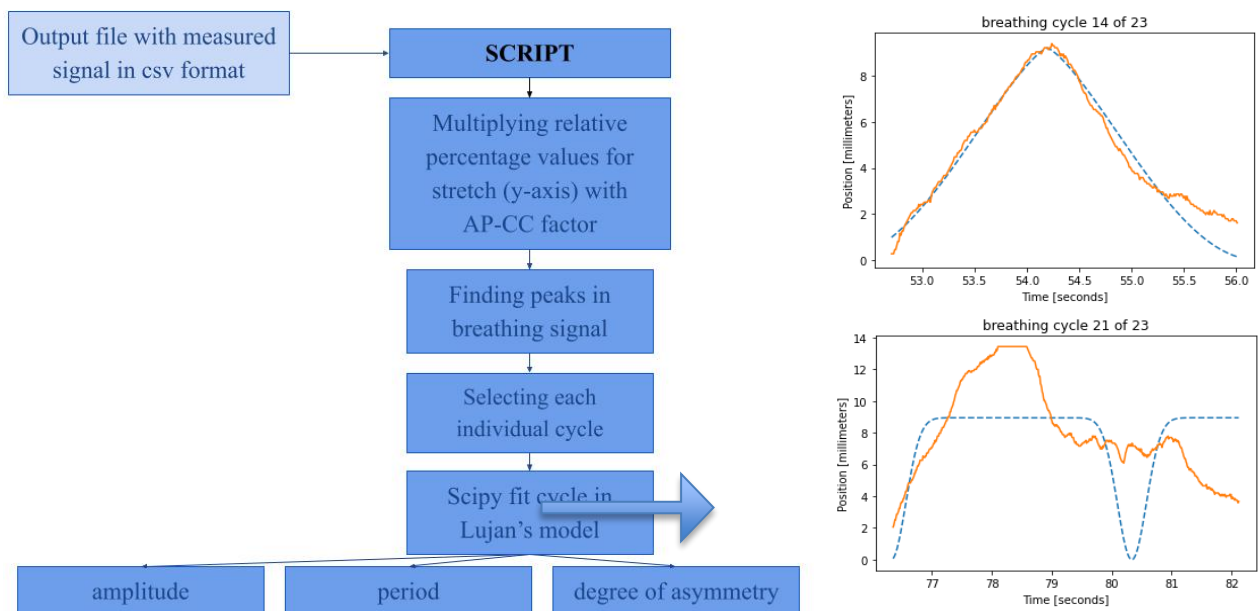
Figure 25: Block scheme for Python script on the right. An output file in csv format of the Anzai measurement is run into the script. The script firstly multiplies each Y value of the signal with the corresponding AP-CC converter factor. Thereafter, peaks

within the respiratory signal are obtained to automatically select cycles. Each cycle is then fitted into Lujan's model in terms of period, amplitude and degree of asymmetry using the Scipy optimize curve fit function. This function is available in Python and is used to find the best-fit parameters for amplitude, period and degree of asymmetry using a least-squares fit for each measured breathing cycle with the Lujan's model. On the left: worst- and best-case scenario for the fit, orange curve is the original signal, blue curve is the fit. When a poor fit is obtained, a manually fit is done by changing each value for amplitude, period and degree of asymmetry.

After the fit, the retrieved values for period, amplitude and degree of asymmetry were used to estimate the Probability Density Function (PDF) for the concerned parameter of the patient. PDF is a function that provides the likelihood that the value of a variable will fall between a certain range of values. The integral of the PDF over the entire space is equal to 1.

For each patient, multiple measurement sessions for both 4DCT and extra measurement were done. For our analysis we looked per patient at the intra-session variation and inter-session variation in period, amplitude and degree of asymmetry.

4.3 │ Results

From the 25th of April till the 20th of May 2022, the breathing patterns of four lung patients (A, B, C, D) were collected and analysed by 4DCT in HollandPTC. In addition, seven extra measurements were executed: one patient (C) had one extra measurement, two patients (A, D) had two extra measurements and one (B) had three extra measurements. Due to failures in the measurement tools, only five extra measurements could be analysed: one extra measurement for one patient (D) and two extra measurements for two patients (A, B). Thus, only three patients (A, B, D) were included for this part of the analysis. The signals of the extra measurements were fitted into Lujan's model. The obtained values can be seen in the figures below. In *Appendix 4A*, the Probability Density Functions for the period retrieved from the all the repeat 4DCTs till the 20th of May of all patients (A, B, C, D) are visualised. Also, a table for the peak-to-peak amplitude during each 4DCT is shown in *Appendix 4B*.

For patient A, large fluctuations in amplitude are observed during both measurements (**Figure 27**). However, for both days the amplitude vary in the same range. Regarding the period of this patient's breathing, a shifted plot is obtained for the seconds measurement towards the first one. In *Appendix 4A*, results of the 4DCT retrieved periods for all patients are shown. For patient A, we again see that the plots are shifted to right when the patient is further in its trajectory. Concerning the shape: a comparable degree of asymmetry is obtained for both measurements in patient A. In patient B (**Figure 28**), the variation in amplitude is much smaller compared to patient A. Also, the period seems more stable (also see *Appendix 4A*), hence minimal day-to-day variations are observed for this patient: all values are within the same range. In patient D (**Figure 29**) only one extra measurement was executed, therefore inter-session analysis could not be done. For the intra-session observations: again a smaller variation in amplitude and degree of asymmetry is obtained compared to patient A. Overall, we see that the amplitude, period and degree of asymmetry varies from patient to patient and in some patients a strong day-to-day variation can be observed (**Figure 30**).
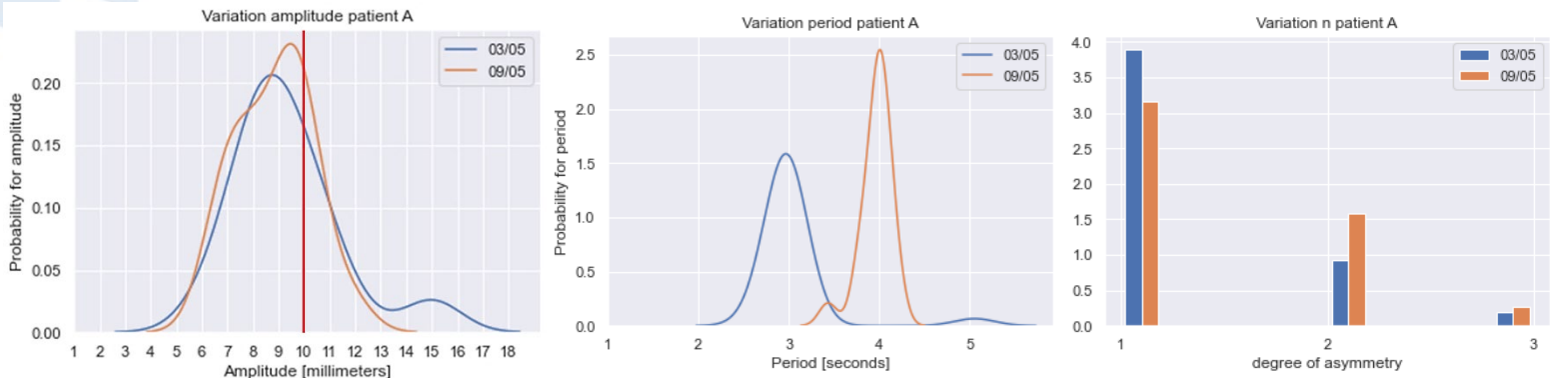
Figure 26: Results for Patient A. Probability Density Functions for the variation in amplitude (vertical red line represents the peak-to-peak amplitude in reference 4DCT) and period. Frequency histogram for the variation in degree of asymmetry.
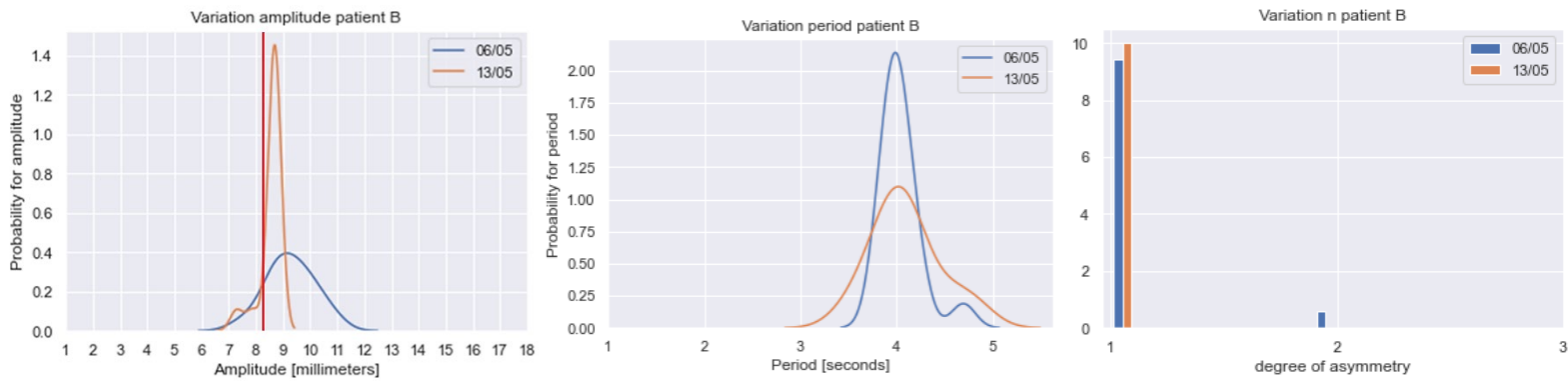
Figure 27: Results for Patient B. Probability Density Functions for the variation in amplitude (vertical red line represents the peak-to-peak amplitude in reference 4DCT) and period. Frequency histogram for the variation in degree of asymmetry.
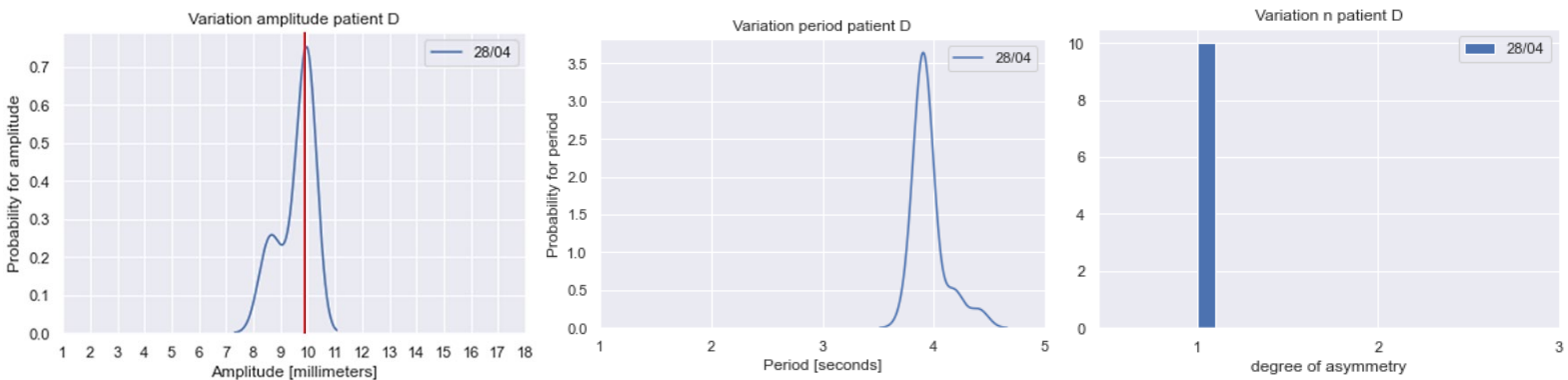
Figure 28: Results for Patient D. Probability Density Functions for the variation in amplitude (vertical red line represents the peak-to-peak amplitude in reference 4DCT) and period. Frequency histogram for the variation in degree of asymmetry.
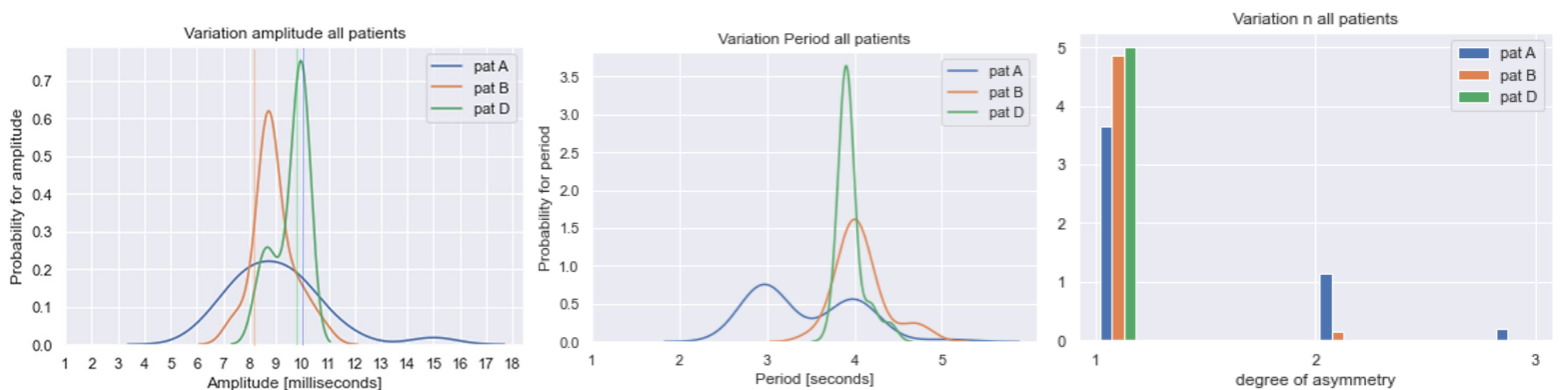
Figure 29: Results for all patients. Probability Density Functions for the variation in amplitude and period. Frequency histogram for the variation in degree of asymmetry.

4.4 | Discussion

During the research period, the HollandPTC 4DCT protocol changed: the frequency of the CTs is reduced from weekly to once in the two weeks. Hence less data is obtained than intended.

The mentioned results are retrieved from fitting the raw signal into the Lujan's model [67]. In this way we would like to model a patient breathing utilizing a model which can combine the fluctuations in each variable. A drawback of the used strategy is the laborious fit for breathing cycles which show disturbed patterns. In the raw signal, abnormalities in breathing patterns are perceived (**Figure 31**), hence an extended cycle obtained. In some cases irregular patterns/ hiccups and 'phase jumps' are observed, which are typical phenomena for diseased lungs [68][69]. Particularly, when the patient is further in the trajectory, those patterns are more observed (e.g. due to the impact of the treatment). Nevertheless, prior to the extra measurements, each patient is informed according to the non-WMO research law. Questionable is the possible bias which occurred due to this informed consent: the patients were aware of the respiratory monitoring which can potentially lead to an unusual breathing during the measurement.

Figure 30: Abnormalities in raw respiratory signal.

The respiratory signals were measured utilizing the Anzai belt. This belt only gates the respiratory signal as circumference changes of the patient. Since this is no direct measure for tumour motion, a degree of uncertainty is involved. For this experiment an arbitrary factor is calculated based on the priorly done 4DCT. The reliability of the calculated linear AP-CC factor is ambiguous, as for this calculation we assumed similar patient breathing patterns during the 4DCT and the extra measurement. Moreover, since the Anzai belt is attached at the lower abdomen (sub-umbilically), the breathing technique of the patient may also be responsible for the changes in the calculated factor. Also, the patient's comfort level may have an impact on the breathing: this can be increased in the course of the treatment trajectory and is possibly visible as period shifts to the right e.g. in patient A, **Figure 27** and *Appendix 4A*.

The HollandPTC uses a robustness margin of 5mm on the ITV+2mm to account for deviations in tumour position, however in **Figure 27**, much larger deviations in amplitude are obtained for patient A. This could also be the case for the other patients, as we do not know to which extent a signal of 60 seconds will cover the breathing variation during a full treatment. The extra measurement is just a snapshot for a fraction of time. Even in this small fraction of time, large respiratory variations are observed.

Also, localisation and path of the tumour motion will have a great impact on the breathing variables. This is also visible in *Appendix 4B* where the peak-to-peak amplitudes retrieved from the 4DCT are shown.

When the tumour is attached to surrounding rigid tissue (e.g. bronchus) or located in the upper part of the lung, less motion is obtained than when it is located in the lower region of the lungs [70]. Moreover, smaller tumours seem more likely to move in an ellipsoid pattern than larger ones [71][72], therefore information regarding the other two directions would also be relevant so a more accurate dose distribution assessment could be realized.

We see huge interpatient variation in terms of amplitude and period. A general value with a deviation will not be realistic enough to cover a patient specific respiratory induced tumour motion. Although there are also some differences observed between the inter-session measurements within a patient, those are more corresponding to each other than signals of other patients, mainly for the amplitude.

In the in-house developed Interplay Analysis QA tool, the focus is placed in CC-direction, hence our study only investigated the breathing variation in CC-direction. As the present model is only one-dimensional, a simple linear assumption from AP to CC is accurate enough. Computational studies also show that for interplay dose distribution analysis no difference is obtained when a simple breathing model is used versus an artificial patient-specific realistic breathing model in 1D [73]. In future developments, the software will be expanded to higher dimensions, then it would be appealing to analyse the variation in other directions in a more decent way e.g. taking phase differences into account via 4DCT. Even if the used method does not provide true values, it is a good approach to get information regarding the variations in respiratory variables.

4.5 | Conclusion

We found that the variation for each respiratory variable is patient dependent. Generally, the tumour characteristics are relevant for amplitude. For our group the amplitude variated between 6 and 12mm and the period variated between 2.5 and 4.5 seconds. The degree of asymmetry was most likely to be 1. In summary, we successfully determined the variation in the relevant breathing parameters patient specifically.

General Discussion

The HollandPTC is working on a software which can be used for interplay analysis. The software assesses the robustness of our plans to interplay effect by taking a periodic sinusoidal breathing pattern into account. To implement fluctuations in relevant parameters to this software (to make the assessment more realistic), the variations in concerned parameters are investigated. We divided the parameters into machine and patient parameters. Since no information is available for the VARIAN machines, we aimed in our work to examine the variations in ELST and BOT. Our investigation provides the first insights towards the fluctuation in ELST and BOT in the VARIAN machines. More measurements, with different energy ranges and/or step sizes are required to have a more precise estimation or approach for the ELST in each energy range. If more data can be obtained, an appealing tool which can predict the probable ELST for each energy in a plan can be initialized. Also, for future studies, machine log file analysis is recommended. As the MatriXX is only capable of measuring the plans with a resolution of 0.04 seconds, other BDT parameters with a much smaller time were not measurable. Contacting VARIAN regarding the results, yielded to not much extra information. In short, VARIAN was not aware of the strong variations in ELST within an energy. Bases on our research we encourage to measure interplay on a system itself and to base the acceptance-criteria for interplay also on real measurements of a system and not only on computational work.

Regarding the patient parameters: since the respiratory fluctuations strongly depend on the patient and tumour characteristics, we recommend determining their impact on the interplay effect patient specifically instead of taking an average population value. Since the variables within a patient can show variations, longer measurements are advised to get a more complete overview of the respiratory pattern, which covers the fluctuations of a larger time period.

Variations (within limits), have positive effects on the interplay. Each form of variation in motion leads to an extra blur in the dose distribution: it is comparable with a larger spot size effectively which actually ensures increased robustness for interplay. After collecting this data, an interesting step would be the implementation of those variations into our Interplay Analysis software. For each variable of the patient parameters a Probability Density Function is made. Those functions work in different directions in X, Y and Z on the tumour position and hence dose distribution. After determining on which direction each parameter has an effect, all PDFs should be grouped based on their working direction. A Point Spread Function of all the PDFs could be created. The PSF is basically the probability function for all parameters in all directions together. This function can subsequently be convoluted with every pixel/ voxel of the integral dose distribution map. The same can be done for the beam parameters, however a more promising way would be creating a prediction tool which can accurately estimate the ELST and BOT for each layer. Currently, only variations relevant for the CC-direction (Y-direction) are investigated. Analysing the variation in other direction and adding this to the other directions would be engaging for the interplay assessment. In a later stadium, the tool can be used for clinical use by taking an advising or decisive role: e.g. if insufficient robustness of the plan is obtained, plan adjustments is advised/ required.

General Conclusion

In this thesis report a strategy to determine variations in beam and patient specific parameters relevant to the interplay effect, was elaborated. Our research provides us the first insights towards the fluctuations in the relevant parameters: we determined the variation in our VARIAN machine and also an impression regarding the variation in patient specific breathing was obtained for our lung patients.

The retrieved information is useful for the in-house developed interplay simulation, and therefore it can be used to optimize this tool. By implementing the obtained variations into our QA tool, it is believed that a more realistic interplay assessment could be performed.

Appendix A ⏐ Staging

DISTANT METASTASIS (M)

Stage IV B (Any T, Any N, M1c)	M1c	Multiple extrathoracic metastases (in one or more organs)
Stage IV A (Any T, Any N, M1a/b)	M1b	Single extrathoracic metastasis (including non-regional lymph nodes)
	M1a	Satellite (separate) tumor nodule(s) in contralateral lobe or Pleural or pericardial nodules or malignant effusion
Distant metastasis	M1	
No distant metastasis	M0	

LYMPH NODE (N)

Explanation of lymph node staging:

- For any N category, one or more of the groups marked by ● must be involved and the involvement of all groups marked by ⊟ should be absent.

- The presence or absence of involvement in groups marked by ▦ does not alter N staging in the corresponding category.

Lymph node groups (columns): Scalene (ipsi./ contralateral), Supraclavicular, Hilar (Contralateral), Mediastinal (Contralateral), Subcarinal, Mediastinal (Ipsilateral), Hilar (Ipsilateral), Peribronchial (Ipsilateral)

N	Scalene	Supraclav	Hilar(C)	Mediast(C)	Subcarinal	Mediast(I)	Hilar(I)	Peribr	Stage
N3	●	●	●	●	▦				Stage III B / Stage III C
N2	−	−	−	−	●	●			Stage III A / Stage III B
N1	−	−	−	−	−	−	●	●	Stage II B / Stage III A
N0	−	−	−	−	−	−	−	−	I A1, I A2, I A3, I B, II A, II B

PRIMARY TUMOR (T)

	T1a	T1b	T1c	T2a	T2b	T3	T4
	T1			**T2**		**T3**	**T4**
	I A1	I A2	I A3	I B	II A		
						II B	

Stage I A1 (T1 (mi) N0 M0)

T1 (mi): Minimally invasive adeno-carcinoma (solitarey adenocarcinome, ≤ 3 cm with a lepidic growth and ≤ 5 mm invasion in any focus

Stage 0 (Tis N0 M0)

Tis: Carcinoma in situ

Occult Carcinoma (Tx N0 M0)

Tx: Tumor is proven histopathologically (+ Cytology) but not detected by imaging or bronchoscopy)

2- Criteria of Extent

	T1a	T1b	T1c	T2a	T2b	T3	T4
1- Size (greatest dimension)	≤ 1 cm	> 1 cm ≤ 2 cm	> 2 cm ≤ 3 cm	> 3 cm ≤ 4 cm	> 4 cm ≤ 5 cm	> 5 cm ≤ 7 cm	> 7 cm
				or Any size ≤ 5 cm in the presence of 1 or more of the criteria of extent *		or Any size ≤ 7 cm in the presence of 1 or more of the criteria of extent	or Any size if 1 or more of the criteria of extent are present
Endo-bronchial Location	No extension proximal to the lobar bronchus **			Main bronchus (regardless of the distance to the carina)** vs. Atelectasis or obstructive pneumonitis extending to the hilum (entire or part of the lung)			Carina or Trachea
Local Invasion	None; the tumor is surrounded by lung or visceral pleura			Visceral pleura		Chest wall (Including superior sulcus), phrenic nerve, parietal pleura and/or parietal pericardium	Diaphragm, Mediastinum, heart, great vessels, recurrent laryngeal nerve, esophagus and/or vertebral body
Separate Tumor Nodule(s)	Absent			Absent		Present in the same lobe of the primary tumor	Present in a different ipsilateral lobe

* : The tumor is classified as T2a if ≤ 4 cm in size (or size cannot be determined) and T2b if > 4 cm and ≤ 5 cm

** : The uncommon superficial spreading tumor with invasion limited to the bronchial wall is considered T1a regardless of size and extension proximal to the main bronchus

Appendix A | Clinical Treatment Plans

In the tables below data of the three RT plans are shown. Each plan contains three beams, and each beam contains a planned number of energy layers. Each energy layer is made up of multiple spots with a certain planned dose.

Patient A									
	Beam 1			Beam 2			Beam 3		
Energy layer No.	Energy [MeV]	Dose [MU]	No. of spots	Energy [MeV]	Dose [MU]	No. of spots	Energy [MeV]	Dose [MU]	No. of spots
1	167,9	235,3	20	160,3	21,3	2	186	198,4	17
2	165,7	488,9	42	158,1	72,6	7	183,6	327,7	28
3	163,5	567,3	47	155,9	245,6	26	181,2	377,1	31
4	161,3	708,6	65	153,7	439,5	37	178,8	338,5	29
5	159,1	754,1	59	151,6	374,3	37	176,5	413,0	28
6	156,9	630,8	54	149,5	552,8	54	174,2	456,9	34
7	154,7	561,4	51	147,4	786,3	63	171,9	442,6	36
8	152,6	581,4	50	145,3	908,1	78	169,6	557,3	44
9	150,5	737,5	47	143,3	844,1	72	167,3	516,6	41
10	148,4	678,5	46	141,3	916,4	71	165	473,8	40
11	146,3	884,3	59	139,3	906,4	69	162,8	432,0	37
12	144,2	891,5	55	137,3	700,8	62	160,6	417,7	32
13	142,2	924,7	66	135,3	614,7	61	158,4	396,1	30
14	140,2	862,0	63	133,3	652,4	53	156,2	391,4	32
15	138,2	848,2	62	131,3	576,3	60	154	444,0	30
16	136,2	777,0	55	129,3	581,2	52	151,9	347,8	29
17	134,2	814,2	69	127,4	480,6	49	149,8	305,6	27
18	132,2	771,0	61	125,5	477,6	39	147,7	297,9	25
19	130,2	572,0	55	123,6	616,7	54	145,6	273,3	24
20	128,3	548,7	55	121,7	466,4	49	143,6	294,4	24

	Energy [MeV]	Dose [MU]	No. of spots	Energy [MeV]	Dose [MU]	No. of spots	Energy [MeV]	Dose [MU]	No. of spots
21	126,4	493,3	56	119,8	464,4	42	141,6	300,9	27
22	124,5	404,5	44	117,9	550,9	48	139,6	262,1	23
23	122,6	326,4	42	116	653,6	60	137,6	303,5	28
24	120,7	265,2	37	114,1	465,0	54	135,6	296,5	27
25	118,8	269,2	33	112,2	474,1	50	133,6	250,0	23
26	116,9	266,7	33	110,3	522,6	47	131,6	281,9	22
27	115	178,2	21	108,4	431,1	41	129,6	225,5	22
28	113,1	168,1	21	106,6	328,4	38	127,7	210,7	19
29	111,2	95,9	15	104,8	293,0	31	125,8	316,5	21
30	109,3	100,6	13	103	257,5	32	123,9	326,4	24
31	107,5	94,9	12	101,2	139,8	17	122	277,8	25
32	105,7	68,9	7	99,4	89,3	9	120,1	220,2	21
33				97,7	109,3	10	118,2	163,2	18
34				96	45,1	6	116,3	167,8	17
35							114,4	178,5	19
36							112,5	141,0	16
37							110,6	108,2	15
38							108,7	95,6	16
39							106,9	69,1	9
40							105,1	50,1	9
41							103,3	45,6	6
42							101,5	29,6	6
43							99,7	5,3	1

Patient B									
	Beam 1			**Beam 2**			**Beam 3**		
Energy layer No.	**Energy [MeV]**	**Dose [MU]**	**No. of spots**	**Energy [MeV]**	**Dose [MU]**	**No. of spots**	**Energy [MeV]**	**Dose [MU]**	**No. of spots**
1	174,5	228,8	31	152,5	11,4	2	167,9	108,3	14

2	172,2	309,1	46	150,1	207,4	22	165,5	213,6	30
3	169,9	383,5	55	147,7	576,1	55	163,1	421,4	54
4	167,6	709,9	76	145,3	692,8	69	160,7	372,6	50
5	165,3	734,9	81	142,9	706,3	81	158,3	576,7	58
6	163,1	726,1	86	140,5	1213,5	126	155,9	564,3	66
7	160,9	810,5	86	138,2	1070,2	124	153,6	723,7	85
8	158,7	666,7	73	135,9	1056,3	137	151,3	597,6	85
9	156,5	776,6	81	133,6	1208,9	141	149	878,0	98
10	154,3	815,9	85	131,3	1223,2	129	146,8	781,4	96
11	152,2	818,6	86	129	1237,4	143	144,6	783,2	97
12	150,1	699,8	81	126,7	1087,1	132	142,4	833,8	96
13	148	670,2	78	124,4	1113,2	136	140,2	813,6	103
14	145,9	624,1	81	122,2	938,8	120	138	828,5	114
15	143,9	765,7	90	120	851,1	118	135,8	750,7	104
16	141,9	821,8	94	117,8	938,6	114	133,7	698,5	100
17	139,9	821,8	93	115,6	863,0	116	131,6	809,3	102
18	137,9	717,2	89	113,4	909,3	117	129,5	786,1	92
19	135,9	754,3	93	111,2	816,6	108	127,4	657,7	97
20	133,9	677,1	99	109	777,5	107	125,3	798,1	88
21	131,9	634,2	86	106,8	654,6	92	123,2	912,6	96
22	129,9	507,7	77	104,7	592,5	94	121,1	705,1	85
23	128	455,3	74	102,6	471,3	73	119	577,4	86
24	126,1	439,2	70	100,5	408,5	68	116,9	509,4	75
25	124,2	329,6	59	98,4	330,1	62	114,8	475,7	74
26	122,3	300,9	57	96,4	276,2	47	112,8	403,8	65
27	120,4	302,3	50	94,4	195,7	36	110,8	313,8	54
28	118,5	222,5	38	92,5	150,4	26	108,8	256,2	44
29	116,6	139,2	27	90,6	56,4	13	106,8	228,3	36
30	114,7	121,4	22	88,8	26,6	6	104,8	141,7	26
31	112,8	86,2	19	87	19,8	5	102,8	64,5	9

32	110,9	50,8	10	85,2	11,3	3	100,9	28,5	5
33	109	27,2	6						

Patient C									
	Beam 1			**Beam 2**			**Beam 3**		
Energy layer No.	**Energy [MeV]**	**Dose [MU]**	**No. of spots**	**Energy [MeV]**	**Dose [MU]**	**No. of spots**	**Energy [MeV]**	**Dose [MU]**	**No. of spots**
1	175,9	18,1	3	162,8	98,0	13	169,6	56,2	7
2	173,4	84,1	14	160,2	275,6	31	167	238,3	24
3	170,9	283,4	29	157,6	687,9	68	164,4	592,2	56
4	168,4	424,1	47	155,1	1095,1	98	161,8	582,7	60
5	166	433,7	48	152,6	1400,2	139	159,2	563,9	66
6	163,6	293,4	34	150,1	1276,5	145	156,6	558,5	65
7	161,2	315,7	37	147,7	1357,0	161	154,1	745,5	75
8	158,8	314,7	38	145,3	1536,1	161	151,6	870,5	88
9	156,4	631,3	62	142,9	1698,1	181	149,2	1021,2	93
10	154,1	899,7	84	140,5	1685,3	175	146,8	1074,0	108
11	151,8	836,3	82	138,2	1488,1	161	144,4	1094,0	116
12	149,5	797,0	87	135,9	1471,6	167	142	954,2	102
13	147,3	831,7	99	133,6	1548,2	158	139,6	825,3	91
14	145,1	757,3	92	131,3	1522,6	171	137,3	807,9	95
15	142,9	822,6	109	129	1638,3	185	135	742,8	100
16	140,7	759,5	101	126,7	1817,2	186	132,7	718,2	95
17	138,5	689,4	96	124,4	1457,5	162	130,4	988,3	108
18	136,3	647,5	88	122,2	1202,2	151	128,1	953,2	114
19	134,2	552,4	79	120	1163,5	150	125,8	747,7	101
20	132,1	584,0	79	117,8	1121,6	148	123,5	861,9	105
21	130	488,8	69	115,6	1006,2	123	121,3	894,2	107
22	127,9	511,7	67	113,4	940,9	116	119,1	791,6	97

23	125,8	535,9	60	111,2	784,8	105	116,9	701,9	88
24	123,7	388,4	56	109	715,9	93	114,7	647,3	81
25	121,6	331,0	49	106,8	607,6	83	112,5	531,1	78
26	119,5	347,2	49	104,7	462,2	61	110,3	377,0	54
27	117,4	290,4	44	102,6	408,6	55	108,1	347,5	47
28	115,3	262,5	32	100,5	293,1	35	105,9	261,8	38
29	113,3	177,2	27	98,4	214,0	27	103,8	196,0	25
30	111,3	143,9	23	96,4	179,2	18	101,7	136,8	19
31	109,3	132,3	23	94,4	80,3	11	99,6	125,4	18
32	107,3	126,2	18	92,5	6,3	1	97,6	75,7	10
33	105,3	105,6	13				95,6	53,7	7
34	103,3	94,7	11				93,6	31,6	3
35	101,4	84,1	11						
36	99,5	52,8	7						
37	97,6	39,2	6						
38	95,7	13,8	2						
39	93,9	11,3	1						

Appendix B | Energy Layer Switching Time for each individual beam

In the boxplot below, the variation in ELST for each beam is visualised per energy layer. The blue line is the step size, which is defined as the required step in MeV to go to the next energy layer.

Boxplot ELST patient A, beam 1

Boxplot ELST patient A, beam 2

Boxplot ELST patient A, beam 3
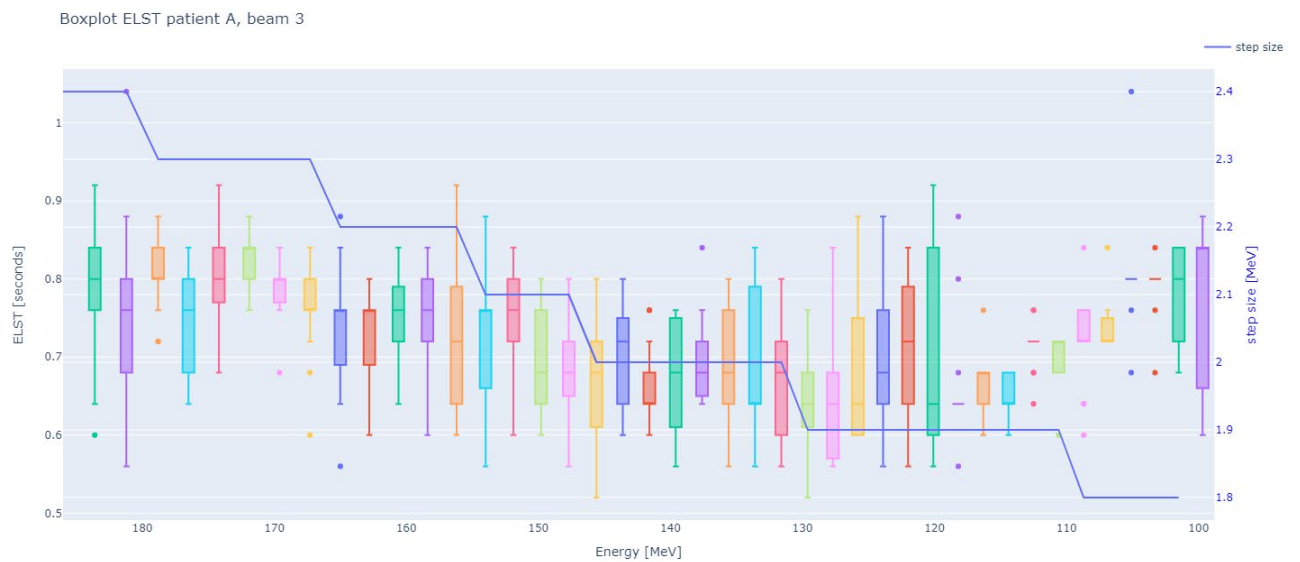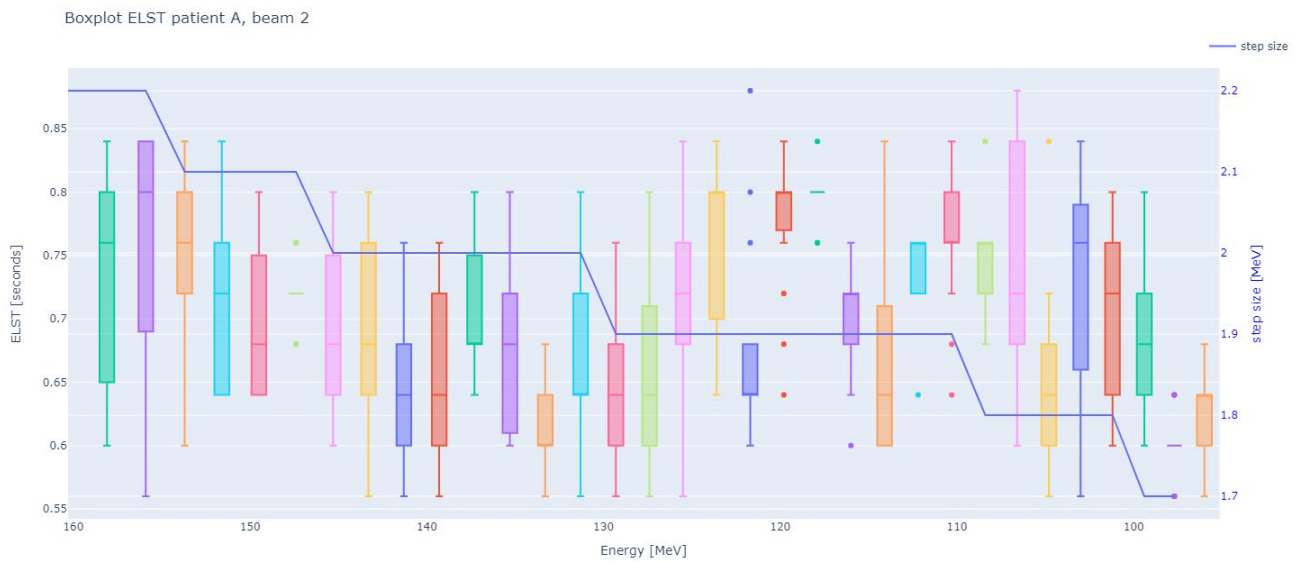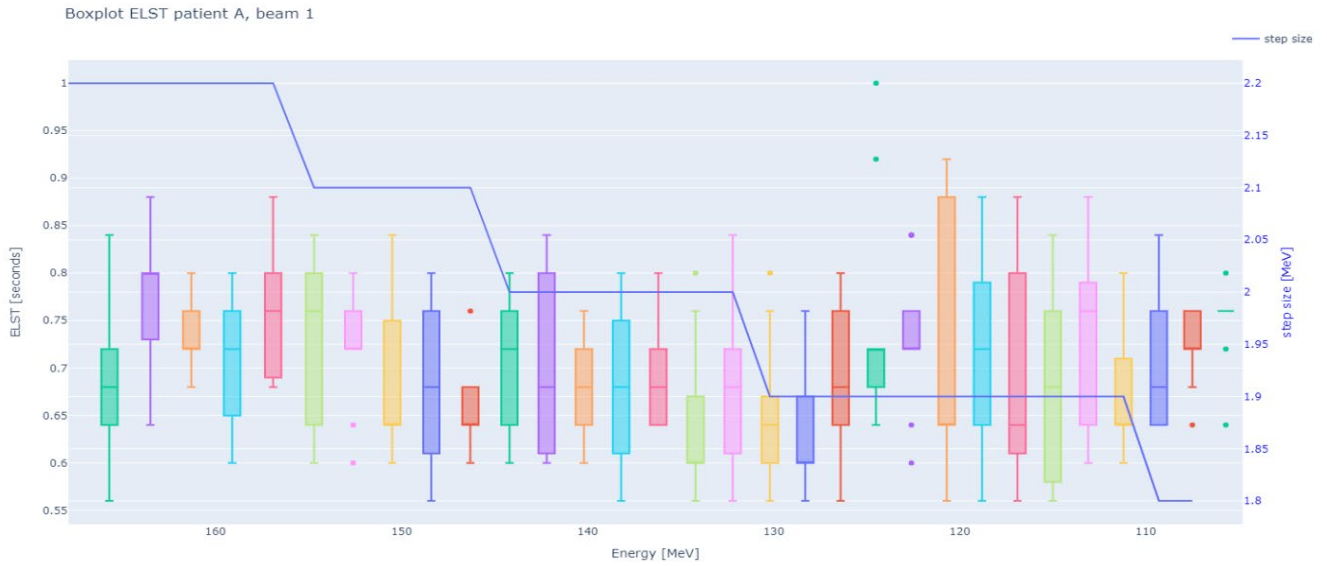
Boxplot ELST patient B, beam 1
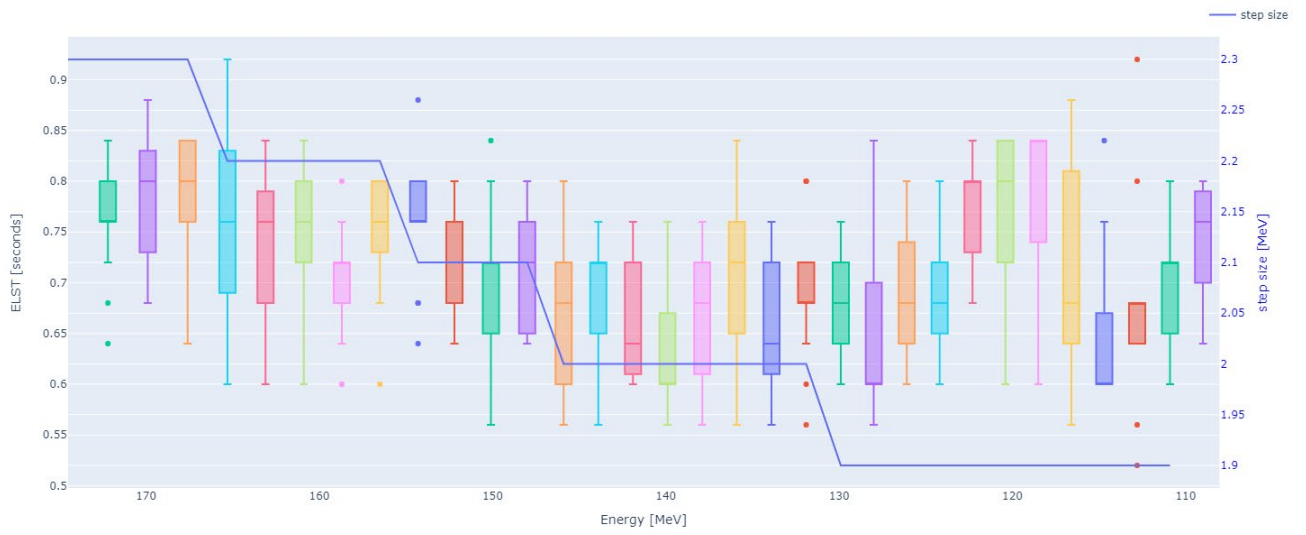
Boxplot ELST patient B, beam 2
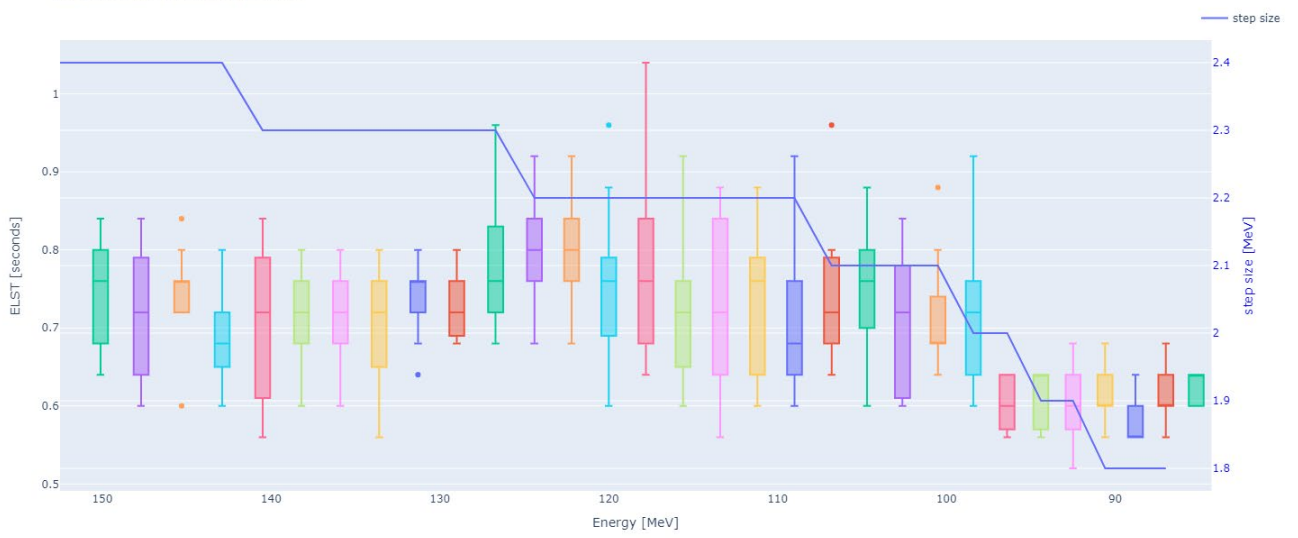
Boxplot ELST patient B, beam 3
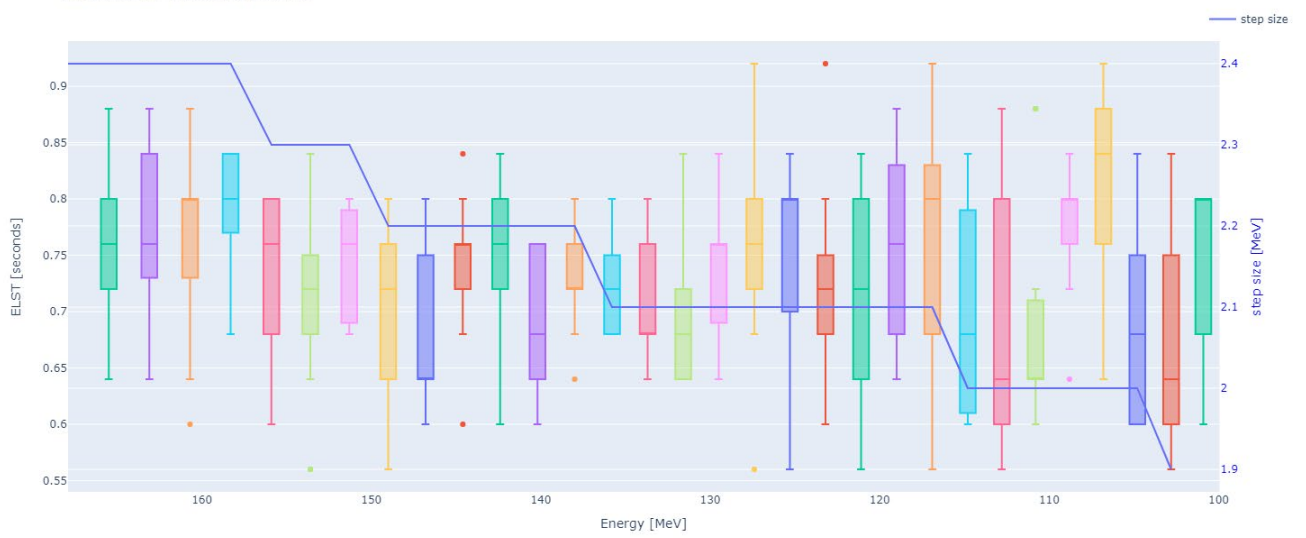
Boxplot ELST patient C, beam 1
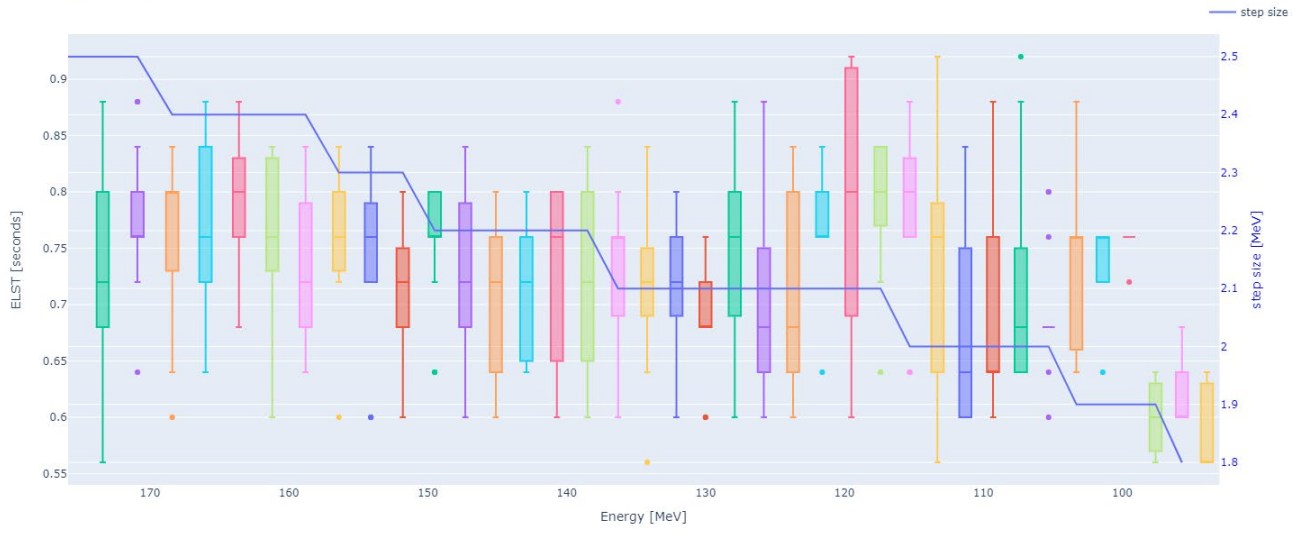
Boxplot ELST patient C, beam 2
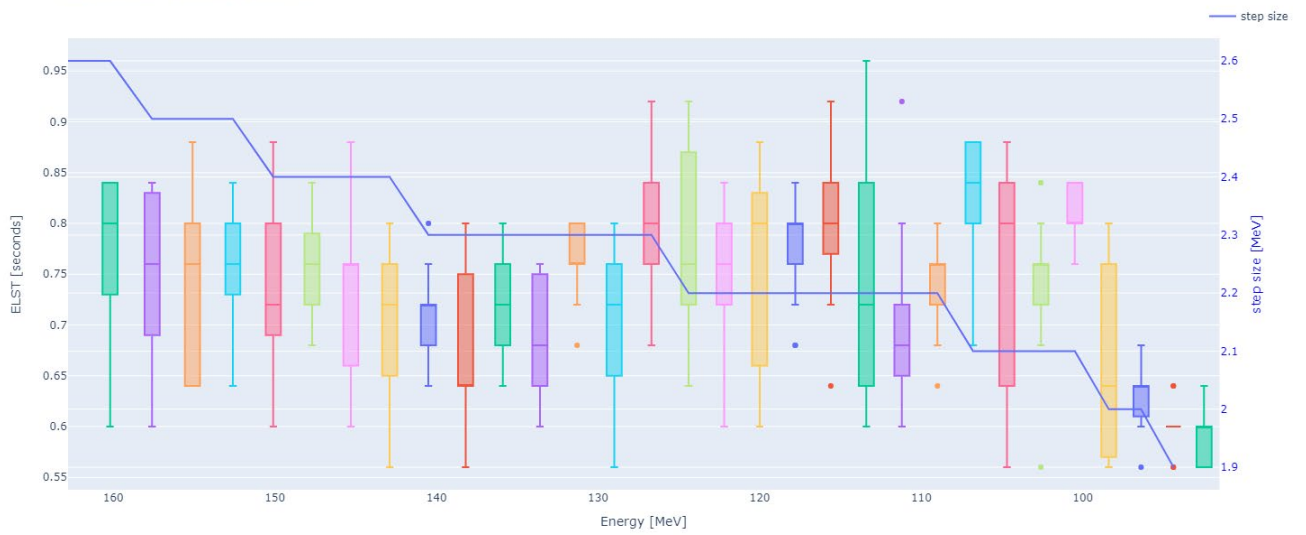
Boxplot ELST patient C, beam 3
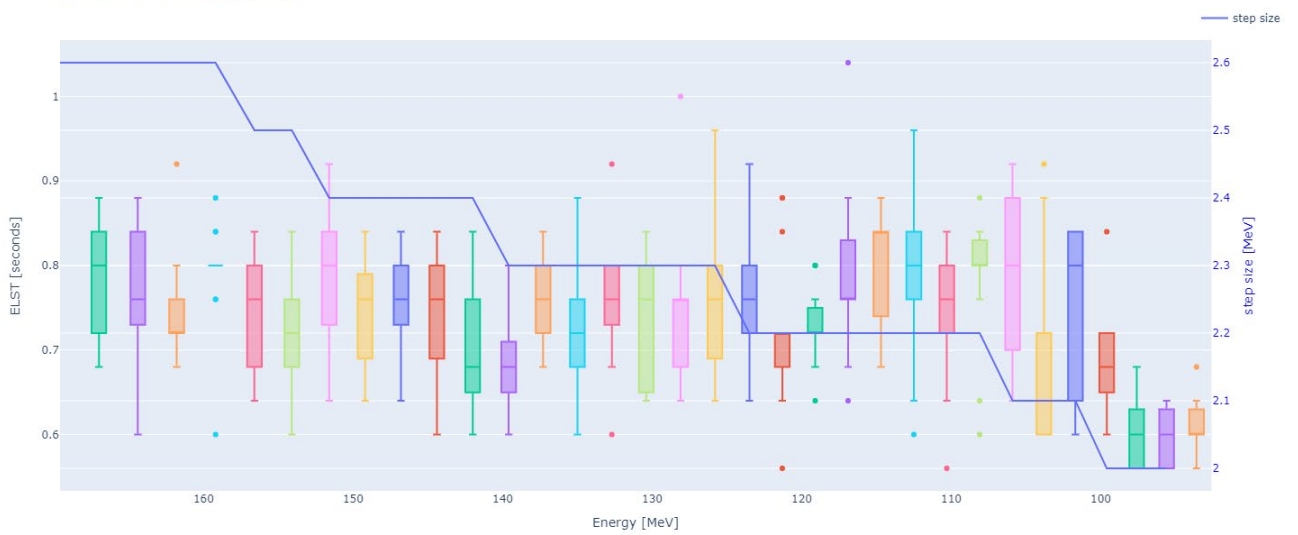
Appendix C ｜ Energy Layer Switching Time per step size for each individual beam

In the boxplots below the ELST is divided by the corresponding step size for each beam.

Boxplot ELST/step size patient A, beam 1
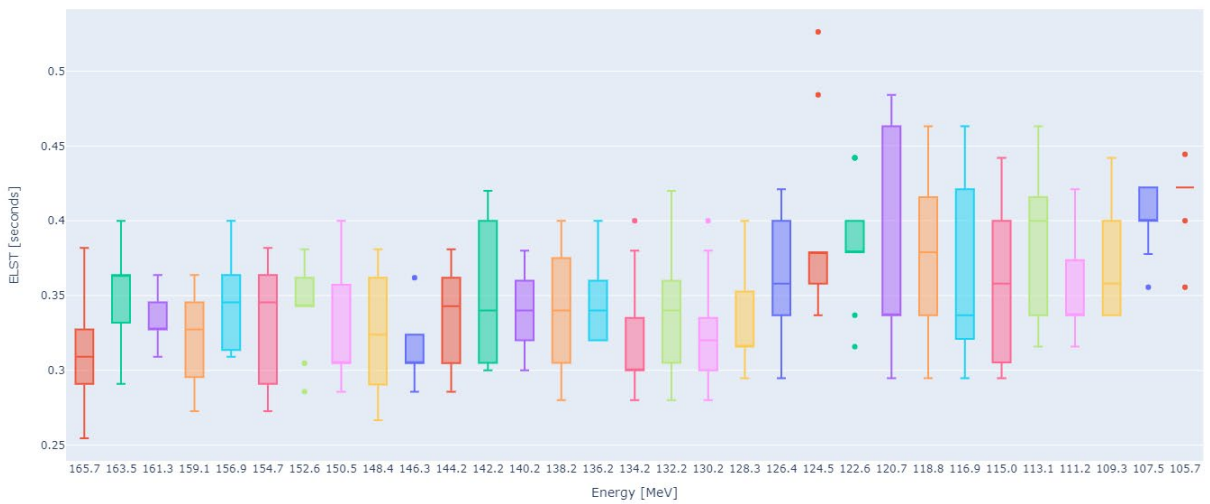
Boxplot ELST/step size patient A, beam 2
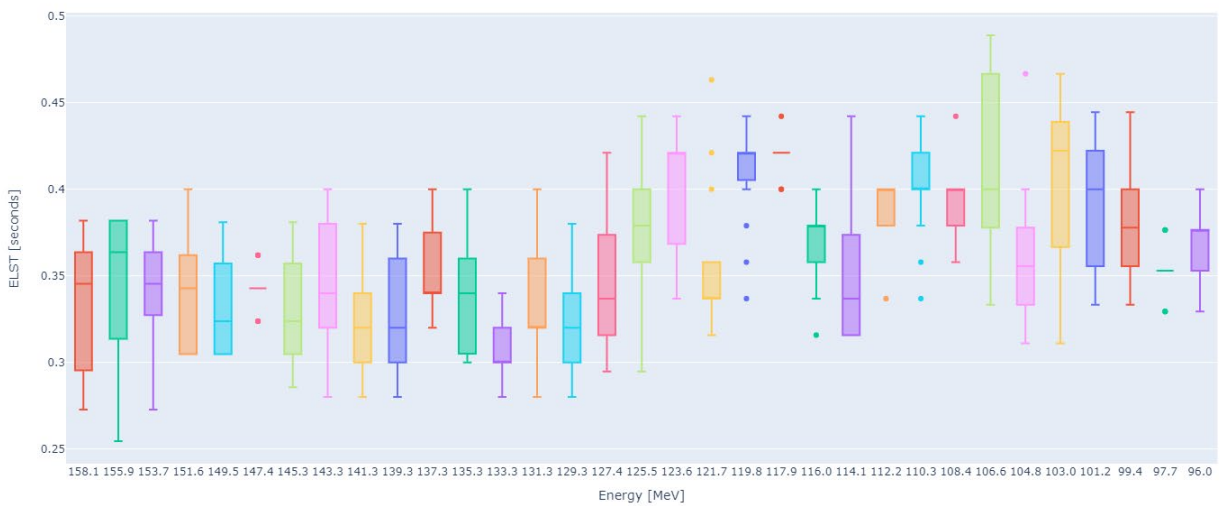
Boxplot ELST/step size patient A, beam 3
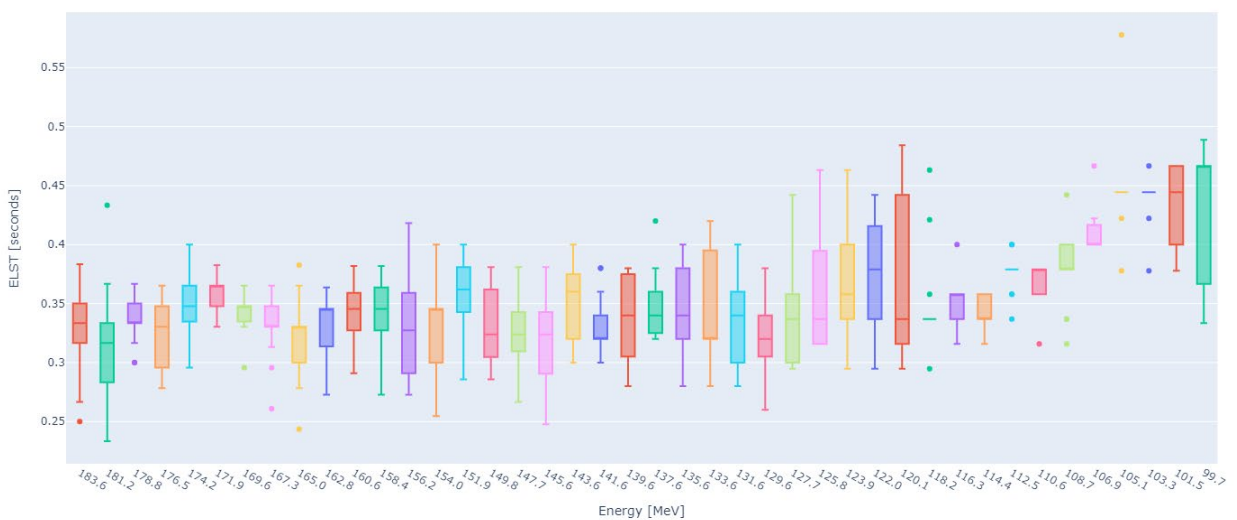
Boxplot ELST/step size patient B, beam 1
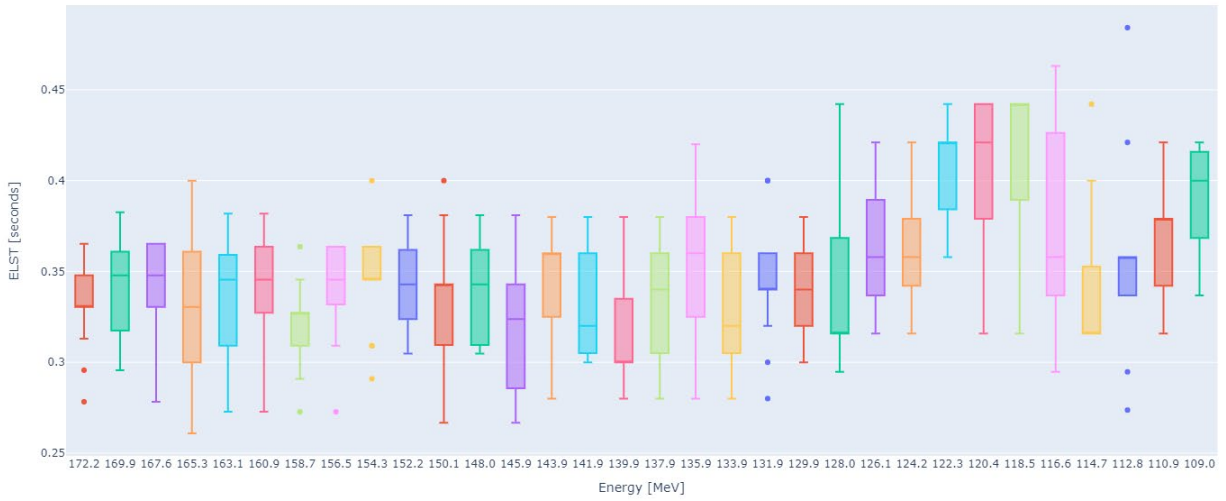
Boxplot ELST/step size patient B, beam 2
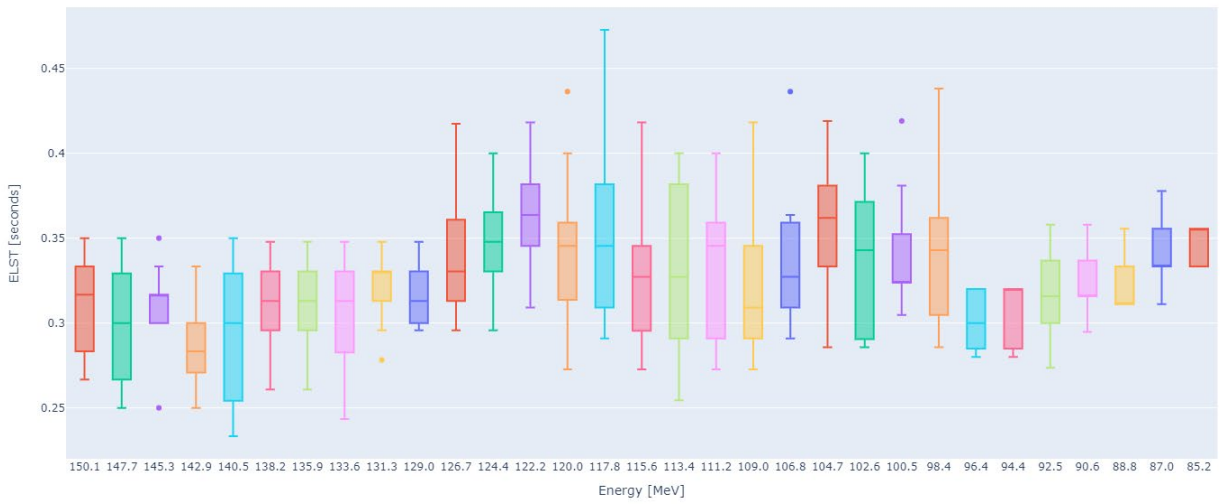
Boxplot ELST/step size patient B, beam 3
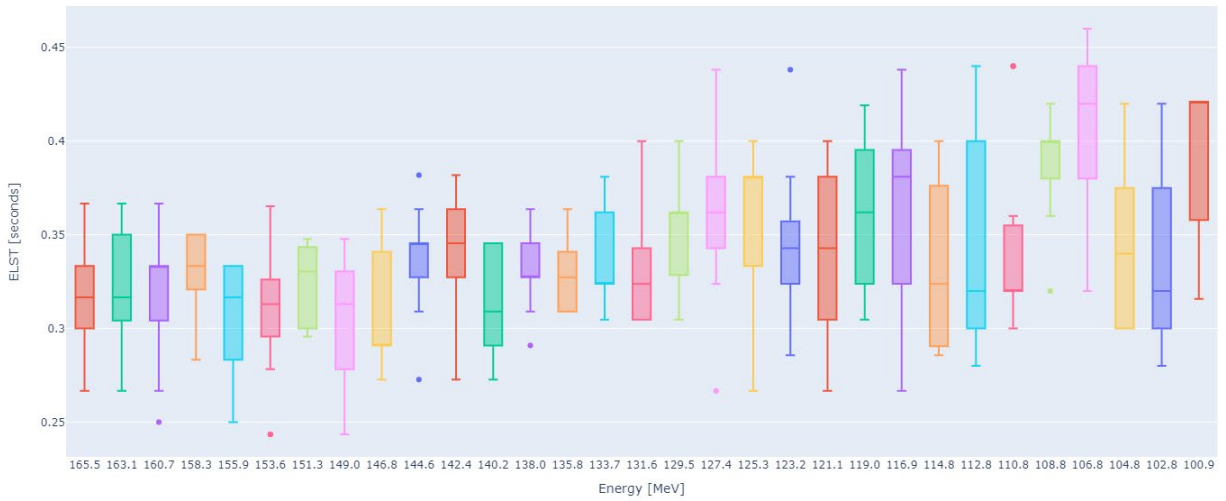
Boxplot ELST/step size patient C, beam 1
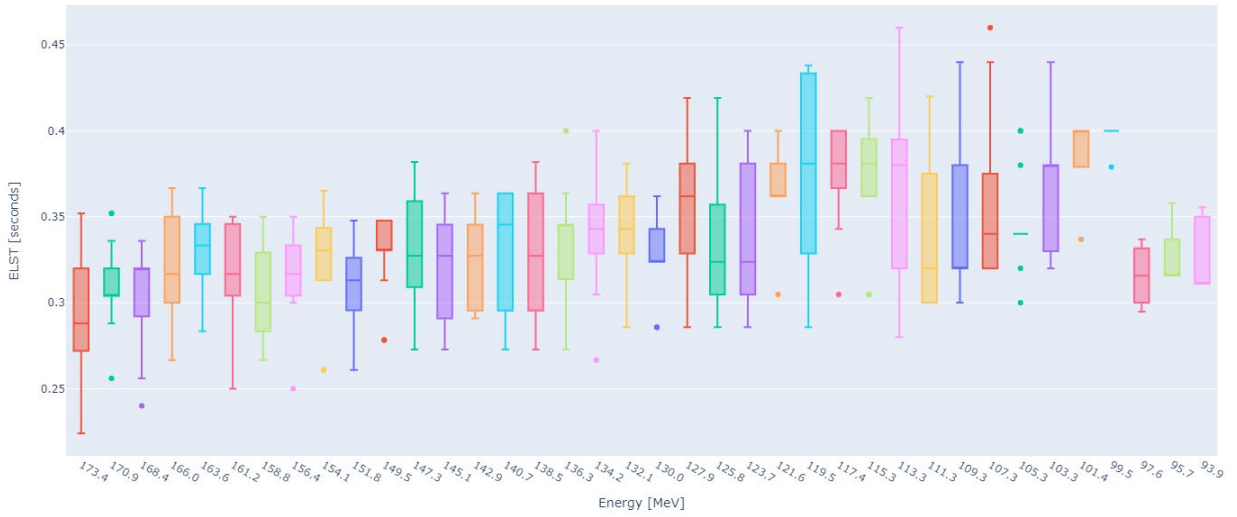
Boxplot ELST/step size patient C, beam 2
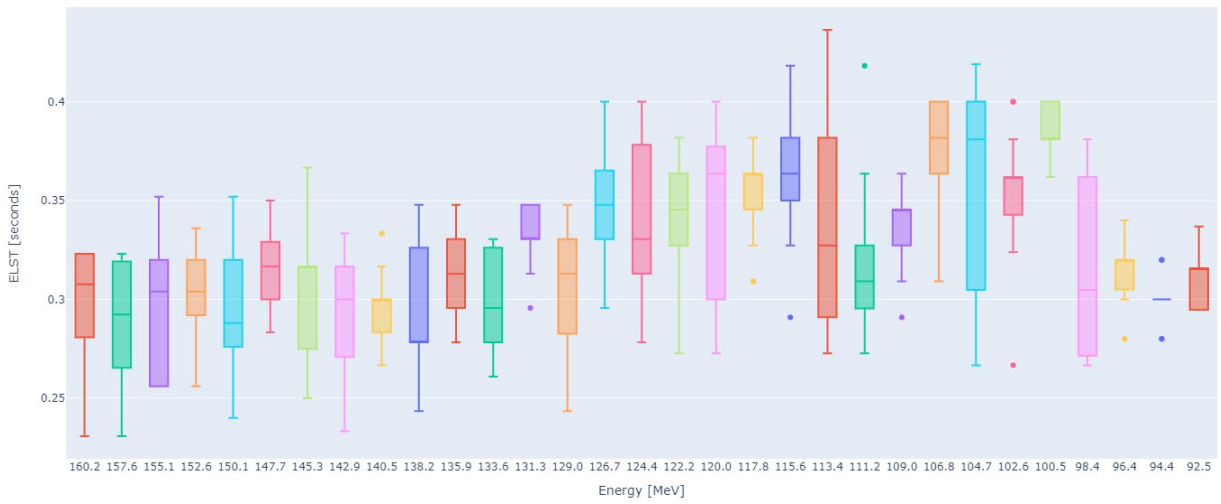
Boxplot ELST/step size patient C, beam 3
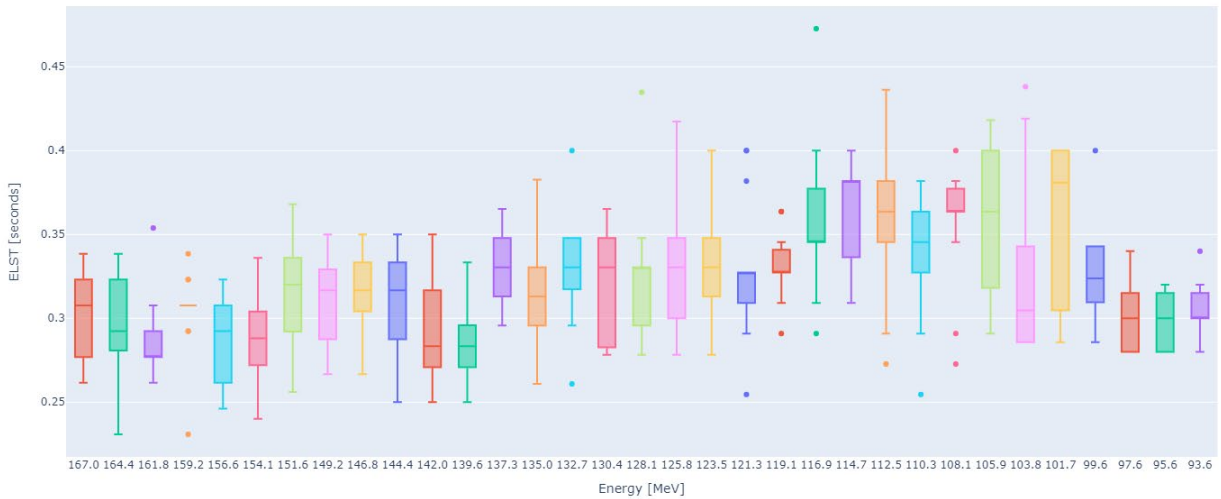
Appendix D │ Measured dose and planned dose for each individual beam

In the plots below for each beam, the measured dose in mGy is visualised per energy layer. Also the planned dose in MU retrieved from the RT plans are added to those plots as a blue line.

Boxplot dose patient A, beam 1

Boxplot dose patient A, beam 2

Boxplot dose patient A, beam 3
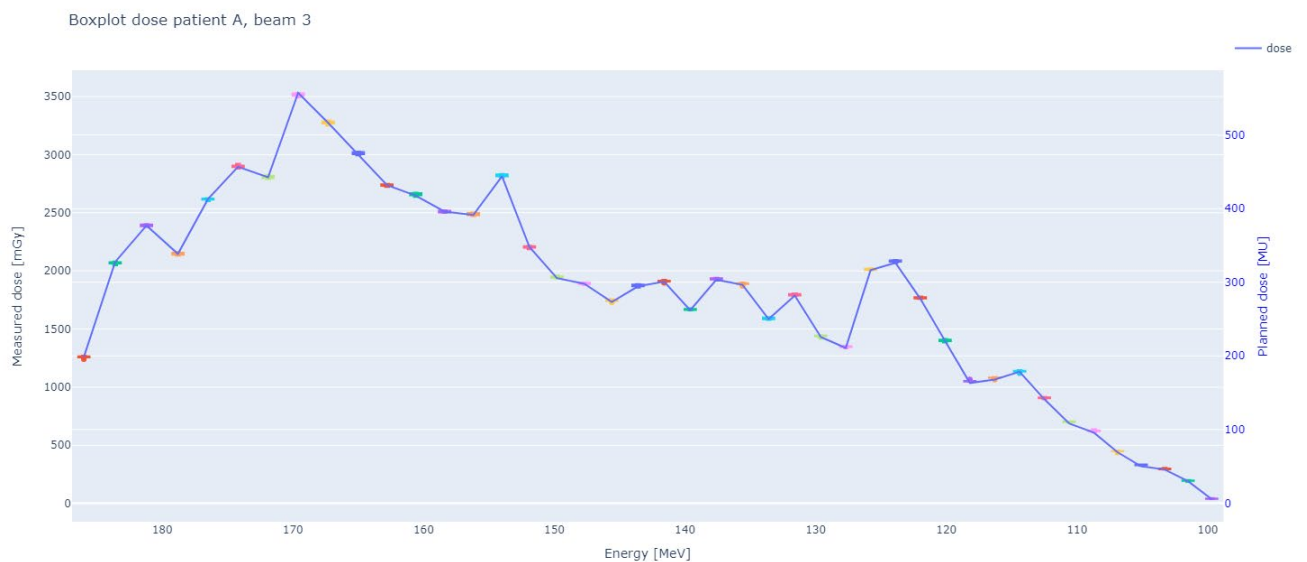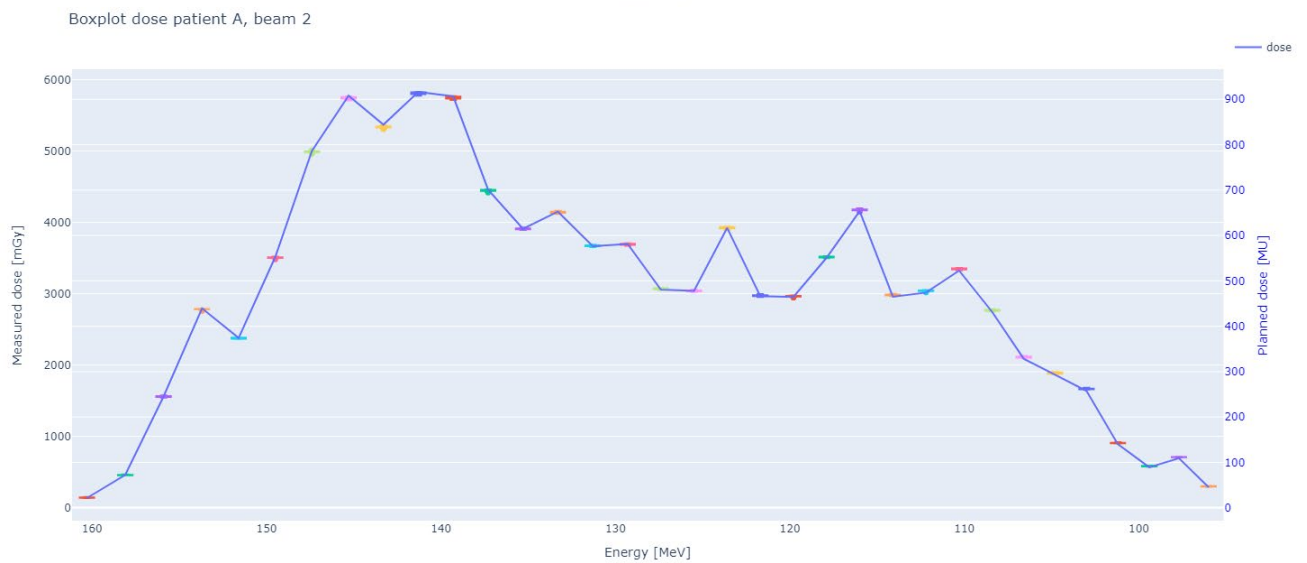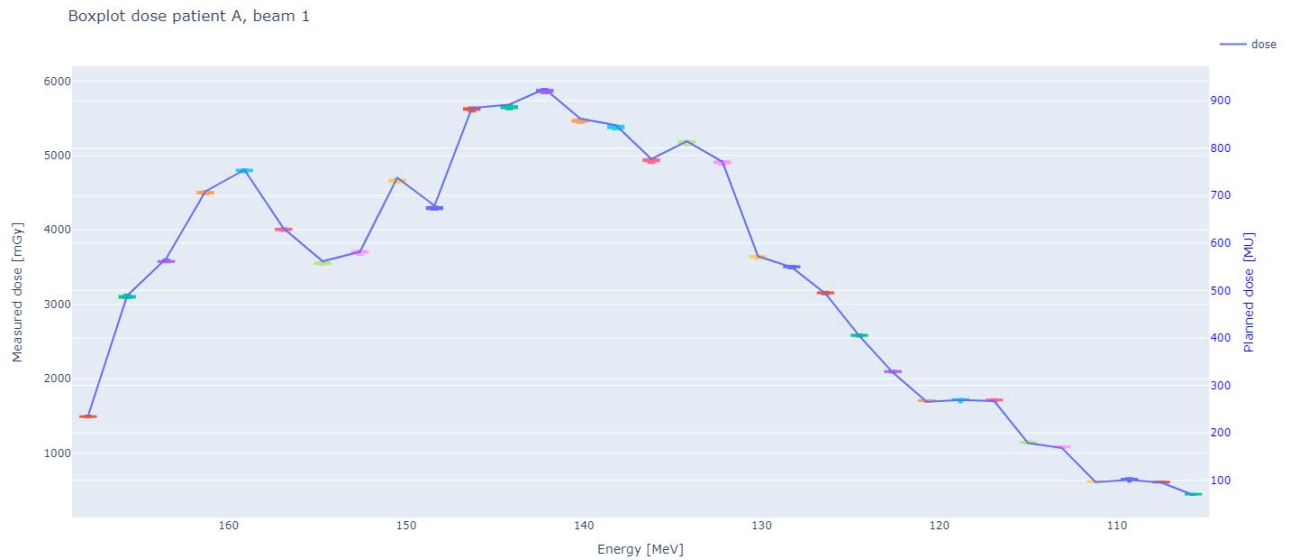
Boxplot dose patient B, beam 1
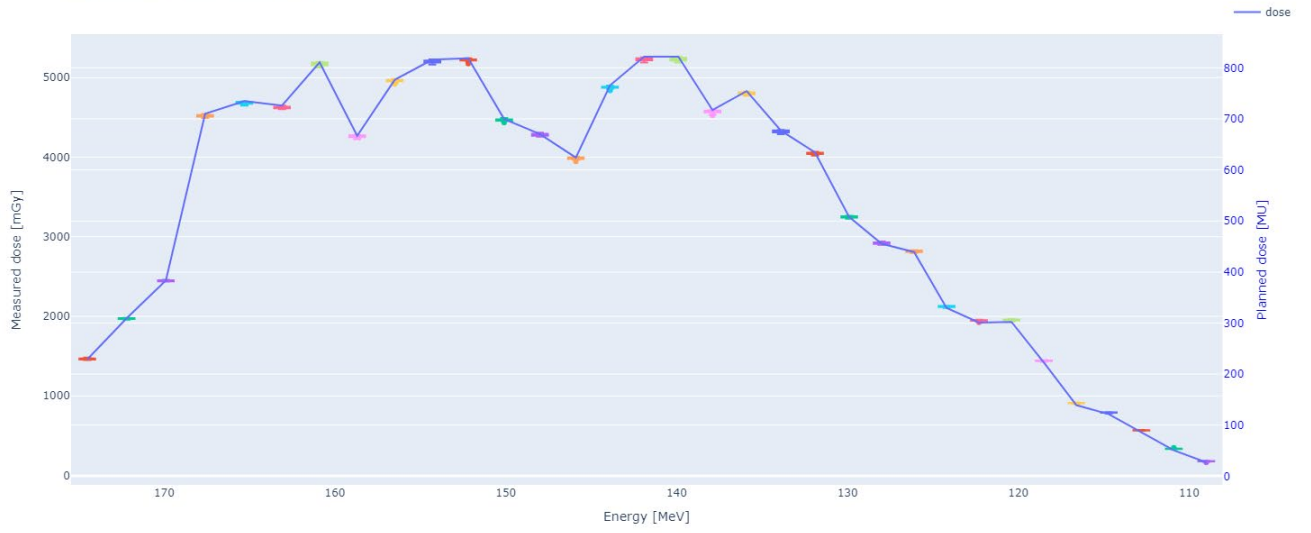
Boxplot dose patient B, beam 2
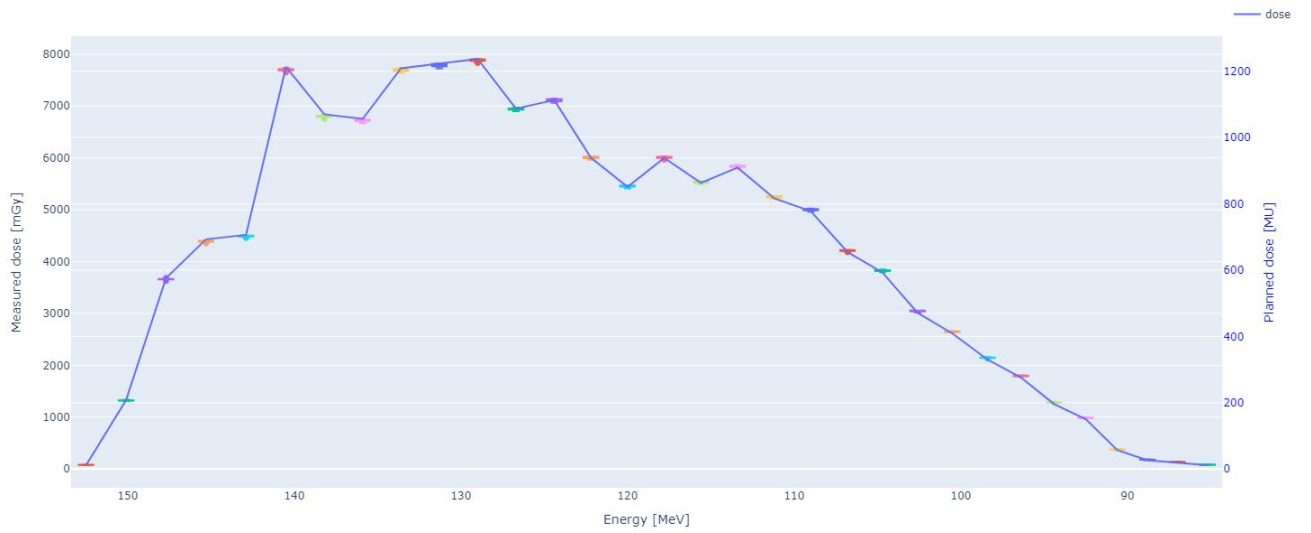
Boxplot dose patient B, beam 3
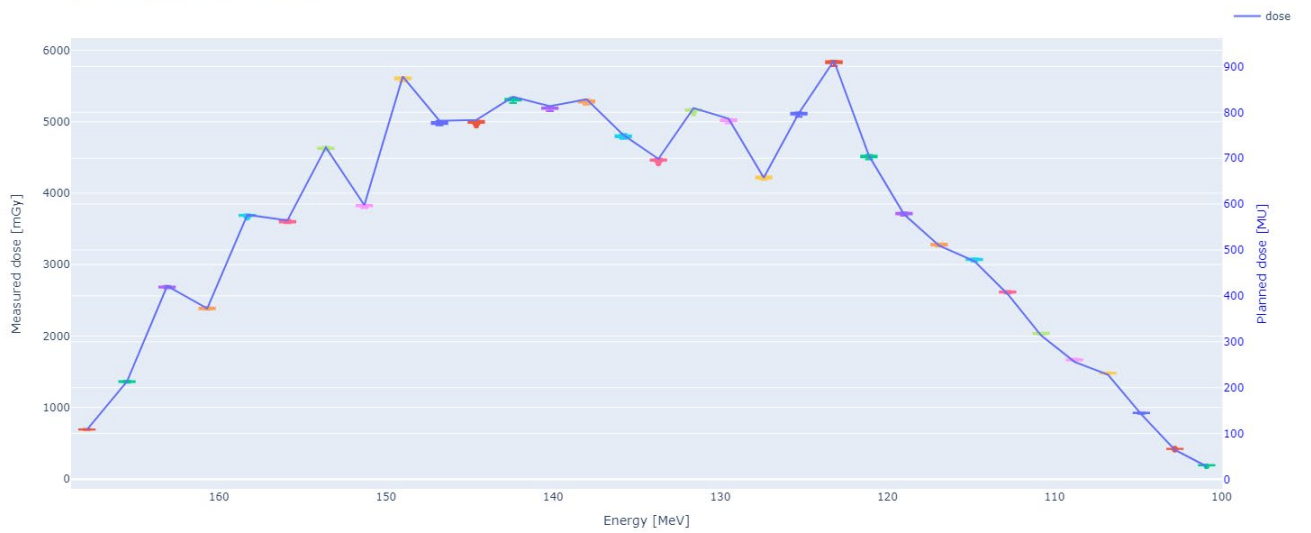
Boxplot dose patient C, beam 1
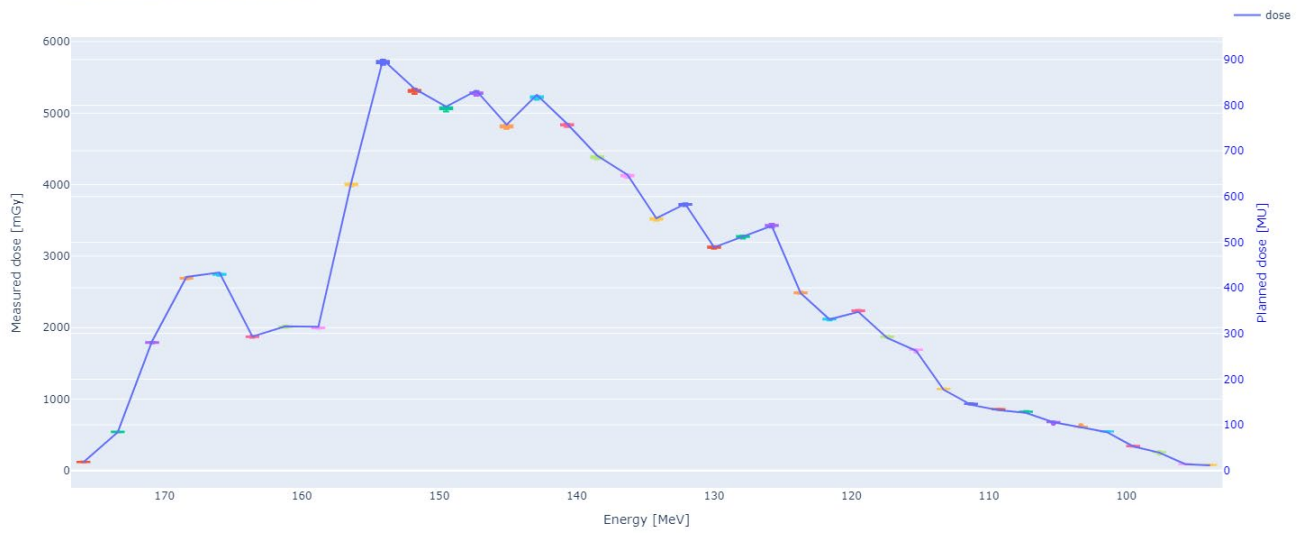
Boxplot dose patient C, beam 2
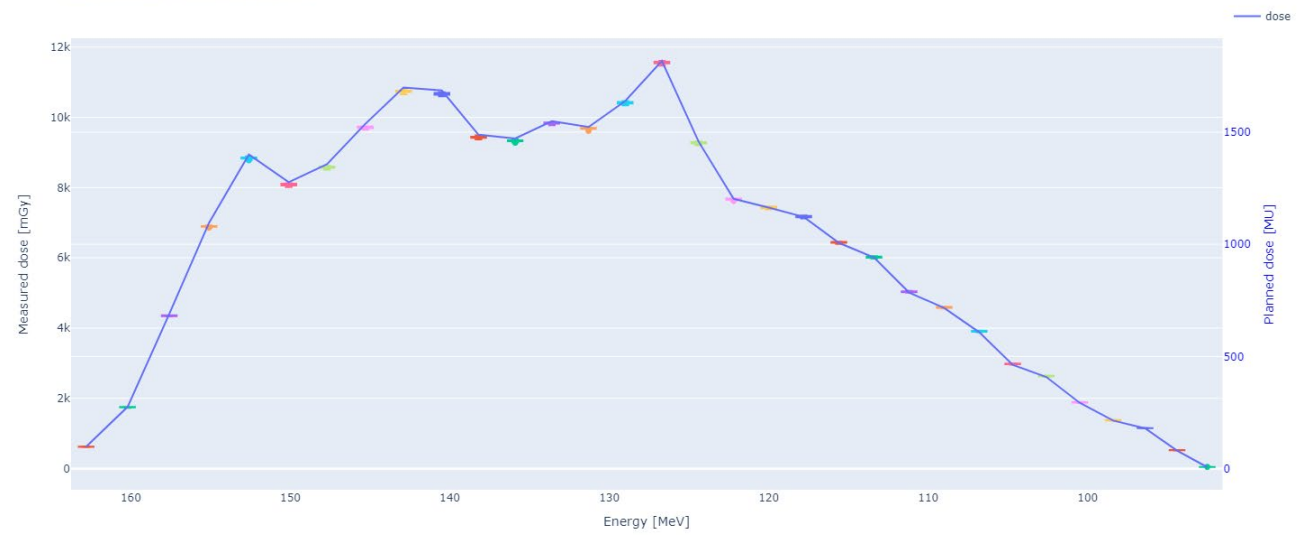
Boxplot dose patient C, beam 3
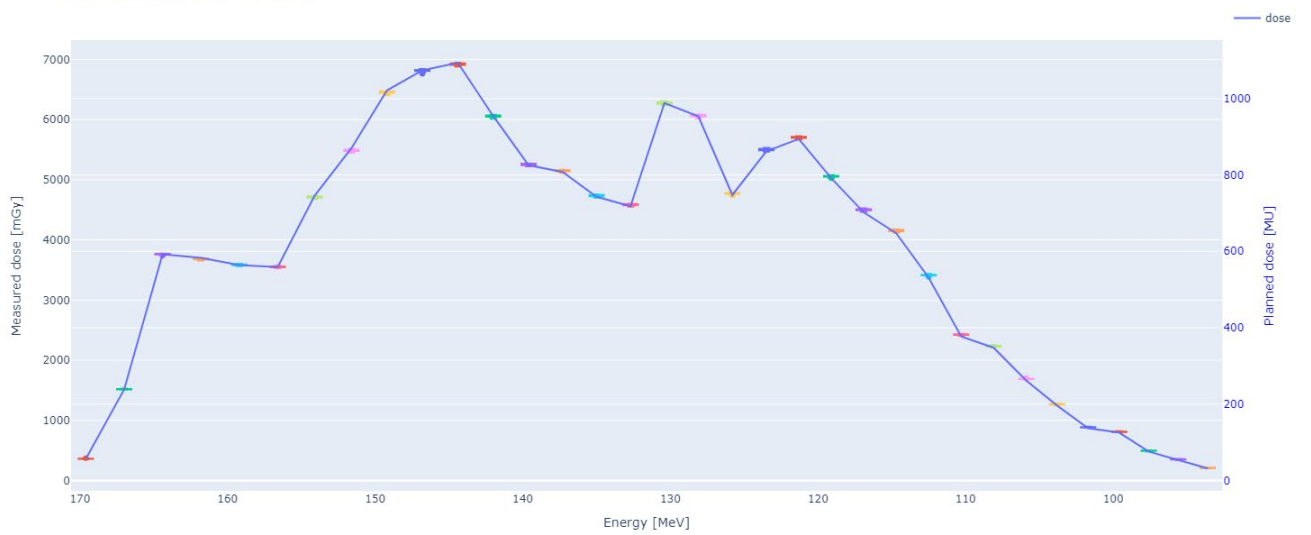
Appendix E ｜ Beam On Time per energy layer for each individual beam

In the plots below the BOT per energy layer for each beam is visualised. The blue line represents the number of planned spots, and the red line represents the planned dose in MU.

Boxplot BOT patient A, beam 1
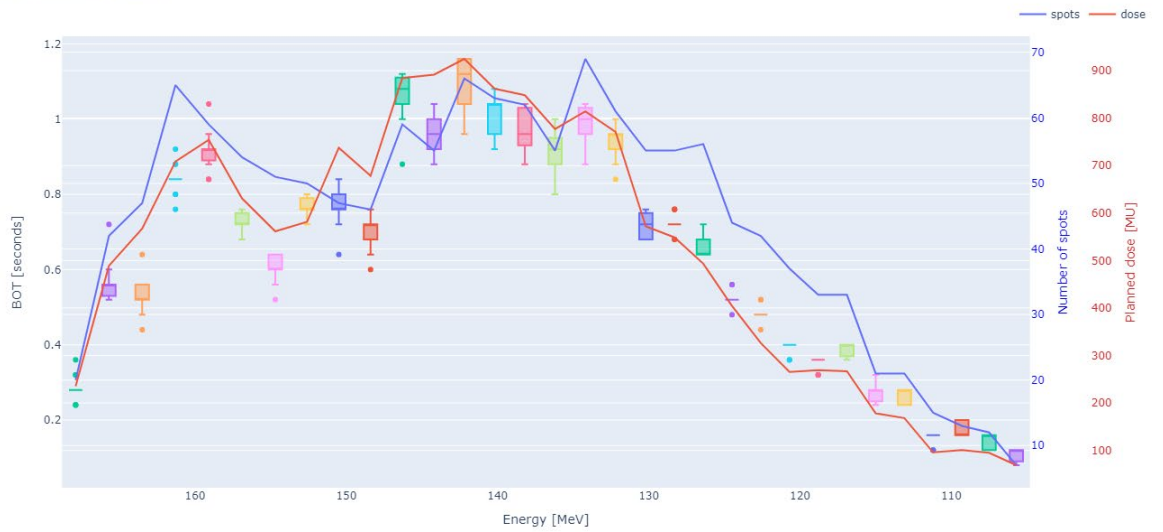
Boxplot BOT patient A, beam 2
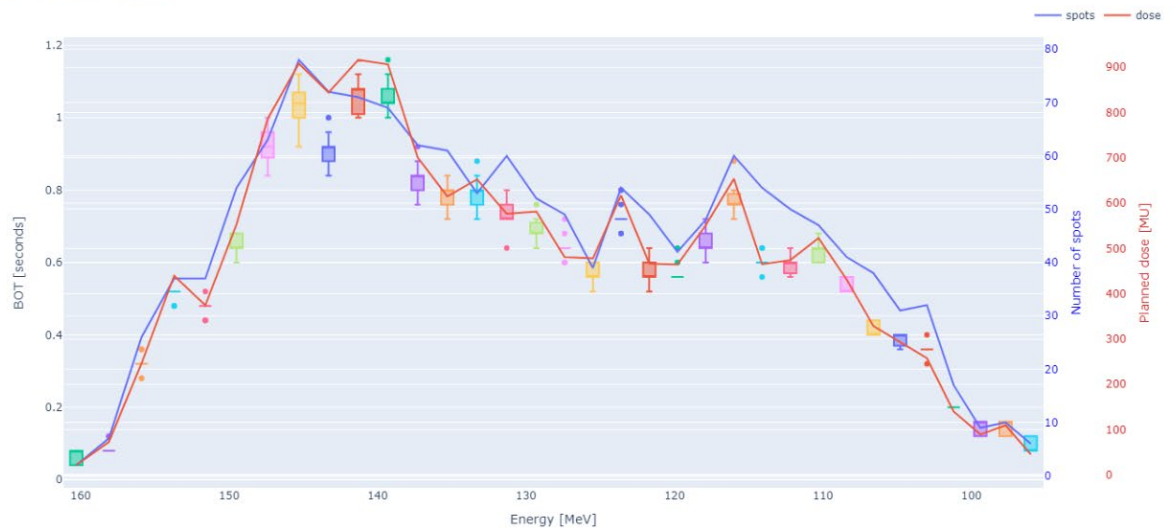
Boxplot BOT patient A, beam 3
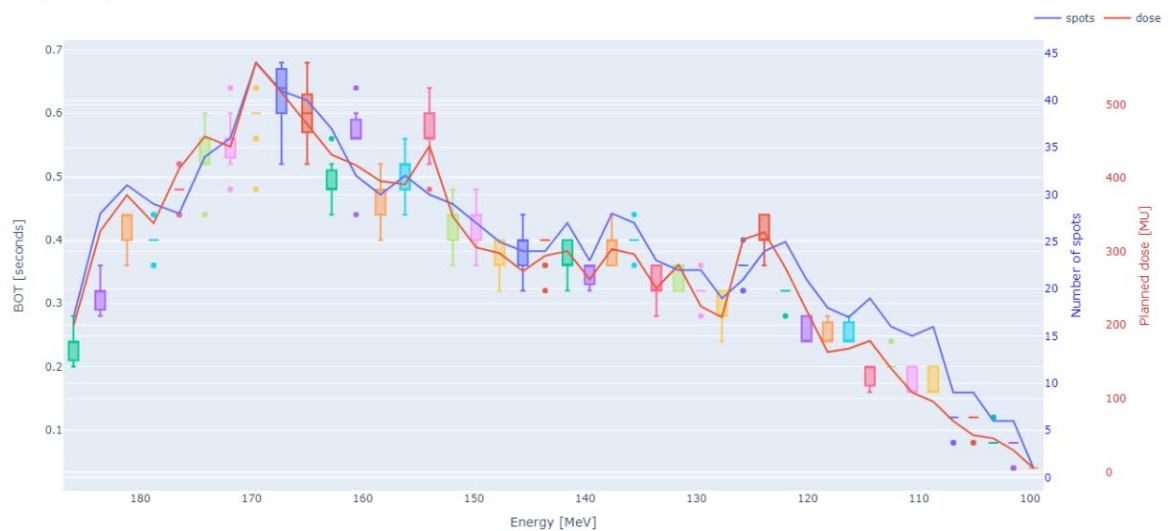
Boxplot BOT patient B, beam 1
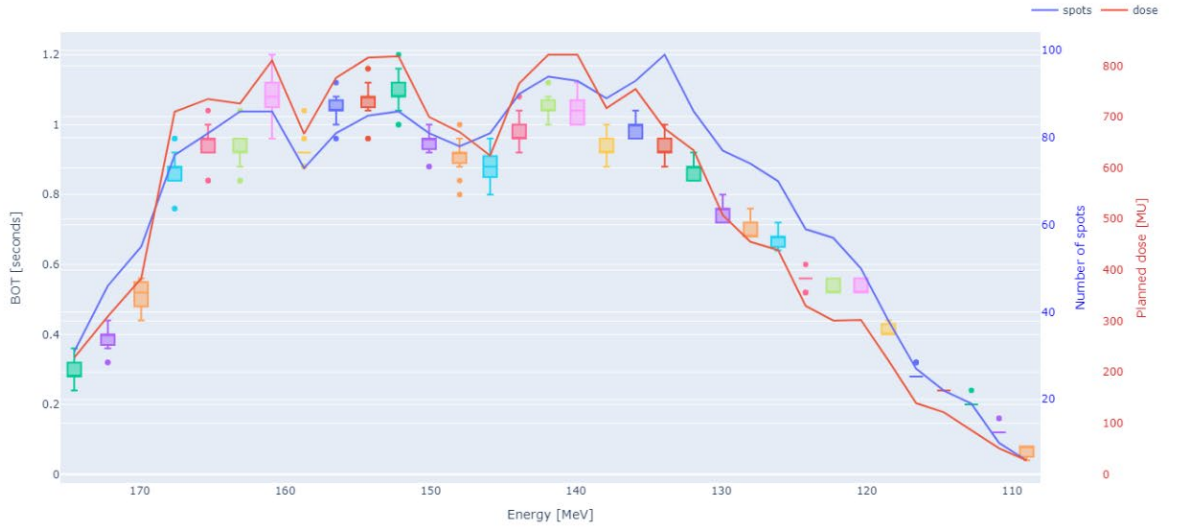
Boxplot BOT patient B, beam 2
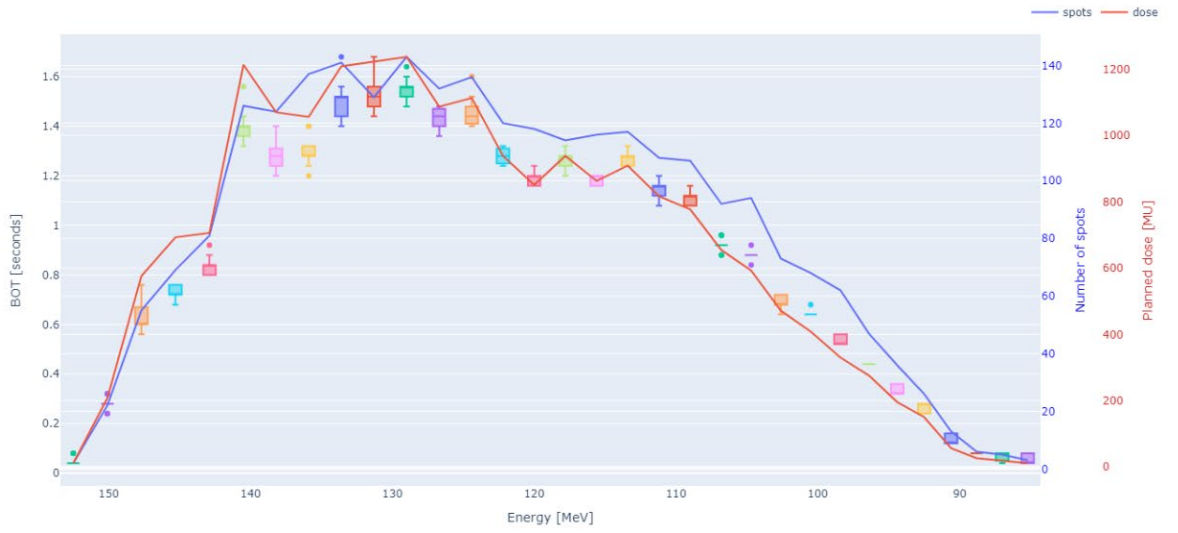
Boxplot BOT patient B, beam 3
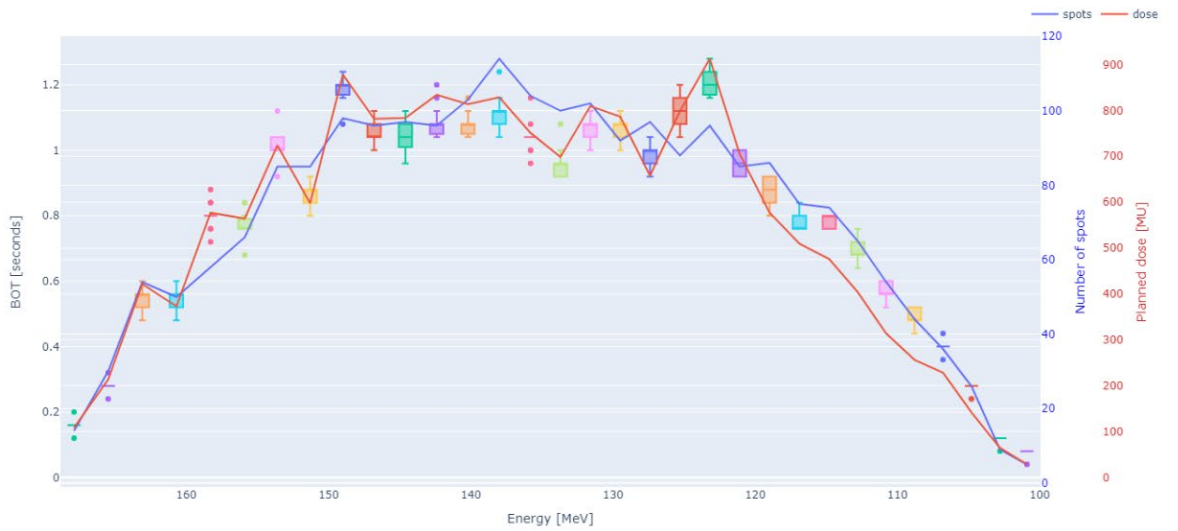
Boxplot BOT patient C, beam 1
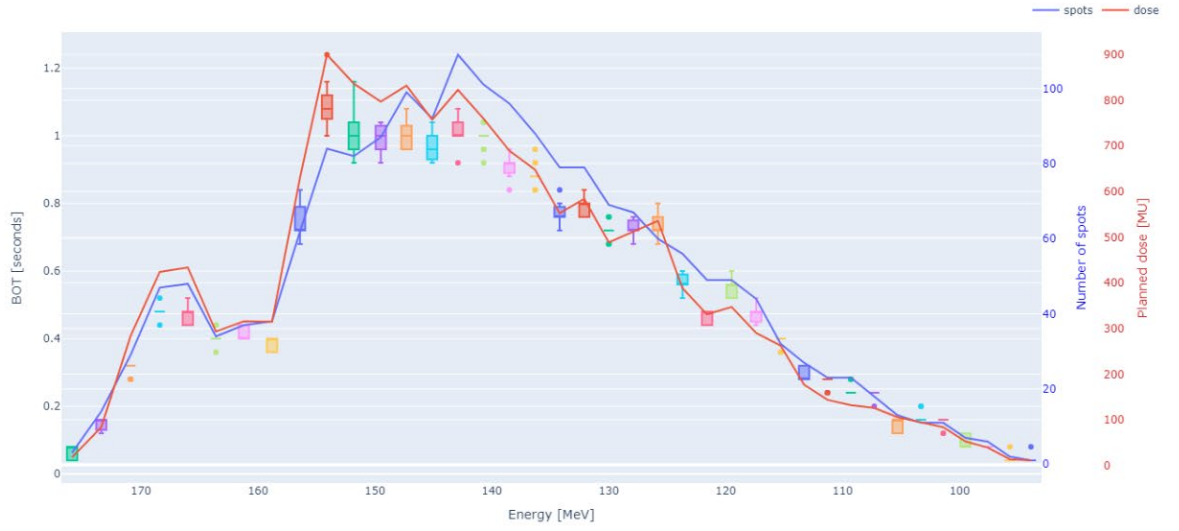
Boxplot BOT patient C, beam 2
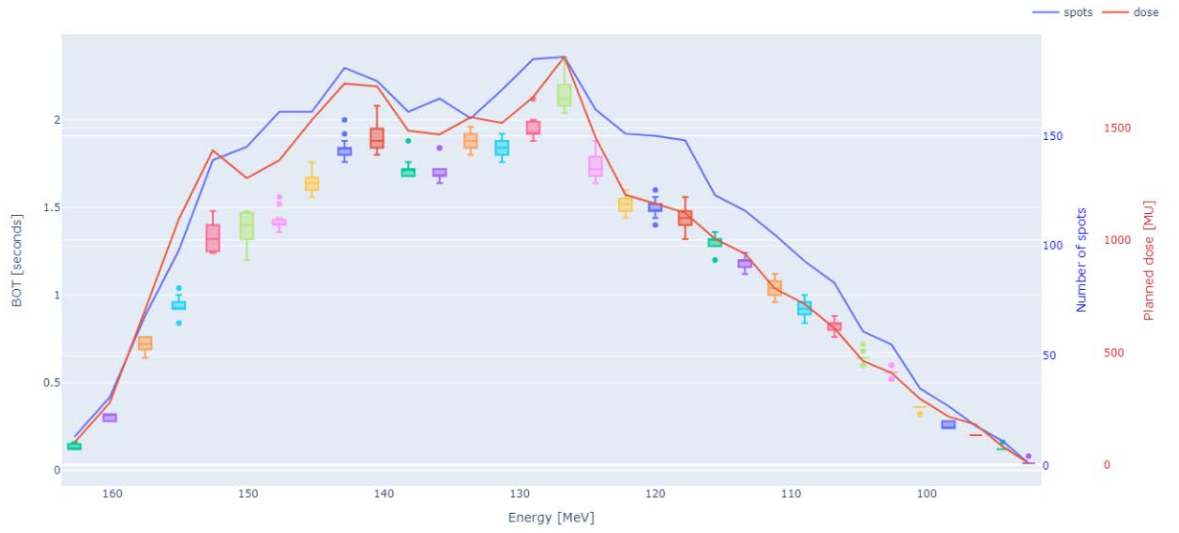
Boxplot BOT patient C, beam 3
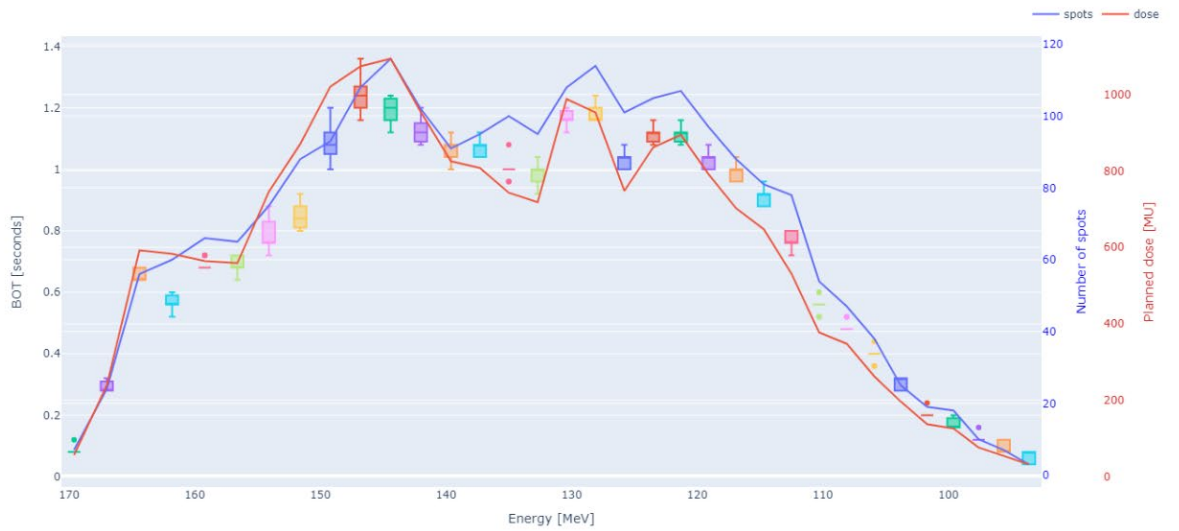
Appendix F | Dose rate per energy layer for each individual beam

By dividing the measured dose with the corresponding BOT, dose rate data is retrieved. In the figures below the dose rate in each energy layer for each beam is visualised. The blue line represents the planned dose in MU.

Boxplot dose rate patient A, beam 1

Boxplot dose rate patient A, beam 2

Boxplot dose rate patient A, beam 3
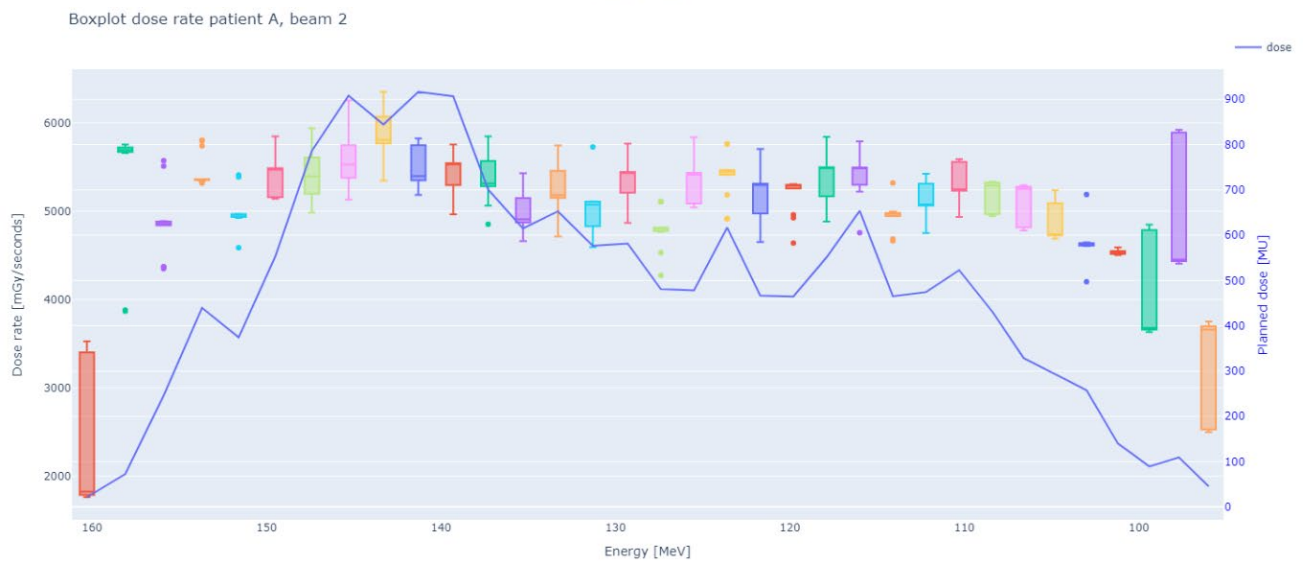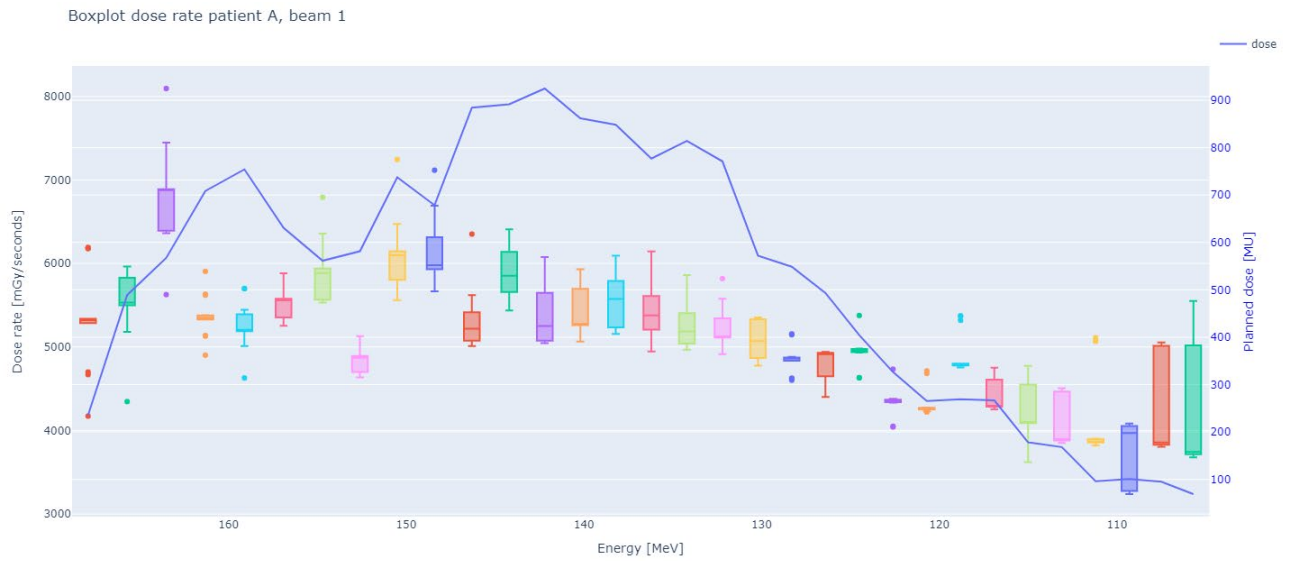
Boxplot dose rate patient B, beam 1
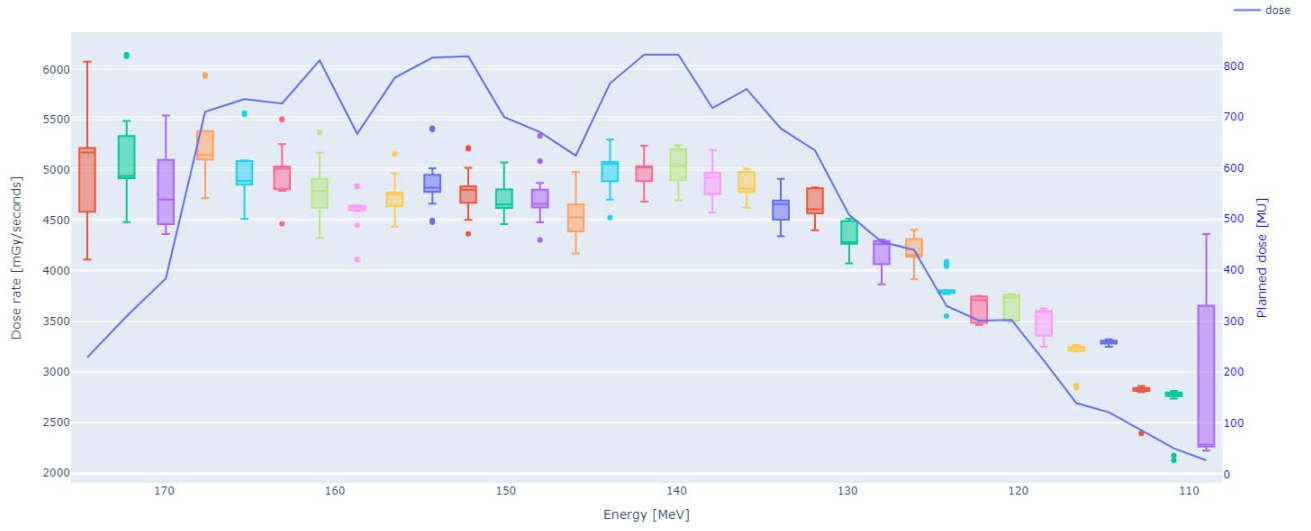
Boxplot dose rate patient B, beam 2
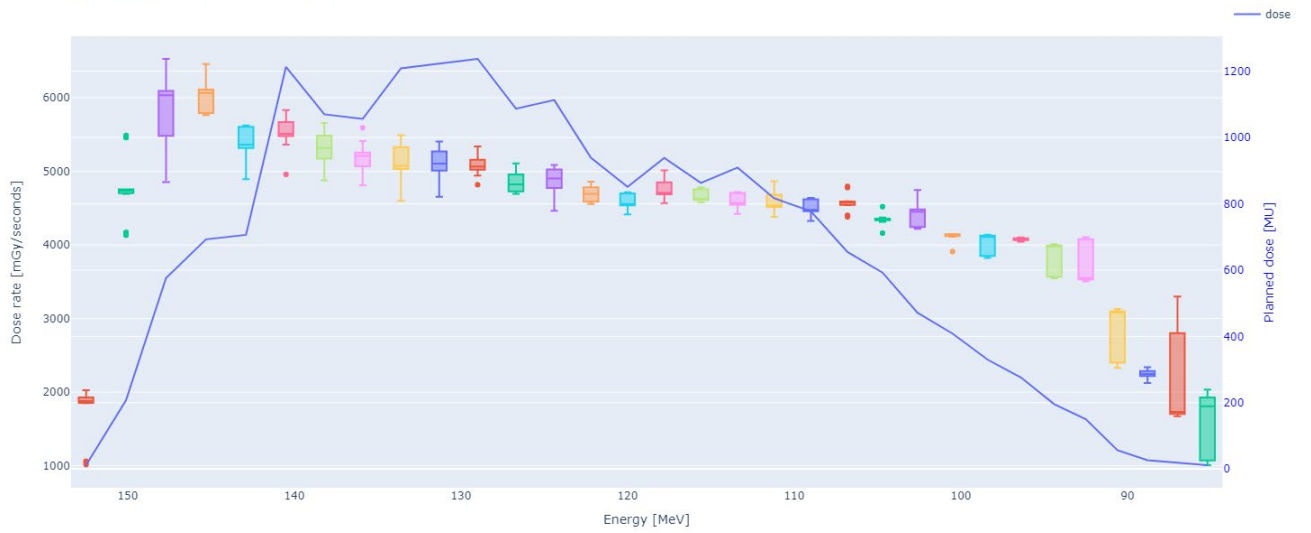
Boxplot dose rate patient B, beam 3
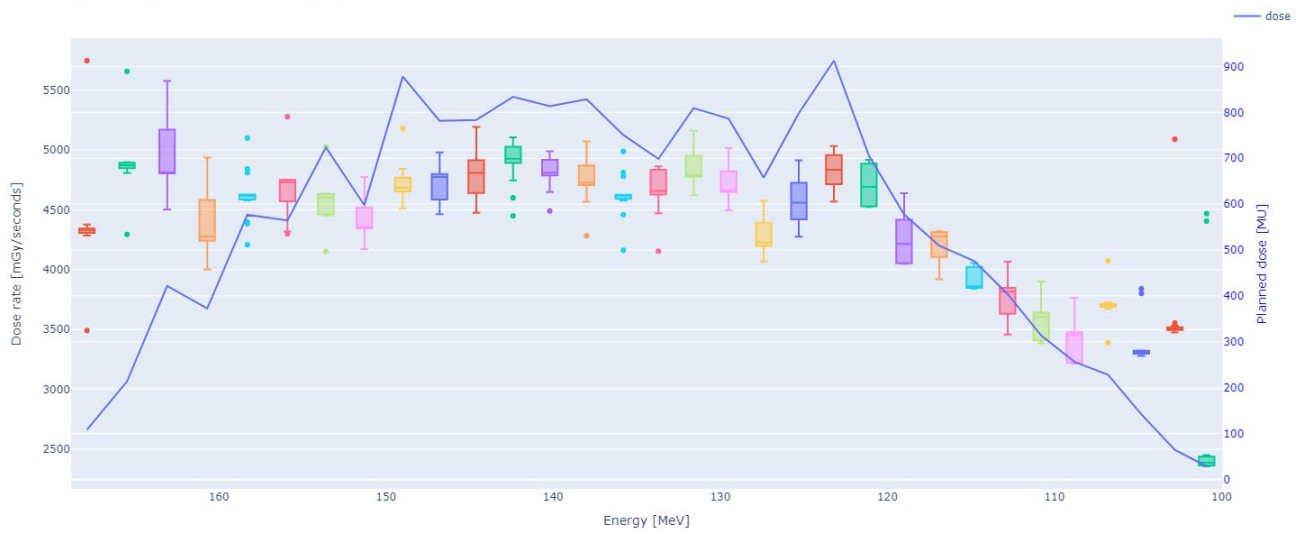
Boxplot dose rate patient C, beam 1
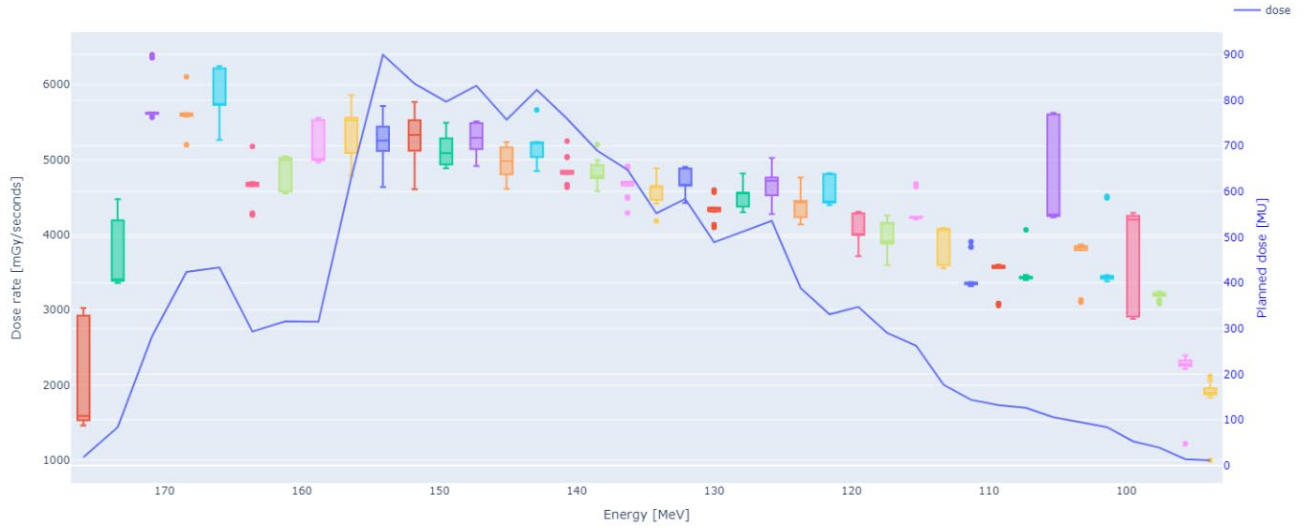
Boxplot dose rate patient C, beam 2
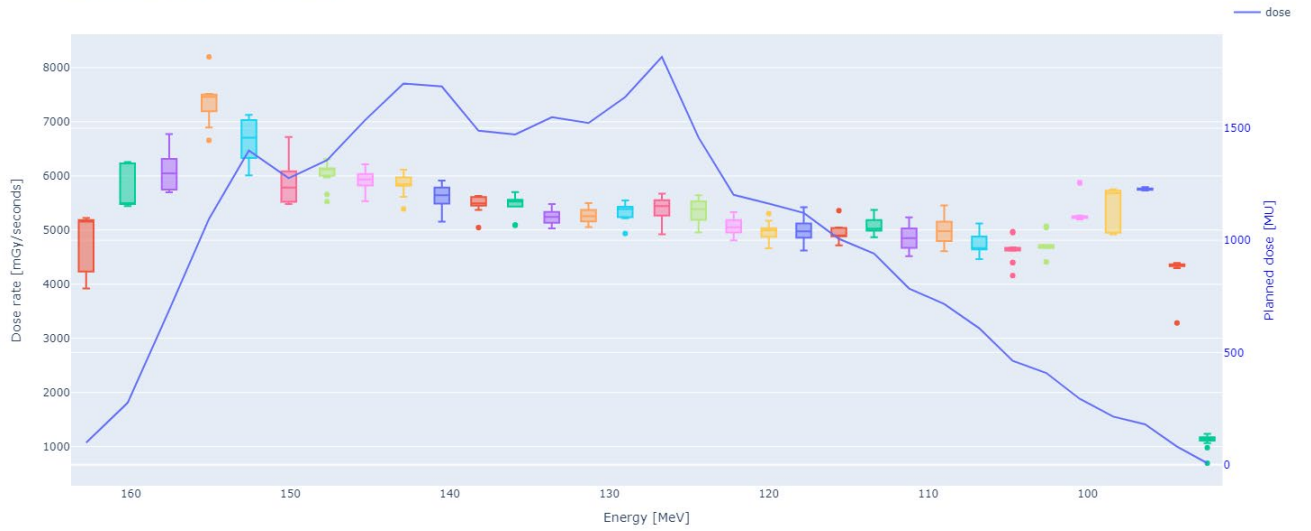
Boxplot dose rate patient C, beam 3
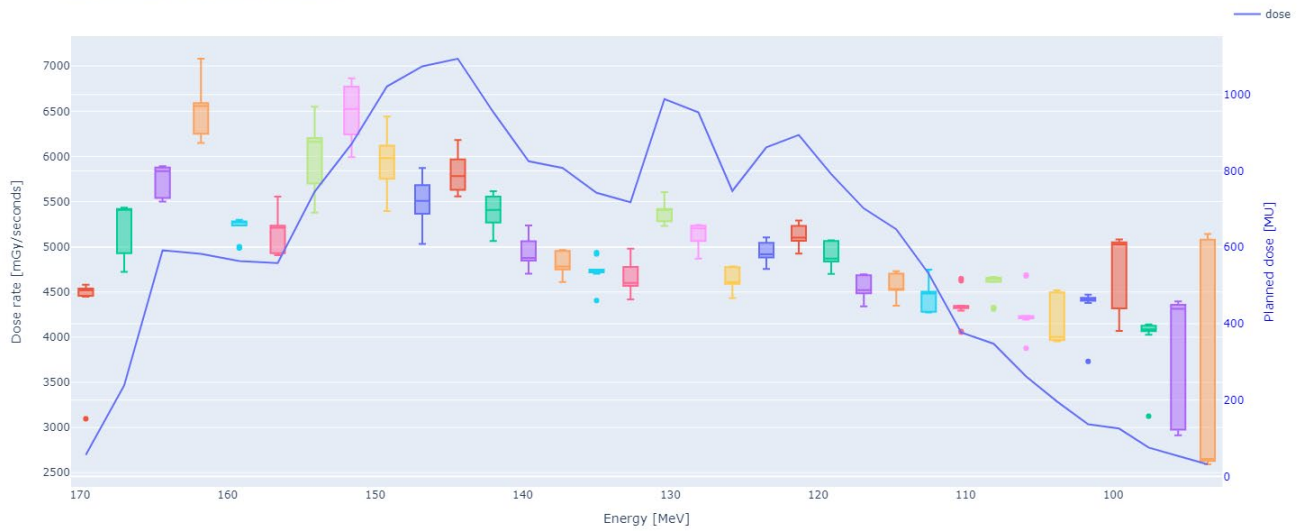
Appendix G │ Script for analysing ELST and BOT

```python
"""
1. Functions for getting the energy layer switching time and beam on time
"""
def get_time_from_dose_maps(mainfolder, patient_name, beam_name,
measurement_number):
    dose_maps = get_dose_maps(mainfolder, patient_name, beam_name,
measurement_number)
    valueA = 0
    valueB = 0
    energy_switch_time = []
    beam_on_time = []
    for data in dose_maps:
        average = np.average(data)
        if average > 0.01:
            valueA += 0.04
            if (valueB >0):
                energy_switch_time.append(round(valueB, 2))
                valueB=0
        else:
            valueB += 0.04
            if (valueA > 0):
                beam_on_time.append(round(valueA, 2))
                valueA=0
    energy_switch_time[0] = None
    return energy_switch_time, beam_on_time


def get_opg_version(headers):
    separator = headers[1].strip()
    if "[Tab]" in separator:
        return "new"
    elif '","' in separator:
        return "old"
    else:
        raise ValueError("Cannot decide the opg version.")


def get_dose_maps(mainfolder, patient_name, beam_name, measurement_number):
    dose_maps = {}
    subfolder = f"{mainfolder}/pat {patient_name} bundel {beam_name} meting
{measurement_number}"
    dose_maps = []

    for filename in os.listdir(subfolder):
        with open(os.path.join(subfolder, filename), 'r') as f:
            contents = f.read()
            soup = BeautifulSoup(contents, features="html.parser")
            headers =  np.genfromtxt(
                StringIO(str(soup.asciiheader)),
                skip_header=1,
                delimiter="\t",
                skip_footer=1,
                dtype=str
            )
            opg_version = get_opg_version(headers)
            delimiter = "," if opg_version == "old" else "\t"
```

```python
            raw_data = np.genfromtxt(
                StringIO(str(soup.asciibody)),
                skip_header=5,
                skip_footer=1,
                delimiter=delimiter
            )

            data = raw_data[:, 1:-1]
            dose_maps.append(data)
    return dose_maps


def get_dose_from_dose_maps(mainfolder, patient_name, beam_name,
measurement_number):
    dose_maps = get_dose_maps(mainfolder, patient_name, beam_name,
measurement_number)
    valueA = 0
    valueB = 0
    dose_beam_off = []
    dose_beam_on = []
    for data in dose_maps:
        total = np.sum([value for value in data.flatten() if value>=0])
        if total > 17.9:
            valueA += total
            if (valueB >0):
                dose_beam_off.append(round(valueB, 2))
                valueB=0
        else:
            valueB += total
            if (valueA > 0):
                dose_beam_on.append(round(valueA, 2))
                valueA=0


    return dose_beam_off, dose_beam_on




"""
2. Definitions for getting RT plan information per beam for each patient.
"""
def get_dose(mainRTplanfolder, patient_name, beam_name):
    dose = {}
    path_plan = f"{mainRTplanfolder}/Plan_{patient_name}.dcm"
    dose = []
    ds = pydicom.dcmread(path_plan)
    for EL in range(0,len(ds.IonBeamSequence[int(f'{beam_name}')-
1].IonControlPointSequence),2):
        spot_weights= ds.IonBeamSequence[int(f'{beam_name}')-
1].IonControlPointSequence[EL].ScanSpotMetersetWeights
        dose.append(np.sum(spot_weights))
    return dose


def get_energy_stepsize(mainRTplanfolder, patient_name, beam_name):
    step_size = {}
    path_plan = f"{mainRTplanfolder}/Plan_{patient_name}.dcm"
    step_size = []
    energy_layer = []
    ds = pydicom.dcmread(path_plan)
    for EL in range(0,len(ds.IonBeamSequence[int(f'{beam_name}')-
1].IonControlPointSequence),2):
```

```python
        energy_layer.append(float(ds.IonBeamSequence[int(f'{beam_name}')-
1].IonControlPointSequence[EL].NominalBeamEnergy))
        step_size = [x-y for x, y in zip(energy_layer, energy_layer [1:])]
    return step_size, energy_layer


def get_spots(mainRTplanfolder, patient_name, beam_name):
    spots = {}
    path_plan = f"{mainRTplanfolder}/Plan_{patient_name}.dcm"
    spots = []
    ds = pydicom.dcmread(path_plan)
    for EL in range(0,len(ds.IonBeamSequence[int(f'{beam_name}')-
1].IonControlPointSequence),2):
        spots.append(int(ds.IonBeamSequence[int(f'{beam_name}')-
1].IonControlPointSequence[EL].NumberOfScanSpotPositions))
    return spots


"""
3. Creating dataframes for ELST and BOT.
"""


if __name__ == "__main__":
    mainfolder = "C:/folder which contains all measurement folders of all
beams"
    mainRTplanfolder = 'C:/folder which contains all RT plans'
        for patient_name in ['A','B' ,'C',    ]:

        for beam_name in ['1','2','3',]:
            step_size, energy_layer = \
                get_energy_stepsize (mainRTplanfolder= mainRTplanfolder,

patient_name=patient_name,

                                                beam_name=beam_name)


            spots = \
                get_spots(mainRTplanfolder= mainRTplanfolder,

patient_name=patient_name,

                                                beam_name=beam_name)


            dose =  \
                get_dose(mainRTplanfolder= mainRTplanfolder,

patient_name=patient_name,

                                                beam_name=beam_name)
            dose_per_spot = [i / j for i, j in zip(dose, spots)]

            df_ELST = pd.DataFrame()
            df_BOT = pd.DataFrame()
            df_dose = pd.DataFrame()
            df_doserate = pd.DataFrame()

            for measurement_number in range(1, 16):

                energy_switch_time, beam_on_time = \
                    get_time_from_dose_maps(mainfolder=mainfolder,
                                    patient_name=patient_name,
                                    beam_name=beam_name,
measurement_number=measurement_number)
```

```python
                dose_beam_off, dose_beam_on = \
                get_dose_from_dose_maps(mainfolder=mainfolder,
                                        patient_name=patient_name,
                                        beam_name=beam_name,
                                        measurement_number=
measurement_number)

                #Making df for each measurement
                df_ELST[f"ELST_{measurement_number}"] = energy_switch_time
                df_BOT[f"BOT_{measurement_number}"] = beam_on_time
                df_dose[f"dose_{measurement_number}"] = dose_beam_on
                df_doserate[f'dose/bot{measurement_number}'] =
df_dose[f'dose_{measurement_number}']
```

Appendix A | Probability Density Functions of period from 4DCT data

In the figures below the 4DCT period values for each patient and each session are visualised in PDF.
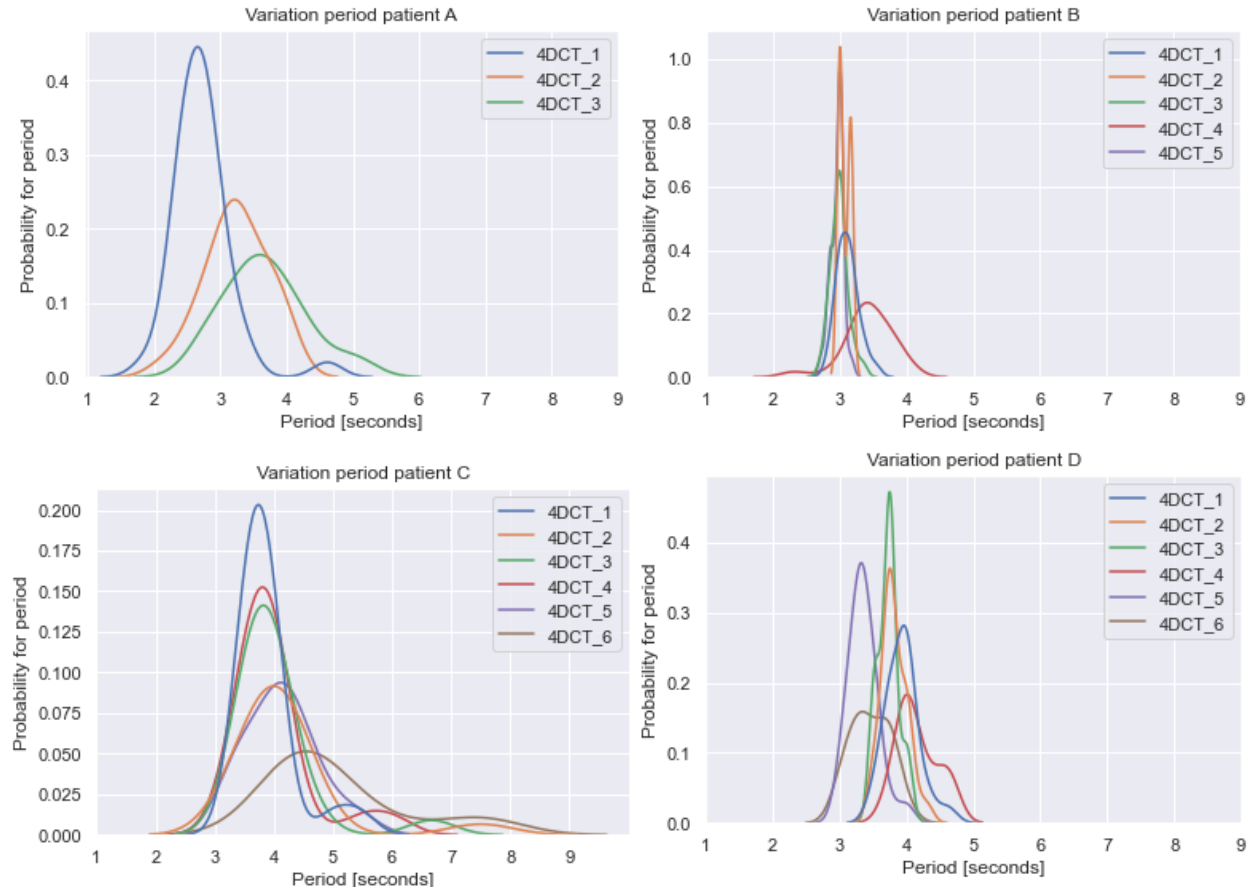
Also, the total variation in period is visualised for each patient.
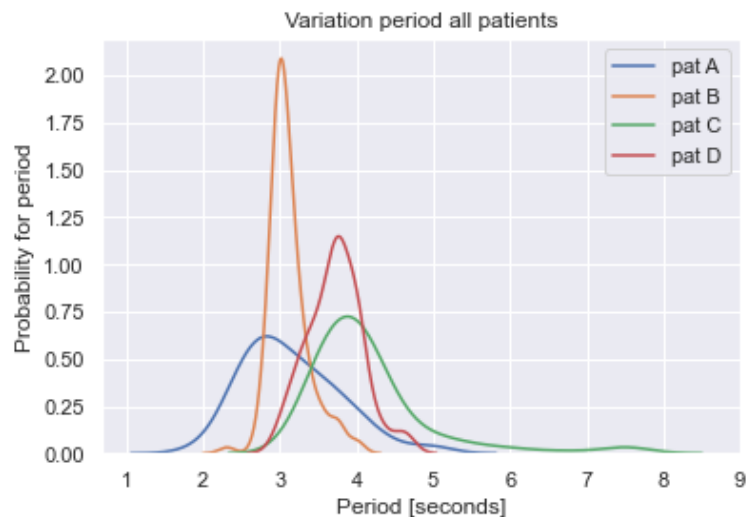
Appendix B | Peak-to-peak amplitudes and periods retrieved from 4DCT in

In the table the peak-to-peak amplitude values from the 4DCTs are shown for each patient. The values are in millimetres.

	Reference	4DCT_2	4DCT_3	4DCT_4	4DCT_5	4DCT_6
Patient A	10.0	9.04	9.19			
Patient B	8.19	10.55	10.87	10.52	8.45	
Patient C	2.52	2.67	2.56	1.74	2.13	2.3
Patient D	9.93	9.26	12.3	11.49	7.81	8.76

Also for each 4DCT, the period for each cycle is visualised in the table below.

Date	Period of cycle																																				
	1	2	3	4	5	6	7	8	9	10	11	12	13	14	15	16	17	18	19	20	21	22	23	24	25	26	27	28	29	30	31	32	33	34	35	36	37
Patient A																																					
19/04	2,4	2,4	2,2	2,9	2,7	2,5	2,7	2,9	2,5	2,4	2,6	2,6	2,9	4,6	2,9	2,5	2,4	2,4	2,3	2,4	2,7	2,7	2,9	2,7	3,0	1,9	3,3	3,3	3,2	2,6	3,0	2,7	2,4	2,7	3,0	2,7	2,7
03/05	2,9	2,1	3,8	3,8	3,2	2,7	3,5	3,0	3,5	2,7	3,8	3,3	3,2	3,0	2,6	3,3	3,8	3,3	2,5	4,0	3,0	3,2	4,0	4,0	3,2	3,2	3,3	3,3									
09/05	3,3	3,5	4,3	3,8	3,5	5,0	4,0	2,9	2,9	3,5	3,5	3,2	3,5	3,8	4,0	5,0	4,3	3,2	3,5	2,7	3,0	3,8	4,0	4,3													
Patient B																																					
04/04	3.5	3.3	3.0	3.2	3.0	3.3	3.3	3.3	3.0	3.2	3.2	3.2	3.0	3.0	3.0	3.0	3.2	3.2	3.2	3.0	3.2	3.0	3.2	2.9	2.9												
22/04	3.0	3.0	3.0	3.2	3.2	3.2	3.2	3.2	3.0	3.2	3.0	3.0	3.2	3.0	3.0	3.0	3.2	3.0	3.0	3.0	3.2	3.0	3.2	3.2	3.0	3.2											
28/04	3.0	3.0	2.9	3.2	3.3	3.0	3.0	3.0	3.0	3.2	3.2	3.0	2.7	2.9	2.9	3.0	3.0	3.0	3.0	2.9	3.0	3.0	2.9	2.9													

06/05	3.3	3.3	3.2	3.5	3.3	3.3	3.3	3.5	3.3	2.3	2.9	3.2	3.2	3.3	3.8	4.0	4.0	3.8	3.8	3.8	3.8	3.5	3.3	3.5
13/05	3.0	2.7	3.0	3.0	3.0	2.9	3.0	3.0	3.0	3.0	2.9	3.0	2.9	3.2	3.0	2.9	3.0	3.0	3.0	3.0	3.0	3.0	2.9	2.9
Patient C																								
28/03	5.5	3.5	3.8	3.5	3.5	3.8	4.0	4.0	3.5	3.5	3.8	4.0	3.8	3.8	3.8	4.0	5.0	3.8	3.5	4.0	4.0	3.3		
07/04	3.5	3.5	4.0	4.3	4.0	3.8	4.3	4.0	4.3	3.5	4.0	3.5	7.5	4.3	4.3	4.0	4.3							
14/04	3.5	4.0	4.6	4.3	6.7	3.5	3.8	3.8	4.0	3.8	4.0	4.0	3.8	3.8	3.5	3.5	3.5	4.0	4.0					
21/04	4.0	3.8	3.5	5.5	3.8	3.8	4.3	4.0	3.8	3.8	3.3	4.0	3.5	4.0	4.0	4.0	3.3	4.0	6.0	3.8	3.5			
28/04	5.0	5.5	3.5	4.0	3.8	4.3	3.3	3.3	4.0	4.3	4.3	4.6	4.6	4.0	4.0	4.3	3.3							
03/05	6.0	7.5	4.3	7.5	5.0	5.0	4.3	4.3	5.0	4.6	4.3	4.3	4.3	4.3										
Patient D																								
23/03	4.0	3.5	3.8	3.8	3.8	4.0	4.0	4.0	4.0	3.8	3.8	4.0	3.5	4.0	4.6	4.3	4.3	4.0	3.8	3.8	4.0	4.0	4.0	

29/03	3.8	4.0	3.8	4.0	4.0	3.8	3.8	3.5	3.8	3.8	4.0	4.0	3.8	3.8	3.8	3.8	4.3	3.8	3.5	3.8	4.0	3.5							
05/04	3.8	3.8	3.8	3.5	3.8	3.8	4.0	3.5	3.8	3.8	4.0	3.8	3.8	4.0	3.8	3.8	3.8	3.5	3.5	3.5	3.8	3.5							
12/04	3.8	4.0	3.8	4.0	4.0	4.3	4.3	4.3	4.6	4.0	4.0	4.0	4.0	4.0	4.6	4.6	4.0	4.6											
21/04	3.3	3.3	3.5	3.8	3.2	3.2	3.0	3.0	3.2	3.5	3.3	3.2	3.3	3.2	3.3	3.3	3.3	3.3	3.5	3.3	3.3	3.3	3.2	3.2	3.5	3.3	3.5	3.5	4.0
28/04	3.3	3.3	3.0	3.2	3.0	3.2	3.3	3.2	3.3	3.5	3.8	3.8	3.8	3.5	3.5	3.8	3.8	3.3	3.8	4.0									

Appendix C | Script for fitting breathing signal into Lujan's model

```python
bestand = "xxx.csv"
measurement = '4DCT_x'


### FROM CSV FILE EXTRACT RELEVANT DATA; THIS DATA IS A LIST
rows = []
with open(bestand) as f:
    reader = csv.reader(f, delimiter=",")
    for row in reader:
        rows.append(row)
    magnification = float(rows[11][1][:-4])
    data= rows[33:]

### MAKE ARRAY OF FLOATS OF THE DATA
y =  np.array([item[1] for item in data])
y = y.astype(np.float)

### LET THE TIME CORRESPONDS WITH Y; SAMPLING TIME ANZAI BELT IS 100 PER
SECOND
sample_rate =0.01 ; start_time = 0; end_time = len(y)/100
t = np.arange(start_time, end_time, sample_rate)
#plt.plot(t, y)
plt.title('breathing signal')
plt.xlabel('Time [seconds]')
plt.ylabel('Position [millimeters]')

### FIND MINIMUM PEAKS
peaks, _ = find_peaks(y*1, width=20, prominence=2,distance=200)
mins, _ = find_peaks(y*-1, width=20, prominence=2,distance=200)
y = y*(a_cc[measurement]/np.mean(y[peaks[1:]]))
plt.plot(t,y)
plt.plot(peaks/100, y[peaks], "o")
plt.plot(mins/100, y[mins], "x")
plt.show()
print (peaks)


### LUJANS MODEL DEFINITION
def fit(t, a, b, n):
    return -a * np.abs(np.cos(np.pi * t / b))**(2*n) + a

avalue = []
pvalue = []
nvalue = []
for i in np.arange(1,len(mins),1):

    t1= t[mins[i-1]:mins[i]]
    y1= y[mins[i-1]:mins[i]]
    params, pcov = scipy.optimize.curve_fit(
        fit, t1, y1, bounds=(0, 14), p0=(12, 4, 2))
    plt.figure(i+1)
    plt.title('breathing cycle ' + str(i-1) + ' of ' + str(len(mins)-2))
    plt.xlabel('Time [seconds]')
    plt.ylabel('Position [millimeters]')
    plt.plot(t1, fit(t1, a=params[0], b=params[1], n=params[2]), '--');
```

```
plt.plot(t1, y1)
avalue.append(params[0])
pvalue.append(params[1])
nvalue.append(params[2])
```

Appendix A | Subject information sheet and informed consent form

Versienummer: 3 (29/03/2022)

Proefpersoneninformatie voor deelname aan medisch-wetenschappelijk onderzoek
[Variaties in ademhalingspatroon/ VAR-LUNG-PT]
Officiële titel: Invloed van variaties in ademhalingspatroon op de protonbehandelplannen, hoe robuust zijn de plannen?

Geachte heer/ mevrouw,

Met deze informatiebrief willen we u vragen of u wilt meedoen aan medisch-wetenschappelijk onderzoek. U krijgt deze brief omdat u protonentherapie zal krijgen binnen HollandPTC en wij onderzoek doen om deze behandeling te verbeteren.

U leest hier om wat voor onderzoek het gaat, wat het voor u betekent, en wat de voordelen en nadelen zijn. Wilt u deze informatie goed doorlezen en beslissen of u wilt meedoen? U bent overigens nooit verplicht om aan een onderzoek mee te doen. Meedoen is geheel vrijwillig. Als u besluit om niet mee te doen, dan hoeft u hiervoor geen reden op te geven. Welke beslissing u ook neemt, het heeft geen gevolgen voor uw behandeling.

Indien u wilt meewerken aan dit onderzoek, zullen wij dat enorm waarderen. U kunt hiervoor aan het einde van deze brief uw toestemming geven door het toestemmingsformulier te ondertekenen. Nadat u schriftelijk toestemming heeft gegeven, kunt u zich op elk moment uit het onderzoek terugtrekken. Hiervoor hoeft u geen reden op te geven.

Informatie over het onderzoek
In dit onderzoek bekijken we of het nodig is om de huidige behandelplannen te personaliseren op uw ademhaling. Op dit moment maken we de behandelplannen met behulp van het ademhalingspatroon dat u bij de eerste scans had. Wij willen gaan kijken of het een meerwaarde heeft om eventuele verschillen in uw ademhaling mee te nemen in het opstellen van het behandelplan.

Het onderzoek gebeurt als volgt: U komt naar HollandPTC voor uw behandeling met protonentherapie. In uw behandeltraject krijgt u standaard meerdere scans, waaronder een wekelijkse CT scan. Tijdens deze CT scan, zal er een band rond uw buik worden geplaatst, deze band houdt uw ademhalingssignaal in de gaten tijdens de scan. De totale scan zal ongeveer 10 minuten duren en is onderdeel van uw standaard behandeling. Voor het onderzoek vragen we van u of u na deze scan nog een paar minuten langer op de CT tafel wilt blijven liggen zodat wij uw ademhalingssignaal één minuut lang kunnen meten. Deze extra meting zal na elke wekelijkse CT herhaalt worden. In totaal wordt deze extra meting 3 of 4 keer uitgevoerd.

Meedoen aan het onderzoek zal geen invloed hebben op uw behandelplan bij HollandPTC. Het levert u geen risico's en ook geen voordelen op. Wij zullen alleen uw ademhaling voor 1 minuut meten. U zal hiervoor geen financiële vergoeding ontvangen.

Versienummer: 3 (29/03/2022)

Als u toestemming geeft voor het meten van uw ademhalingssignaal met de band, zullen we uw gegevens gebruiken voor onderzoek binnen HollandPTC. De data voor dit onderzoek zullen in HollandPTC opgeslagen worden en zullen HollandPTC niet verlaten. We gebruiken de volgende gegevens van u:

- uw HollandPTC patiëntennummer
- (medische) gegevens die we tijdens het onderzoek verzamelen, dit zijn uw behandelplan en de 3-4 ademhalingsmetingen.

Om uw privacy te beschermen geven we uw gegevens een code. Als we uw gegevens gebruiken voor dit onderzoek gebruiken we ook steeds deze code. Ook in rapporten en publicaties over het onderzoek kan niemand terughalen dat het over u ging. De data die gebruikt worden voor het onderzoek zullen verwijderd worden wanneer de bewaartermijn van 15 jaar is verstreken. Sommige mensen kunnen wel uw gegevens zonder code inzien, dit is om te controleren dat het onderzoek goed wordt uitgevoerd. Zij houden uw gegevens geheim.

Vragen en/ of klachten

Voor vragen rondom de privacy, gebruik van persoonsgegevens of uw privacy rechten, kunt u terecht bij de Functionaris Gegevensbescherming HollandPTC (e-mailadres: privacy@hollandptc.nl).

Bij klachten kunt u zich melden bij de klachtencommissie van het HollandPTC. Hier kunt u melding maken van uw onvrede en het klachtenformulier invullen. Zij informeren u zo snel mogelijk over een mogelijke oplossing en kan eventueel de klachtenfunctionaris inschakelen (e-mailadres: klachtenfunctionaris@hollandptc.nl).

Als u naar aanleiding van deze brief nog vragen heeft kunt u deze altijd stellen bij uw arts. Ook is het mogelijk om vragen te stellen aan de onderzoeker die het onderzoek gaat uitvoeren. Dit is Jasika Paramasamy. Zij zal u ook vooraf aan de eerste CT scan spreken, zodat u de mogelijkheid heeft om vragen te stellen.

Met vriendelijke groet,
Jasika Paramasamy

Versienummer: 3 (29/03/2022)

Toestemmingsformulier proefpersoon
Behorende bij
[**Variaties in ademhalingspatroon**]

- – Ik heb de informatiebrief gelezen. Ook kon ik vragen stellen. Mijn vragen zijn goed genoeg beantwoord. Ik had genoeg tijd om te beslissen of ik meedoe.
- – Ik weet dat meedoen vrijwillig is. Ook weet ik dat ik op ieder moment kan beslissen om toch niet mee te doen met het onderzoek. Of om ermee te stoppen. Ik hoef dan niet te zeggen waarom ik wil stoppen.
- – Ik geef de onderzoekers toestemming om mijn gegevens te verzamelen en gebruiken. De onderzoekers doen dit alleen om de onderzoeksvraag van dit onderzoek te beantwoorden.
- – Ik weet dat voor de controle van het onderzoek sommige mensen al mijn gegevens kunnen inzien. Die mensen staan in deze informatiebrief.
- – Ik wil meedoen aan dit onderzoek.

Mijn naam is (proefpersoon): ………………………………..
Handtekening: ………………………   Datum : __ / __ / __

Ik verklaar dat ik deze proefpersoon volledig heb geïnformeerd over het genoemde onderzoek.

Wordt er tijdens het onderzoek informatie bekend die die de toestemming van de proefpersoon kan beïnvloeden? Dan laat ik dit op tijd weten aan deze proefpersoon.

Naam onderzoeker (of diens vertegenwoordiger):……………………………….
Handtekening:………………………   Datum: __ / __ / __

De proefpersoon krijgt een volledige informatiebrief mee, samen met een getekende versie van het toestemmingsformulier.

[12] Sung, H., Ferlay, J., Siegel, R. L., Laversanne, M., Soerjomataram, I., Jemal, A., & Bray, F. (2021). Global Cancer Statistics 2020: GLOBOCAN Estimates of Incidence and Mortality Worldwide for 36 Cancers in 185 Countries. CA: a cancer journal for clinicians, 71(3), 209–249. https://doi.org/10.3322/caac.21660

[3] Cancer. Dectection, diagnosis and staging. 2022. Retrieved from: https://www.cancer.org/cancer/lung-cancer/detection-diagnosis-staging/detection.html

[4] Ellis, Peter M, and Rachel Vandermeer. "Delays in the diagnosis of lung cancer." Journal of thoracic disease vol. 3,3 (2011): 183-8. doi:10.3978/j.issn.2072-1439.2011.01.01

[5] Cancer. Non-small cell lung treatment. 2022. Retrieved from: https://www.cancer.gov/types/lung/hp/non-small-cell-lung-treatment-pdq#:~:text=NSCLC%20is%20any%20type%20of,occur%20in%20unusual%20histologic%20VARIANts.

[6] Myers DJ, Wallen JM. Lung Adenocarcinoma. 2021 Sep 10. In: StatPearls [Internet]. Treasure Island (FL): StatPearls Publishing; 2022 Jan–. PMID: 30137862.

[7] Sabbula BR, Anjum F. Squamous Cell Lung Cancer. [Updated 2021 Dec 8]. In: StatPearls [Internet]. Treasure Island (FL): StatPearls Publishing; 2022 Jan-. Available from: https://www.ncbi.nlm.nih.gov/books/NBK564510/

[8] Bernhardt EB, Jalal SI. Small Cell Lung Cancer. Cancer Treat Res. 2016;170:301-22. doi: 10.1007/978-3-319-40389-2_14. PMID: 27535400.

[9] NHS. Lung cancer diagnosis. 2021. Retrieved from: https://www.nhs.uk/conditions/lung-cancer/diagnosis/#:~:text=Most%20lung%20tumours%20appear%20on,that%20forms%20in%20the%20lungs).

[10] Xiao, J., Zhang, H., Gong, Y., Fu, Y., Tang, B., Wang, S., Jiang, Q., & Li, P. (2010). Feasibility of using intravenous contrast-enhanced computed tomography (CT) scans in lung cancer treatment planning. Radiotherapy and oncology : journal of the European Society for Therapeutic Radiology and Oncology, 96(1), 73–77. https://doi.org/10.1016/j.radonc.2010.02.029

[11] https://www.chestmed.theclinics.com/article/S0272-5231(03)00065-0/fulltext

[12] Travis WD, Brambila E, Burke AP, et al. WHO classification of tumours of the lung, pleura, thymus and heart. 4th edition. Lyon (France): IARC Press; 2015.

[13] Deppen SA, Blume JD, Kensinger CD, et al. Accuracy of FDG-PET to Diagnose Lung Cancer in Areas With Infectious Lung Disease: A Meta-analysis. JAMA. 2014;312(12):1227–1236. doi:10.1001/jama.2014.11488

[14] Chen K. N. (2016). Zhongguo fei ai za zhi = Chinese journal of lung cancer, 19(6), 409–412. https://doi.org/10.3779/j.issn.1009-3419.2016.06.22

[15] Lemjabbar-Alaoui, H., Hassan, O. U., Yang, Y. W., & Buchanan, P. (2015). Lung cancer: Biology and treatment options. Biochimica et biophysica acta, 1856(2), 189–210. https://doi.org/10.1016/j.bbcan.2015.08.002

[16] Hirsch, F. R., Scagliotti, G. V., Mulshine, J. L., Kwon, R., Curran, W. J., Jr, Wu, Y. L., & Paz-Ares, L. (2017). Lung cancer: current therapies and new targeted treatments. Lancet (London, England), 389(10066), 299–311. https://doi.org/10.1016/S0140-6736(16)30958-8

[17] https://www.ccnursing.theclinics.com/article/S0899-5885(19)30029-2/fulltext

[18] Han, M., Ruan, J., & Zhi, X. (2002). Zhongguo fei ai za zhi = Chinese journal of lung cancer, 5(4), 287–289. https://doi.org/10.3779/j.issn.1009-3419.2002.04.14

[19] Hofman, V., Ilie, M., Long, E., Guibert, N., Selva, E., Washetine, K., Mograbi, B., Mouroux, J., Vénissac, N., Reverso-Meinietti, J., Milano, G., Mazières, J., Marquette, C. H., Paterlini-Bréchot, P., & Hofman, P. (2014). Detection of circulating tumour cells from lung cancer patients in the era of targeted therapy: promises, drawbacks and pitfalls. Current molecular medicine, 14(4), 440–456. https://doi.org/10.2174/1566524014666140414205455

[20] Ihde D. C. (1992). Chemotherapy of lung cancer. The New England journal of medicine, 327(20), 1434–1441. https://doi.org/10.1056/NEJM199211123272006

[21] Anagnostou, V. K., & Brahmer, J. R. (2015). Cancer immunotherapy: a future paradigm shift in the treatment of non-small cell lung cancer. Clinical cancer research : an official journal of the American Association for Cancer Research, 21(5), 976–984. https://doi.org/10.1158/1078-0432.CCR-14-1187

[22] Alizadeh, E., Orlando, T. M., & Sanche, L. (2015). Biomolecular damage induced by ionizing radiation: the direct and indirect effects of low-energy electrons on DNA. Annual review of physical chemistry, 66, 379–398. https://doi.org/10.1146/annurev-physchem-040513-103605

[23] Joanna Czapla-Masztafiak, Jakub Szlachetko, Christopher J. Milne, Ewelina Lipiec, Jacinto Sá, Thomas J. Penfold, Thomas Huthwelker, Camelia Borca, Rafael Abela, Wojciech M. Kwiatek, Investigating DNA Radiation Damage Using X-Ray Absorption Spectroscopy, Biophysical Journal, Volume 110, Issue 6, 2016, Pages 1304-1311, ISSN 0006-3495, https://doi.org/10.1016/j.bpj.2016.01.031.

[24] Vitti, E. T., & Parsons, J. L. (2019). The Radiobiological Effects of Proton Beam Therapy: Impact on DNA Damage and Repair. Cancers, 11(7), 946. https://doi.org/10.3390/cancers11070946

[25] Baumann, B. C., Mitra, N., Harton, J. G., Xiao, Y., Wojcieszynski, A. P., Gabriel, P. E., Zhong, H., Geng, H., Doucette, A., Wei, J., O'Dwyer, P. J., Bekelman, J. E., & Metz, J. M. (2020). Comparative Effectiveness of Proton vs Photon Therapy as Part of Concurrent Chemoradiotherapy for Locally Advanced Cancer. JAMA oncology, 6(2), 237–246. https://doi.org/10.1001/jamaoncol.2019.4889

[26] LaRiviere, M. J., Santos, P., Hill-Kayser, C. E., & Metz, J. M. (2019). Proton Therapy. Hematology/oncology clinics of North America, 33(6), 989–1009. https://doi.org/10.1016/j.hoc.2019.08.006

[27] Zeng, XH., Zheng, JX., Song, YT. *et al.* Beam optics study for energy selection system of SC200 superconducting proton cyclotron. *NUCL SCI TECH* **29,** 134 (2018). https://doi.org/10.1007/s41365-018-0462-5

[28] R. Sépulchre, B. Marchand, D. Prieels, B. Bauvir, M. Gérard, "Dynamic Delivery Planning in IBA Proton Pencil Beam", EPAC'2000, Vienna, June 2000

[29] Thariat, J., Habrand, J. L., Lesueur, P., Chaikh, A., Kammerer, E., Lecomte, D., Batalla, A., Balosso, J., & Tessonnier, T. (2018). Apports de la protonthérapie à la radiothérapie d'aujourd'hui, pourquoi, comment ? [Why proton therapy? And how?]. Bulletin du cancer, 105(3), 315–326. https://doi.org/10.1016/j.bulcan.2017.12.004

[30] Virtuelle Experimente. Modell of a Cyclotron (non relativistic). 2022. Retrieved from: https://virtuelle-experimente.de/en/b-feld/anwendung/zyklotron.php

[31] Britannica. Cyclotron Dee. 2022. Retrieved from: https://www.britannica.com/science/dee

[32] F. Stichelbaut, L. Herremans, G. Bosmans, P. Pleunis, C. Gomà. (2018). Proton therapy technology in the clinic. Retrieved from: https://www.icrp.org/docs/icrp2017/17%20Depuydt%20Presentation.pdf

[33] Baumann, K. S., Flatten, V., Weber, U., Lautenschläger, S., Eberle, F., Zink, K., & Engenhart-Cabillic, R. (2019). Effects of the Bragg peak degradation due to lung tissue in proton therapy of lung cancer patients. Radiation oncology (London, England), 14(1), 183. https://doi.org/10.1186/s13014-019-1375-0

[34] Zhang, G., Wang, J., Wang, Y., & Peng, H. (2021). Proton FLASH: passive scattering or pencil beam scanning?. Physics in medicine and biology, 66(3), 03NT01. https://doi.org/10.1088/1361-6560/abd22d

[35] Wang, P., Tang, S., Leach, K., Mangona, V., Simone, C. B., 2nd, Langen, K., & Chang, C. (2020). Proton pencil beam scanning treatment with feedback based voluntary moderate breath hold. Medical dosimetry : official journal of the American Association of Medical Dosimetrists, 45(3), e10–e15. https://doi.org/10.1016/j.meddos.2019.11.003

[36] MD Anderson. Pencil Beam Proton Therapy. 2022. Retrieved from: https://www.mdanderson.org/cancerwise/pencil-beam-proton-therapy--what-to-know.h00-159305412.html

[37] Underberg, R. W., Lagerwaard, F. J., Slotman, B. J., Cuijpers, J. P., & Senan, S. (2005). Benefit of respiration-gated stereotactic radiotherapy for stage I lung cancer: an analysis of 4DCT datasets. International journal of radiation oncology, biology, physics, 62(2), 554–560. https://doi.org/10.1016/j.ijrobp.2005.01.032

[38] Adamczyk, M., Konkol, M., Matecka-Nowak, M., & Piotrowski, T. (2020). 4DCT-based evaluation of lung tumour motion during the breathing cycle. *Neoplasma*, *67*(1), 193–202. https://doi.org/10.4149/neo_2019_190309N206

[39] Liu, J., Lin, T., Fan, J., Chen, L., Price, R., & Ma, C. C. (2018). Evaluation of the combined use of two different respiratory monitoring systems for 4D CT simulation and gated treatment. *Journal of applied clinical medical physics*, *19*(5), 666–675. https://doi.org/10.1002/acm2.12434

[40] Dietrich, L., Jetter, S., Tücking, T., Nill, S., & Oelfke, U. (2006). Linac-integrated 4D cone beam CT: first experimental results. *Physics in medicine and biology*, *51*(11), 2939–2952. https://doi.org/10.1088/0031-9155/51/11/017

[41] He, T., Xue, Z., Nitsch, P. L., Teh, B. S., & Wong, S. T. (2013). Helical mode lung 4D-CT reconstruction using Bayesian model. *Medical image computing and computer-assisted intervention : MICCAI ... International Conference on Medical Image Computing and Computer-Assisted Intervention*, *16*(Pt 3), 33–40. https://doi.org/10.1007/978-3-642-40760-4_5

[42] Valenti, M., Campanelli, A., Parisotto, M., & Maggi, S. (2018). Cine 4DCT imaging artifacts: Quantification and correlations with scanning parameters and target kinetics. *Physica medica : PM : an international journal devoted to the applications of physics to medicine and biology : official journal of the Italian Association of Biomedical Physics (AIFB)*, *52*, 133–142. https://doi.org/10.1016/j.ejmp.2018.07.006

[43] 4D CT cookbook 2.1 A guide to 4D CT imaging in RT. Published by Siemens Healthcare GmbH ©Siemens Healthcare GmbH, 2020. Retrieved from: https://cdn0.scrvt.com/7b8dc61d55f0deedb776692474194f7c/6f12b0f4879fe7c0/d11ea7897f8e/siemens-healthineers_SOMATOM-Go_4DCT_Cookbook.pdf

[44] Li, X., Chen, E., Guo, B., Yang, W., Han, R., Hu, C., Zhang, L., Pan, C., Ma, S., & Kuang, Y. (2020). The impact of respiratory motion and CT pitch on the robustness of radiomics feature extraction in 4DCT lung imaging. *Computer methods and programs in biomedicine*, *197*, 105719. https://doi.org/10.1016/j.cmpb.2020.105719

[45] Thoracic Key. Helical 4D CT and Comparison with Cine 4D CT. 2016. Retrieved from: https://thoracickey.com/helical-4d-ct-and-comparison-with-cine-4d-ct/

[46] Pan T. (2005). Comparison of helical and cine acquisitions for 4D-CT imaging with multislice CT. *Medical physics*, *32*(2), 627–634. https://doi.org/10.1118/1.1855013

[47] Chi, Y., Liang, J., Qin, X., & Yan, D. (2012). Respiratory motion sampling in 4DCT reconstruction for radiotherapy. *Medical physics*, *39*(4), 1696–1703. https://doi.org/10.1118/1.3691174.

[48] Aznar, M. C., Persson, G. F., Kofoed, I. M., Nygaard, D. E., & Korreman, S. S. (2014). Irregular breathing during 4DCT scanning of lung cancer patients: is the midventilation approach robust?. *Physica medica : PM : an international journal devoted to the applications of physics to medicine and biology : official journal of the Italian Association of Biomedical Physics (AIFB)*, *30*(1), 69–75. https://doi.org/10.1016/j.ejmp.2013.03.003

[49] Thieke C. (2018). „Gross tumour volume" (GTV) : Grundsätze, Methoden, Registrierung, Grenzen [Gross tumour volume (GTV) : Basics, methods, registration, limitations]. *Der Radiologe*, *58*(8), 722–729. https://doi.org/10.1007/s00117-018-0416-2

[50] Le Pechoux, C., Faivre-Finn, C., Ramella, S., McDonald, F., Manapov, F., Putora, P. M., Slotman, B., De Ruysscher, D., Ricardi, U., Geets, X., Belderbos, J., Pöttgen, C., Dziadiuszko, R., Peeters, S., Lievens, Y., Hurkmans, C., Van Houtte, P., & Nestle, U. (2020). ESTRO ACROP guidelines for target volume definition in the thoracic radiation treatment of small cell lung cancer. *Radiotherapy and oncology : journal of the European Society for Therapeutic Radiology and Oncology*, *152*, 89–95. https://doi.org/10.1016/j.radonc.2020.07.012

[51] Unkelbach, J., & Paganetti, H. (2018). Robust Proton Treatment Planning: Physical and Biological Optimization. *Seminars in radiation oncology*, *28*(2), 88–96. https://doi.org/10.1016/j.semradonc.2017.11.005

[52] Taasti, V. T., Hattu, D., Vaassen, F., Canters, R., Velders, M., Mannens, J., van Loon, J., Rinaldi, I., Unipan, M., & van Elmpt, W. (2021). Treatment planning and 4D robust evaluation strategy for proton therapy of lung tumours with large motion amplitude. *Medical physics*, *48*(8), 4425–4437. https://doi.org/10.1002/mp.15067

[53] Erik W. Korevaar, Steven J.M. Habraken, Daniel Scandurra, Roel G.J. Kierkels, Mirko Unipan, Martijn G.C. Eenink, Roel J.H.M. Steenbakkers, Stephanie G. Peeters, Jaap D. Zindler, Mischa Hoogeman, Johannes A. Langendijk, Practical robustness evaluation in radiotherapy – A photon and proton-proof alternative to PTV-based plan evaluation, Radiotherapy and Oncology, Volume 141, 2019, Pages 267-274, ISSN 0167-8140, https://doi.org/10.1016/j.radonc.2019.08.005.

[54] Meijers, A., Seller, O. C., Free, J., Bondesson, D., Seller Oria, C., Rabe, M., Parodi, K., Landry, G., Langendijk, J. A., Both, S., Kurz, C., & Knopf, A. C. (2020). Assessment of range uncertainty in lung-like tissue using a porcine lung phantom and proton radiography. *Physics in medicine and biology*, 65(15), 155014. https://doi.org/10.1088/1361-6560/ab91db

[55] Boria, A. J., Uh, J., Pirlepesov, F., Stuckey, J. C., Axente, M., Gargone, M. A., & Hua, C. H. (2018). Interplay Effect of Target Motion and Pencil-Beam Scanning in Proton Therapy for Pediatric Patients. International journal of particle therapy, 5(2), 1–10. https://doi.org/10.14338/IJPT-17-00030.1

[56] Kang, M., Huang, S., Solberg, T. D., Mayer, R., Thomas, A., Teo, B. K., McDonough, J. E., Simone, C. B., 2nd, & Lin, L. (2017). A study of the beam-specific interplay effect in proton pencil beam scanning delivery in lung cancer. *Acta oncologica (Stockholm, Sweden)*, 56(4), 531–540. https://doi.org/10.1080/0284186X.2017.1293287

[57] Varasteh Anvar, M., Attili, A., Ciocca, M., Donetti, M., Fanola Guarachi, L. K., Fausti, F., Giordanengo, S., Marchetto, F., Molinelli, S., Monaco, V., Sacchi, R., Vignati, A., & Cirio, R. (2016). Quality assurance of carbon ion and proton beams: A feasibility study for using the 2D MatriXX detector. *Physica medica : PM : an international journal devoted to the applications of physics to medicine and biology : official journal of the Italian Association of Biomedical Physics (AIFB)*, 32(6), 831–837. https://doi.org/10.1016/j.ejmp.2016.05.058

[58] Lin, L., Kang, M., Solberg, T. D., Mertens, T., Baeumer, C., Ainsley, C. G., & McDonough, J. E. (2015). Use of a novel two-dimensional ionization chamber array for pencil beam scanning proton therapy beam quality assurance. *Journal of applied clinical medical physics*, 16(3), 5323. https://doi.org/10.1120/jacmp.v16i3.5323

[59] Shi, C., Chen, Q., Yu, F., Zhang, J., Kang, M., Tang, S., Chang, C., & Lin, H. (2021). Auto-Trending daily quality assurance program for a pencil beam scanning proton system aligned with TG 224. *Journal of applied clinical medical physics*, 22(1), 117–127. https://doi.org/10.1002/acm2.13117

[60] MyQA machines. MACHINE QA INDEPENDENT & INTEGRATED. 2019. Retrieved from: https://www.iba-dosimetry.com/fileadmin/user_upload/products/02_radiation_therapy/Machine-QA_Brochure_Rev.2_1219.pdf

[61] IBA Dosimetry. MatriXX Universal Detector Array. 2022. Retrieved from: https://www.iba-dosimetry.com/product/matrixx-universal-detector-array

[62] Padilla-Cabal, F., Georg, D., & Fuchs, H. (2018). A pencil beam algorithm for magnetic resonance image-guided proton therapy. *Medical physics*, 45(5), 2195–2204. https://doi.org/10.1002/mp.12854

[63] Smith, B. R., Pankuch, M., Hyer, D. E., & Culberson, W. S. (2020). Experimental and Monte Carlo characterization of a dynamic collimation system prototype for pencil beam scanning proton therapy. *Medical physics*, 47(10), 5343–5356. https://doi.org/10.1002/mp.14453

[64] Shen, J., Tryggestad, E., Younkin, J. E., Keole, S. R., Furutani, K. M., Kang, Y., Herman, M. G., & Bues, M. (2017). Technical Note: Using experimentally determined proton spot scanning timing parameters to accurately model beam delivery time. *Medical physics*, 44(10), 5081–5088. https://doi.org/10.1002/mp.12504

[65] Pfeiler, T., Bäumer, C., Engwall, E., Geismar, D., Spaan, B., & Timmermann, B. (2018). Experimental validation of a 4D dose calculation routine for pencil beam scanning proton therapy. *Zeitschrift fur medizinische Physik*, 28(2), 121–133. https://doi.org/10.1016/j.zemedi.2017.07.005

[66] L. Zhao , G. Liu, X. Li, W. Zhen, A. Qin, D. Yan, A. Lee, C. Stevens, R. Deraniyagala, J. Shen, G. Janssens, S. Tang and X. Ding. (2021). Introduce An Experimental Approach to Accurately Model Delivery Sequence and Beam Delivery Time Based On a Cyclotron Accelerator Proton Therapy System. 2021 AAPM Spring Clinical Meeting. Retrieved from: http://amos3.aapm.org/abstracts/pdf/165-55292-15591641-170491-770954124.pdf

[67] Zhikai Liang , Wei Chen, Bin Qin, Xu Liu, Kaifeng Liu, Jian Zha. DESIGN OF THE ENERGY SELECTION SYSTEM FOR PROTON THERAPY BASED ON GEANT. Proceedings of Cyclotrons2016, Zurich, Switzerland. ISBN 978-3-95450-167-030

[68] Lujan, A. E., Larsen, E. W., Balter, J. M., & Ten Haken, R. K. (1999). A method for incorporating organ motion due to breathing into 3D dose calculations. *Medical physics*, 26(5), 715–720. https://doi.org/10.1118/1.598577

[69] Kamoshida, S., Okauchi, S., Osawa, H., Ohara, G., Kagohashi, K., & Satoh, H. (2021). Effect of Shakuyakukanzoto on Chemotherapy-Induced Hiccups in Patients with Lung Cancer. *The Eurasian journal of medicine*, 53(1), 2–4. https://doi.org/10.5152/eurasianjmed.2020.18184

[70] Arishima, H., & Kikuta, K. (2011). *Rinsho shinkeigaku = Clinical neurology*, 51(4), 279–281. https://doi.org/10.5692/clinicalneurol.51.279

[71] Sarudis, S., Karlsson Hauer, A., Nyman, J., & Bäck, A. (2017). Systematic evaluation of lung tumor motion using four-dimensional computed tomography. *Acta oncologica (Stockholm, Sweden)*, 56(4), 525–530. https://doi.org/10.1080/0284186X.2016.1274049

[72] Ezhil, M., Vedam, S., Balter, P., Choi, B., Mirkovic, D., Starkschall, G., & Chang, J. Y. (2009). Determination of patient-specific internal gross tumor volumes for lung cancer using four-dimensional computed tomography. *Radiation oncology (London, England)*, 4, 4. https://doi.org/10.1186/1748-717X-4-4

[73] Pepin, E. W., Wu, H., Sandison, G. A., Langer, M., & Shirato, H. (2010). Site-specific volumetric analysis of lung tumour motion. *Physics in medicine and biology*, 55(12), 3325–3337. https://doi.org/10.1088/0031-9155/55/12/005

[74] Pastor-Serrano, O., Habraken, S., Lathouwers, D., Hoogeman, M., Schaart, D., & Perkó, Z. (2021). How should we model and evaluate breathing interplay effects in IMPT?. *Physics in medicine and biology*, 66(23), 10.1088/1361-6560/ac383f. https://doi.org/10.1088/1361-6560/ac383f

[75] Coolens, C., Webb, S., Shirato, H., Nishioka, K., & Evans, P. M. (2008). A margin model to account for respiration-induced tumor motion and its variability. *Physics in medicine and biology*, 53(16), 4317–4330. https://doi.org/10.1088/0031-9155/53/16/007
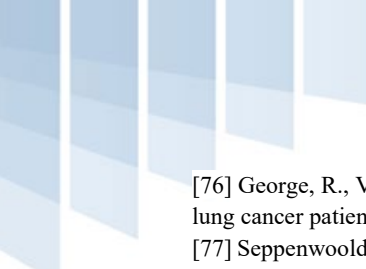
[76] George, R., Vedam, S. S., Chung, T. D., Ramakrishnan, V., & Keall, P. J. (2005). The application of the sinusoidal model to lung cancer patient respiratory motion. *Medical physics*, *32*(9), 2850–2861. https://doi.org/10.1118/1.2001220

[77] Seppenwoolde, Y., Shirato, H., Kitamura, K., Shimizu, S., van Herk, M., Lebesque, J. V., & Miyasaka, K. (2002). Precise and real-time measurement of 3D tumor motion in lung due to breathing and heartbeat, measured during radiotherapy. *International journal of radiation oncology, biology, physics*, *53*(4), 822–834. https://doi.org/10.1016/s0360-3016(02)02803-1

[77] Rana, S., & Rosenfeld, A. B. (2022). Small spot size versus large spot size: Effect on plan quality for lung cancer in pencil beam scanning proton therapy. *Journal of applied clinical medical physics*, *23*(2), e13512. https://doi.org/10.1002/acm2.13512